Utilizing airborne lidar observations for the exploration of gravity waves in the middle atmosphere

Stefanie Knobloch

München 2024

Utilizing airborne lidar observations for the exploration of gravity waves in the middle atmosphere

Stefanie Knobloch

Dissertation
an der Fakultät der Physik
der Ludwig–Maximilians–Universität
München

vorgelegt von
Stefanie Knobloch
aus Gronau

München, den 29.04.2024

Erstgutachter: Prof. Dr. Markus Rapp
Zweitgutachter: Prof. Dr. Martin Riese
Tag der mündlichen Prüfung: 28.06.2024

I wish I was Admiral FitzRoy,
Who up in the clouds calmly sits – high
Ordering here, and ordering there
The wind and the weather – foul and fair.

— W. G. Herdman, *Aeolus Redivivus* (1863)

Zusammenfassung

Das flugzeuggetragene Lidar ALIMA „Airborne Lidar for Middle Atmosphere research“ wurde erstmals während der Kampagne „Southern Hemisphere Transport, Dynamics, and Chemistry – Gravity Waves“ im September 2019 eingesetzt zur Untersuchung von Schwerewellen in der mittleren Atmosphäre. Die Dissertation prüft die Hypothese, dass flugzeuggetragene Lidar-Beobachtungen gut geeignet sind, um Schwerewellen in der mittleren Atmosphäre zu erforschen und analysiert die flugzeuggetragene Beobachtungen von ALIMA. Beobachtungen von sechs nächtlichen Forschungsflügen in der Nähe der Südanden, der Drake-Passage und der Antarktischen Halbinsel werden ausgewertet, ebenso wie Daten von der ECMWF Reanalyse v5 und idealisierte Simulationen.

Die flugzeuggetragene Operation von ALIMA ermöglicht die Untersuchung von horizontalen Skalen von Schwerewellen. Um die Beobachtungen von ALIMA spektral auswerten zu können, ist es zunächst notwendig, Fehler und Unsicherheiten in den Beobachtungen und der Datenverarbeitung zu bestimmen, sowie die dynamische Situation während den Beobachtungen zu charakterisieren.

Die Dissertation zeigt, dass ALIMA eine Genauigkeit von ± 1 K und eine Präzision von 1 K bis 6 K bei der Temperaturmessungen erreicht, die hauptsächlich von der Höhe abhängen. Beiträge durch Photonenrauschen, Hintergrundphotonen, atmosphärischer Transmission und die Temperaturbestimmung aus Photonendaten werden mithilfe zusätzlicher Lidar-Simulationen getestet. Der Vergleich von hochaufgelösten idealisierten Simualtionen mit den Ergebnissen des Temperatur Retrievals zeigt, das die grundlegende Annahme eines hydrostatischen Gleichgewichts in Präzens von nicht hydrostatischen Schwerewellen nicht erfüllt ist und zu einer Unterschätzung der Temperaturstörungen von 5 % bis 20 % führt.

Tierra del Fuego wird als Hauptanregungsregion von orographischen Schwerewellen im September 2019 identifiziert, aufgrund der Verschiebung des Polarfrontjets weiter Richtung Südpol als üblich. Die Schwerewellenaktivität wird um den stratosphärischen Polarwirbel herum charakterisiert, der stark von der Stratosphärenerwärmung in südlichen Hemisphäre im Jahr 2019 beeinflusst wird. Somit ist keine deutliche Beziehung zwischen der Schwerewellenaktivität und den starken Winden am Rand des stratosphärischen Polarwirbels erkennbar.

Erstmalig werden horizontale Wellenzahlspektren aus dem gesamten Höhenbereich der Stratosphäre und Mesosphäre präsentiert, abgeleitet aus den flugzeuggetragenen Lidar-Beobachtungen. Die horizontalen Wellenzahlspektren deuten auf eine Abhängigkeit der horizontalen Skalen hin, die in der mittleren Atmosphäre einer Potenzgesetzfunktion mit Exponent $-5/3$ folgt und die teilweise von der Stratosphärenerwärmung in 2019 beeinflusst wird. Die spektrale Energie reduzierte sich um 25 % in der Mesosphäre aufgrund von reduzierter Schwerewellenaktivität.

Abstract

The Airborne Lidar for Middle Atmosphere research (ALIMA) was first deployed for the exploration of gravity waves during the Southern Hemisphere Transport, Dynamics, and Chemistry – Gravity Waves campaign in September 2019. The thesis assesses the hypothesis that airborne lidar observations are well-suited for the explorations of gravity waves in the middle atmosphere and analyzes ALIMA observations. Observations from six nighttime research flights in the vicinity of the Southern Andes, the Drake's passage and the Antarctic Peninsula are evaluated, as well as, data from the ECMWF Reanalysis v5 and idealized simulations are used.

The airborne operation of ALIMA enables the investigation of horizontal scales of gravity waves. In order to perform a spectral analysis of the observations from ALIMA, it is first necessary to determine errors and uncertainties in the observations and data processing, as well as to characterize the dynamic situation during the observations.

The theis demonstrates that ALIMA achieves an accuracy of ± 1 K and a precision of 1 K to 6 K in temperature measurements, primarily depending on the altitude. Contributions from photon noise, background photons, atmospheric transmission, and temperature retrieval from photon data are tested using additional lidar simulations. The comparison of high-resolution idealized simulations with the results of the temperature retrieval shows that the fundamental assumption of a hydrostatic equilibrium of the retrieval in the presence of non-hydrostatic gravity waves is not met, leading to an underestimation of temperature perturbations of 5 % to 20 %.

Tierra del Fuego is identified as main excitation region of orographic gravity waves during September 2019 due to the shift of the polar front jet further polewards as usual. The gravity wave activity is characterized around the stratospheric polar vortex which is strongly influenced by the 2019 Southern Hemisphere sudden stratospheric warming. Thus, no distinct relationship between gravity wave activity and the strong winds at the edge of the stratospheric polar vortex is apparent.

Novel horizontal wavenumber spectra derived from the airborne lidar observations are presented. The horizontal wavenumber spectra indicate a dependence of the horizontal scales which follows a $-5/3$ power law in the middle atmosphere and which is partly influenced by the 2019 sudden stratospheric warming. The spectral energy decreased by 25 % in the mesosphere due to reduced gravity wave activity.

Publications

Parts of this thesis have been published in the following article:

S. Knobloch, B. Kaifler, A. Dörnbrack, and M. Rapp (2023). "Horizontal Wavenumber Spectra Across the Middle Atmosphere From Airborne Lidar Observations During the 2019 Southern Hemispheric SSW". in: *Geophysical Research Letters* 50.14. e2023GL104357 2023GL104357, e2023GL104357. DOI: https://doi.org/10.1029/2023GL104357

Sections 5.1, 5.2, 5.3, 5.4 and 5.5 of this thesis are literal excerpts of the publication, while Section 4.2 partly includes literal excerpts of the publication.

Contents

1. Introduction

With every breath we Humans take into our body, we interact with Earth's atmosphere. The atmosphere enables our life. It protects and sustains life by shielding lethal cosmic radiation, adjusting incoming and outgoing radiation, and keeping the air temperature near the surface habitable and comfortable. The atmosphere and its weather are ubiquitous for the modern society: Weather forecasts communicated by neat meteorologists in the TV or by an app on the smartphones, documentaries on the anthropogenic climate change on YouTube or strikes for climate in the cities. Stunningly, the modern science of the atmosphere is however barely 200 years old.[1]

In the 19th century, advances in scientific understanding and technology revolutionized the handling of the weather. The invention of the telegraph facilitated the rapid transmission of weather observations across long distances. This enabled the establishment of weather networks, where meteorological observations from multiple locations were collected and analyzed to discern patterns.

Finally, the first storm warning was published by Admiral FitzRoy in 1860. The „Deutsche Seewarte" in Germany released weather forecasts first from 1876.

The birth of modern weather forecasting can be attributed to the pioneering work of scientists such as Lewis Fry Richardson and Vilhelm Bjerknes. Richardson developed the concept of Numerical Weather Prediction (NWP), envisioning the use of mathematical equations to simulate atmospheric behavior (Richardson, 1922). Bjerknes, along with his colleagues, established the Bergen School of Meteorology in Norway, where they integrated observations and physics-based equations to create the first operational weather forecast models.

However, for a long time the weather forecasts were barely short-time forecasts or nowcasts. Meteorologists sketched surface weather maps based on telegraphed observations and drew conclusions about the advection of weather phenomena. Yet, no profound knowledge about atmospheric dynamics was available nor were the temporal integrations very fruitful. Simply out of one reason – *the lack of sufficient observations*, whether in sampling frequency or coverage.

Observations provide essential information about the current state of the atmosphere. These measurements serve as the foundation for weather models, allowing them to simulate and project the future state of the atmosphere. The invention of weather radars, radiosondes (weather balloons equipped with instruments), remote-sensing techniques and weather satellites revolutionized the collection of atmospheric data. These technologies

[1] Find out more about the history of atmospheric sciences with this selection of popular scientific books: The Weather Experiment: The Pioneers Who Sought to See the Future by Peter Moore; Fixing the Sky: The Checkered History of Weather and Climate Control by James Rodger Fleming; or The Weather Machine by Andrew Blum.

provided crucial observations of atmospheric parameters, including temperature, humidity, wind, and cloud cover, enhancing the abilities of weather forecasts.

Nevertheless, todays atmospheric observations are still patchy, often not continuous and come with limitations. The modern atmospheric science still has the *need for more observations* in order to generate an extensive image of the current state of the atmosphere for the initialization of NWP, to improve the weather forecasting systems and to develop a deeper knowledge about atmospheric processes.

The middle atmosphere poses significant challenges when it comes to observations (e.g. Brasseur and Solomon, 2005). The term *middle atmosphere* comprises the atmospheric layers stratosphere (10–50 km) and mesosphere (50–90 km) (e.g. Randel, 2003). The remoteness and low atmospheric density at the altitudes of the middle atmosphere limit the availability and application of measurement techniques. Consequently, obtaining comprehensive and precise data about the middle atmosphere has been a complex task for scientists.

The zonal mean zonal wind velocity can reach remarkable magnitudes as high as 100 ms^{-1} at an altitude of approximately 50 km and 60-80 ms^{-1} at an altitude of approximately 70 km at the midlatitudes in the winter (e.g. Brasseur and Solomon, 2005). It was originally anticipated that these strong zonal winds would persist up to an altitude of 100 km, based on considerations of a radiative equilibrium (Fig. 2.1a, b). However, observations made during the 1960s using rocketsondes revealed a significant inconsistency beyond certain altitudes. Instead of maintaining their strength, the zonal mean zonal winds weakened or even changed direction above approximately 70 km altitude causing a meridional flow from the summer to the winter hemisphere in the mesosphere (Murgatroyd and Singleton, 1961; Leovy, 1964).

To explain this unexpected weakening of the zonal winds, a theory emerged, focusing on the influence of mechanical friction caused by the breaking of atmospheric internal waves (Houghton, 1978; Lindzen, 1981; Matsuno, 1982; Holton, 1983). Atmospheric internal waves range from Rossby waves at the planetary scales to Gravity Waves (GW) at the mesoscales from about 1000 km to 1 km. The theory aimed to understand the impact of GW breaking processes on the dynamics of the middle atmosphere. Selective filtering of GW phase speeds equal to the background flow speed of a broad spectrum of GWs excited in the troposphere drives the residual circulation in the mesosphere. Sources of GWs are flow over orography (orographic waves or Mountain Waves (MW)) or nonorographic generation, e.g. convection, frontal systems, and spontaneous imbalance (e.g. Fritts and Alexander, 2003; Nappo, 2012). Furthermore, GWs and Rossby waves contribute significantly to the Quasi-Biennial Oscillation (QBO) and the Brewer-Dobson-Circulation (BDC) (Baldwin et al., 2019). Thus, atmospheric waves have a significant influence on the dynamics of the middle atmosphere (e.g. Becker, 2012).

The progress in understanding the middle atmospheric circulation was facilitated by the development of large atmospheric radars, e.g. Mesospheric Stratospheric and Tropospheric (MST) radars (Gage and Balsley, 1984; Tsuda, 2014). MST radars are capable of detecting atmospheric winds through the returned radar signal from refractive index fluctuations due to the varying atmospheric density or gradients in the electron density. These radars provided valuable insights into the behavior and effects of GWs

in the middle atmosphere, shedding light on the deviation of observations from the expectations based on an atmosphere in radiative balance.

Other common methods for observing GWs in the middle atmosphere are radiosondes (e.g. Lane et al., 2003; Geller and Gong, 2010), rocket soundings (e.g. Eckermann et al., 1995; Rapp et al., 2004) or ground-based lidars (e.g. von Zahn et al., 2000; Sica and Haefele, 2015; Kaifler and Kaifler, 2021). These are capable of providing high-resolution observations resolved in time, however, they are limited to vertical sampling at a single geographic location. Lidars provide atmopsheric backscatter profiles from which the density, temperature and depending on the used detection method wind can be determined. Ground-based lidars and rocket soundings provided the first temperature profiles in the Mesosphere Lower Thermosphere (MLT) region (Fricke and von Zahn, 1985). Satellite measurements facilitate a (near-) global coverage but are limited in spatial and temporal resolution and cover only a fraction of the GW spectrum (Alexander, 1998). Therefore, satellite observations were mainly investigated for the global distribution and seasonal variation of GW characteristics, e.g. energy and momentum fluxes (e.g. Wu and Waters, 1996; McLandress et al., 2000; Preusse et al., 2000; Ern et al., 2018; Hindley et al., 2020).

Lidars have also been employed on a ship (von Zahn et al., 1996; Wing et al., 2021) and a stratospheric balloon (Kaifler et al., 2020a; Kaifler et al., 2022).

Another approach for the exploration of GWs in the middle atmosphere is the usage of an airborne lidar with an aircraft as platform. The technique was applied only in a few campaigns during th last 40 years (Kwon et al., 1990; Gardner, 1991; Godin et al., 1994; Gardner, 1995; Burris et al., 2002; Fritts et al., 2016; Rapp et al., 2021).

Recent technological advances since the last applications of airborne lidar have improved the data quality, resolution and altitude range of airborne lidar measurements (Kaifler and Kaifler, 2021; Knobloch et al., 2023). Therefore, this thesis evaluates the hypothesis:

Airborne lidar observations are well-suited for the exploration of GWs in the middle atmosphere.

The thesis examines the Airborne Lidar for Middle Atmosphere research (ALIMA). ALIMA was operated for the first time during the Southern Hemisphere Transport, Dynamics, and Chemistry – Gravity Waves (SouthTRAC-GW) campaign. SouthTRAC-GW was conducted in the vicinity of Southern Andes and above the Antarctic peninsula during September 2019 (Rapp et al., 2021). A unique set of GW observations from the troposphere up to the mesosphere was obtained for the study of MWs near their orographic sources, their vertical and horizontal propagation, and their breaking and dissipation. Prior to analyzing the GW signatures in the measured density and temperature profiles obtained by ALIMA, in a first step in this thesis it is investigated

(1) How accurate and precise are the densities and temperatures derived from ALIMA observations?

The causes for potential uncertainties and biases in retrieved densities and temperatues are characterized by evaluating applied corrections and the temperature retrieval with the aid of lidar simulations. Error estimates have been performed for ground-based lidar instruments (Leblanc et al., 1998; Leblanc et al., 2016). The impact of the airborne operation on the error estimates is refined in this thesis.

The SouthTRAC-GW campaign coincided with the 2019 Southern Hemisphere (SH) Sudden Stratospheric Warming (SSW). A SSW is the phenomenon of an abrupt change in the polar winter stratosphere (e.g. Baldwin et al., 2021). The normally strong westerly Polar Night Jet (PNJ) encircling the Stratospheric Polar Vortex (SPV) (Manney et al., 2022) is decelerated to a complete reversal within days, which provokes the stratospheric temperatures to rapidly increase by up to 50°C. Like for the QBO and the BDC, the breaking of vertically propagating planetary waves in the stratosphere is responsible for the deceleration of the zonal circulation (Matsuno, 1971). The 2019 SH SSW is classified as minor event (Yamazaki et al., 2020) following the common metric by Charlton and Polvani (2007) because the zonal wind did not reverse at 10 hPa (compared to a major event) even though the zonal wind was decelerated by up to 72 ms^{-1} (Eswaraiah et al., 2020). A SSW results in a severe constraint for vertically propagating GWs due to the formation of a critical level, specifically for MWs if the zonal wind drops to 0 ms^{-1} at the altitude of reversal. In order to understand the occurrence of GWs observed with ALIMA, it is analyzed

(2) What was the dynamical condition during SouthTRAC-GW and how did it impact the observed GWs?

A fraction of the spectrum of GWs constitute a subgrid-scale process for NWP and climate models which means that horizontal scales are smaller than the horizontal resolution of the models (e.g. McLandress, 1998; Kim et al., 2003). The physical effects of the unresolved horizontal scales of GWs have to be parameterized. Otherwise, the exerted drag by GWs on the mean circulation is underestimated, resulting in a too strong PNJ in the stratosphere and the cold-pole bias (e.g. Shepherd, 2000; McLandress et al., 2012).

GW parameterizations are used to approximate GW effects on the circulation and are not explicitly expressed with a given spectral slope of the horizontal wavenumber k spectrum of GWs. The spectral slope is a statistcal feature that describes how energy is distributed and transferred across different scales. Therefore, parameterizations rely on observations to validate and calibrate that the parametizations capture the appropriate energy distribution and characteristics of GWs.

Horizontal wavenumber spectra based on observations at tropopause altitudes feature an approximate $k^{-5/3}$-dependence (Nastrom and Gage, 1983; Nastrom and Gage, 1985). Airborne in-situ and lidar observations in the lower stratosphere, at the mesopause and lower thermosphere also allowed for studying the k-dependence of the mesoscale spectrum (Kwon et al., 1990; Hostetler et al., 1991; Hostetler and Gardner, 1994; Bacmeister et al., 1996; Gao and Meriwether, 1998; Cho et al., 1999b).

Due to the lack of sufficient observations in the middle atmosphere, no information about the horizontal wavenumber spectrum of the mesoscales in the mesosphere exists so far. The technical advances of ALIMA and the resulting high-resolution horizontally resolved dataset from the SouthTRAC-GW campaign permit to evaluate

(3) What is the shape of horizontal wavenumber spectrum throughout the middle atmosphere in the vicinity of the MW hotspot above the Southern Andes?

Furthermore, SouthTRAC-GW was the first time that horizontally resolved lidar observations of GWs during a SSW were obtained. Therefore, it is examined

(4) How is the horizontal wavenumber spectrum in the middle atmosphere affected by GWs and the SSW?

The thesis is structured as follows: Chapter 2 gives a brief introduction to the theory of general atmospheric dynamics, atmospheric GWs and the airborne Rayleigh lidar technique. Chapter 3 focuses on the ALIMA instrument and evaluates question **(1)**. Question **(2)** is approached in Chapter 4. There, the large-scale dynamics, namely the tropospheric excitation conditions for MWs, are discussed, as well as, the GWs dynamics along the flight tracks of SouthTRAC-GW. In Chapter 5 horizontal wavenumber spectra based on ALIMA observations are presented and questions **(3)** and **(4)** are discussed. Finally, the findings of this thesis are summarized and the hypothesis of this thesis is reviewed in Chapter 6.

2. Theory

2.1. General dynamics

The general dynamics or motion of the atmosphere is the consequence of gradients of atmospheric properties, as temperature, pressure or moisture, in all directions and the continuous counteracting of the atmosphere to eliminate the gradients. The equations that govern the motion of a fluid parcel in the atmosphere are the momentum conservation equation, mass conservation (continuity) equation and energy conservation equation (e.g. Lin, 2007; Holton and Hakim, 2013):

$$\frac{D\vec{\boldsymbol{u}}}{Dt} = -2\vec{\boldsymbol{\Omega}} \times \vec{\boldsymbol{u}} - g - \frac{1}{\rho}\nabla p + \vec{\boldsymbol{F}}, \tag{2.1}$$

$$\frac{D\rho}{Dt} + \rho(\nabla \cdot \vec{\boldsymbol{u}}) = 0, \tag{2.2}$$

$$\frac{D\theta}{Dt} = \frac{\theta}{c_p T}\dot{Q}. \tag{2.3}$$

Here $\vec{\boldsymbol{u}}$ is the three-dimensional velocity vector, $\vec{\boldsymbol{\Omega}}$ is the Earth's rotation vector, g is the acceleration due to Earth gravity, ρ is the density, p is the pressure. The temperature T is related to the potential temperature θ through the Poisson equation:

$$\theta = T(\frac{p_0}{p})^{\kappa}, \tag{2.4}$$

where p_0 refers to pressure at a reference altitude and $\kappa = \frac{R_d}{c_p}$ is the Poisson constant with the gas constant R_d and specific heat capacity c_p for an ideal gas. $\vec{\boldsymbol{F}}$ and $\dot{Q}$ represent frictional forces and diabatic heating per unit mass. Together, the governing equations form a system of partial differential equations that describe the temporal evolution of the fluid velocity, pressure, and density in the atmosphere.

The total (material) derivative $\frac{D}{Dt} = \frac{\partial}{\partial t} + \vec{\boldsymbol{u}} \cdot \nabla = \frac{\partial}{\partial t} + u\frac{\partial}{\partial x} + v\frac{\partial}{\partial y} + w\frac{\partial}{\partial z}$ is the Lagrangian rate of change of a fluid parcel, consisting of the local Eulerian derivative and the advection.

Since the set of equation is underdetermined (more unknown variables than equations), an additional diagnostic equation, the equation of state, is needed. For an ideal gas, that is:

$$p = \rho \cdot R \cdot T. \tag{2.5}$$

2.2. Atmospheric gravity waves

Internal[2] GWs are oscillations of fluid parcels displaced vertically within a stably stratified fluid on which the buoyancy force acts as restoring force opposite to the displacement. GWs are therefore also called buoyancy waves.

Stable stratification refers to an atmospheric condition in which $\partial\theta/\partial z > 0$. A stably stratified fluid depicts a favorable environment for the generation and propagation of GWs, as it results in a strong buoyant force that tries to move the vertically displaced parcels back to their original positions. On the other hand, neutral stratification refers to a condition where $\partial\theta/\partial z = 0$. In this state, buoyancy forces are zero and air parcels displaced vertically neither experience significant restoring forces nor are they inherently stable or unstable. Unstable stratification occurs when $\partial\theta/\partial z < 0$. In this situation, air parcels that are displaced vertically continue to rise from their original positions without being significantly affected by restoring forces. Thus, neutral and unstable stratification inhibits the formation of GWs by leading to their dissipation by overturning and turbulence.

GWs are generated by a variety of sources which can be classified as orographic (MWs) and non-orographic (e.g. Fritts and Alexander, 2003; Nappo, 2012). The latter includes wave generation through convection, jet streams, frontal systems, volcanic eruptions (e.g. Wright et al., 2022; Yue et al., 2022), and secondary wave generation through the breaking of primary GWs (e.g. Vadas et al., 2003; Bossert et al., 2017; Vadas et al., 2018). The generation mechanism is important because it determines the resulting wave properties, e.g. wavelengths and amplitudes. GWs are one of the mechanisms the atmopshere uses to restore its equilibrium and eliminate gradients in atmospheric properties.

The nonlinear governing equations (2.1) - (2.5) can be linearized into a horizontally uniform and hydrostatic background $\overline{(...)}$ and first-order perturbations $(...)'$:

$$ab(x, y, z, t) = \overline{ab}(z) + ab'(x, y, z, t), \tag{2.6}$$

assuming an irrotational, inviscid, adiabatic and incompressible flow and that perturbations are small compared to the hydrostatic background. The linearized equations can be combined, assuming a wave-like solution $a' = \Re\left\{\tilde{a_k} \cdot e^{i(kx-\omega_k t)}\right\}$ for the k^{th} wave mode, and simplified to the Taylor-Goldstein equation (Taylor, 1931; Goldstein, 1931):

$$\frac{d^2\hat{w}}{dz^2} + \left(\frac{k^2 \cdot N^2}{\Omega^2} + \frac{k}{\Omega}\frac{d^2\overline{u}}{dz^2} - k^2 - \frac{k}{\Omega}\frac{1}{H}\frac{d\overline{u}}{dz} - \frac{1}{4H^2}\right)\hat{w} = 0, \tag{2.7}$$

with the vertical velocity perturbation $\hat{w}$ approximated from $\tilde{w_k}$ for one specific wave mode and the scale height H. The Taylor-Goldstein equation describes how the GW amplitude changes with altitude. Furthermore, k is the horizontal wavenumber[3] which is

[2] versus external GWs which propagate on a density discontinuity surface. Throughout this thesis, only internal gravity waves are examined and for simplicity just called GWs.

[3] In this thesis, k is not divided into the respective components (K, L) in (x, y) or zonal and meridional direction. This chapter, therefore, only includes the 2D Taylor-Goldstein equation (2.7) and 2D dispersion relation(2.10). Why k is handled in this way will be discussed in Chapter 5.

related to the horizontal wavelength λ_k by $k = 2\pi/\lambda_k$, Ω is the intrinsic frequency of a wave relative to the flow, $\overline{u}$ is the background wind, and N is the buoyancy frequency or Brunt-Vaisala frequency. N describes the oscillation of a fluid parcel about its equilibrium level in a stably stratified atmosphere and can be expressed as:

$$N^2 = \frac{g}{\overline{\theta}} \frac{d\overline{\theta}}{dz}, \tag{2.8}$$

where $\overline{\theta}$ is the background potential temperature. The Brunt-Vaisala frequency is a measure of stability and reflects the atmospheric conditions.

The terms in brackets of the Taylor-Goldstein equation (2.7) can be simplified by introducing the vertical wavenumber m, assuming that the vertical wavelength λ_m of a wave is much smaller than H:

$$m^2 = \frac{N^2}{(c_k - \overline{u})^2} + \frac{1}{c_k - \overline{u}} \frac{d^2\overline{u}}{dz^2} - k^2, \tag{2.9}$$

where c_k is the horizontal phase speed. GWs are dispersive waves which means that c_k depends on k, for example $c_k = \omega/k$ with the apparent frequency $\omega = \Omega + \overline{u} \cdot k$.

Furthermore, m can be related to ω, which is called the GW dispersion relation:

$$m^2 = \frac{k^2(N^2 - \omega^2)}{\omega^2 - f^2} - \frac{1}{4 \cdot H^2}. \tag{2.10}$$

If $m^2 > 0$, waves are able to propagate vertically. If $m^2 < 0$, waves are unable to propagate vertically and any vertical displacement will be evanescent with altitude. Furthermore, the atmosphere can only carry oscillations which satisfy $N \geq \Omega \geq f$, where f is the Coriolis parameter. Otherwise, oscillations become unstable if $\Omega > N$ or are absorbed by the background if $\Omega < f$.

Within the framework of the linear theory wave quantities are related to each other, which is known as the polarization equations (e.g. Markowski and Richardson, 2010; Nappo, 2012):

$$\hat{u} = -\frac{m}{k}\hat{w}, \tag{2.11}$$

$$\hat{p} = -\frac{\overline{\rho} m(\omega - \overline{u}k)}{k^2}\hat{w} = \frac{\overline{\rho} m \Omega}{k^2}\hat{w}, \tag{2.12}$$

$$\hat{\theta} = -\frac{i}{(\omega - \overline{u}k)} \frac{d\overline{\theta}}{dz}\hat{w} = -\frac{i}{\Omega} \frac{d\overline{\theta}}{dz}\hat{w}. \tag{2.13}$$

GWs are classified as high-, mid- and low-frequency GWs (Fritts and Alexander, 2003). High-frequency GWs feature $\Omega >> f$ and small λ_k. GWs which obey $N \gg \Omega \gg f$ are mid-frequency GWs. Low-frequency GWs are characterized by $\Omega \approx f$ and are called inertia-GWs. f is relevant for these large λ_k. Inertia-GWs are excited by large-scale orography and weather systems.

GWs propagate horizontally and vertically and carry energy and momentum over large distances. GWs can get partially reflected or refracted, generated by wave-wave

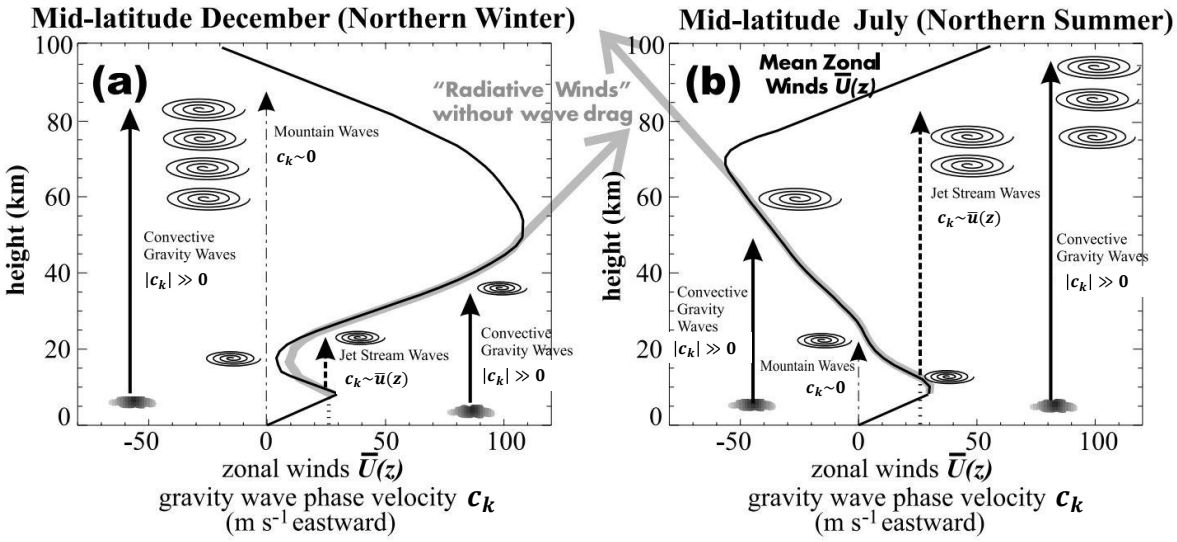

Figure 2.1.: Mid-latitude zonal wind profiles of observed winds (black curve) and radiatively balanced winds (grey curve) of December (a) and July (b). Adapted from Kim et al. (2003) after Lindzen (1981).

interactions or secondary sources (e.g. Hines, 1974). As a GW propagates vertically from the troposphere[4] to the middle atmosphere, the amplitude grows with altitude due to the decreasing atmospheric density. The amplitude growth is not unlimited, as various factors can dampen GWs, e.g. wave saturation or wave breaking.

GW saturation occurs when the energy lost through dissipation, breaking, or nonlinear interactions becomes balanced with the energy gained from the mean flow. At this point, the GW amplitude reaches a maximum, stabilizes and remains convectively stable. The GW is said to be saturated.

Selective filtering of GW modes by critical levels causes wave breaking. A critical level describes the altitude where $\overline{u}(z_c) = c_k$. This causes a singularity of equation (2.9) as $m^2 \to \infty$ and $\lambda_m \to 0$. In a (x, z) cross section of GW signatures, the phase lines tilt into the horizontal at a critical level and amplitudes tend theoretically to infinity. In reality, wavebreaking and overturning occurs and a wave only approaches a critical level. Figure 2.1 illustrates the selective filtering of a spectrum of GWs composed of various c_k by typical mid-latitude zonal wind profiles during Northern Hemisphere (NH) winter and summer.

MWs are stationary and do not experience dispersion since $c_k = 0$ for all k excited by a mountain. However, the intrinsic phase speed of MWs is $c_I = -\overline{u}$, as a wave must be travelling upwind relative to the background flow in order to be stationary.

MWs experience a critical level where $\overline{u}(z_c) = 0$. Typically, the zonal winds are strong

[4]Obviously, MWs are always excited within the troposphere. Non-orographic GWs due to shear instabilities of jet streams or secondary wave generation can also be excited within the middle atmosphere.

and stay eastward throughout the troposphere and middle atmosphere in winter (Fig. 2.1a). MWs and non-orographic GWs which are travelling westward ($c_k < 0$) are able to propagate vertically throughout the middle atmosphere while non-orographic GWs which are travelling eastward ($c_k > 0$) are filtered by the zonal winds within the troposphere and stratosphere. During summer, the zonal winds reverse and become westward within the middle atmosphere (Fig. 2.1b). Thus, only non-orographic GWs which are travelling eastward ($c_k \gg 0$) are able to propagate vertically throughout the middle atmosphere. MWs and non-orographic GWs with ($c_k \approx \overline{u}$) expericence critical level filtering in the troposphere and stratosphere.

The breaking and dissipation of GWs in the mesosphere are a result of the amplitude growth with altitude and cause a westward force in the winter mesosphere and an eastward force in the summer mesosphere. Thus, the GW breaking decelerates the radiatively-driven westerlies in the winter mesosphere and the radiatively-driven easterlies in the summer mesosphere (Fig. 2.1a, b).

For stationary MWs, equation (2.9) can be further reduced to:

$$m^2 = \frac{N^2}{\overline{u}^2} - \frac{1}{\overline{u}}\frac{d^2\overline{u}}{dz^2} - k^2 = l^2 - k^2, \tag{2.14}$$

with the Scorer parameter (Scorer, 1949):

$$l = \sqrt{\frac{N^2}{\overline{u}^2} - \frac{1}{\overline{u}}\frac{d^2\overline{u}}{dz^2}}. \tag{2.15}$$

The Scorer parameter summarizes the atmospheric conditions (background wind and stability) and indicates whether the Taylor-Goldstein equation (2.7) yields a solution for a vertically propagating MW ($l > k$) or an evanescent flow ($l < k$). Figure 2.2 illustrates the separation in the two different regimes for typical mid-latitude NH winter conditions.

The Scorer parameter can be further used to separate MWs into hydrostatic and non-hydrostatic MWs. The classical theory of separating the wave responses goes back to Queney (1948). The theory is derived for $\overline{u}$ and N being constant with altitude.

MW perturbations in the atmosphere that exhibit the characteristic of remaining in hydrostatic balance indicate that their vertical accelerations are negligible. This behavior is observed when the dominant wave mode is the hydrostatic mode, which occurs when the time it takes for a fluid parcel to cross a mountain ridge is significantly longer than the period of a buoyancy oscillation. Several factors contribute to the dominance of the hydrostatic wave mode, including the presence of a broad mountain with a half-width $a > 10$ km, a slow mean flow speed and high static stability, summarized as:

$$l^2 >> k^2, al >> 1, Na >> \overline{u}. \tag{2.16}$$

The wave structure of hydrostatic MWs remains confined over the mountain in the horizontal direction and repeats itself vertically with a vertical wavelength:

$$\lambda_z = \frac{2\pi}{l} = \frac{2\pi\overline{u}}{N}. \tag{2.17}$$

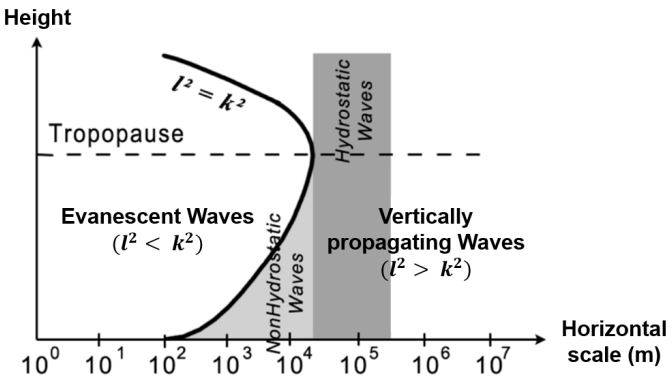

Figure 2.2.: Vertical propagation of MWs as function of horizontal scale and height and associated seperation of hydrostatic and non-hydrostatic responses under typical mid-latitude NH winter conditions. Adapted from Kim et al. (2003).

MW perturbations can exhibit significant vertical accelerations, indicating the presence of non-hydrostatic modes. This occurs when the time it takes for a fluid parcel to cross a mountain ridge is approximately equal to the period of a buoyancy oscillation. In such cases, the Ω of the non-hydrostatic MW becomes comparable to N. Thus, the MWs are no longer governed by the hydrostatic approximation. The characteristics can be summarized as:

$$l^2 \approx k^2, al \approx 1, Na \approx \overline{u}. \tag{2.18}$$

Non-hydrostatic MWs display a dispersive nature as they propagate downstream, resulting in periodic solutions in the vertical and horizontal direction. Moreover, above the mountain, the phase line tilt of the waves is inclined upstream, while the tilt decreases in the downstream direction. As the non-hydrostatic MW travels downstream, its horizontal wavelength λ_k shortens with k approaching l.

Non-hydrostatic MWs have higher ω, smaller λ_k, and exhibit faster vertical motions compared to hydrostatic MWs. Based on the theory from Queney (1948), the separation between hydrostatic and non-hydrostatic MWs occurs at $a \approx 10$ km or $\lambda_k \approx 20$ km (Fig. 2.2).

In the real atmosphere $\overline{u}$ and N vary with altitude and l typically increases within the troposphere to a maximum located at the tropopause (Fig. 2.2). The MWs with λ_k of non-hydrostatic MWs ranging from $\mathcal{O}(100)$ m to $\mathcal{O}(10)$ km become evanescent or reflected with altitude compared to MWs with longer λ_k associated with hydrostatic MWs. Thus, mostly hydrostatic MWs with $\lambda_k > 10$ km are relevant in the middle atmosphere (Fritts and Alexander, 2003).

2.3. Atmospheric horizontal wavenumber spectra

2.3.1. Horizontal scales of atmospheric dynamics

The spectrum of atmospheric dynamics covers a large range of scales (i.e. 10 orders of magnitude) from the mean free path length to the circumfence of the Earth (e.g. Markowski and Richardson, 2010).

Processes at the scales larger than a few thousand kilometers are classified as *planetary* and *synoptic scales*. The horizontal scales are much larger than the vertical scales which implies that the atmospheric motions are to a good approximation two-dimensional, quasi-geostrophic, and hydrostatic. Planetary-scale processes are associated with the global circulation, e.g. planetary waves due to the Coriolis force and climate patterns as the El Nino-Southern Oscillation (ENSO), the North Atlantic Oscillation (NAO) or the BDC. The synoptic scales comprise mid-latitudinal low- and high-pressure systems and weather systems which are driven by baroclinic instability.

The *microscales* constitute the small-scale end of the spectrum of atmospheric dynamics with scales smaller than a few kilometers down to the scales of turbulent[5] dissipation (i.e. less than millimeters in the troposphere). The horizontal scales obey similar dimensions as the vertical scales, resulting in three-dimensional motions. Microscale processes are thus characterized as non-geostrophic, non-hydrostatic, and turbulent, e.g. the three-dimensional turbulent motion in the planetary boundary layer and middle atmosphere, tornados and cumulus convection in the troposphere.

The *mesoscales* range from a few kilometers to a few thousand of kilometers. The term mesoscale was initially introduced to describe dynamical phenomena that are too large to be resolved by observations at a single location and too small to be resolved by the weather observation networks[6] (Ligda, 1951). Rather than being driven by a single dominant instability, mesoscale phenomena are influenced by a diverse range of mechanisms as orography or different types of instabilities, such as thermal instability, barotropic instability or shear instability. Also, the Coriolis force is of importance for a part of the mesoscales without being dominant as for the synoptic scales. Likewise, vertical accelerations become important for various mesoscale phenomena, e.g. convective systems or non-hydrostatic MWs. Due to this complexity, the mesoscales phenomena are commonly divided into subcategories (e.g. Orlanski, 1975; Fujita, 1981). In the troposphere, the mesoscales include atmospheric processes as fronts, hurricanes, convective systems, thunderstorms, large tornados, mountain-valley wind systems, land-sea breezes and GWs (e.g. Markowski and Richardson, 2010). In contrast, the mesoscale dynamics in the middle atmosphere consists of GWs and atmospheric two-dimensional turbulence (e.g. Becker, 2012).

[5]Turbulence describes irregular or random fluctuations superposed on mean fluid motions with the characterisitics: unpredictable, eddies on many scales, diffusive, high Reynolds number, and dissipative.

[6]Based on the density of the weather observation networks during the time of the first synoptic weather maps.

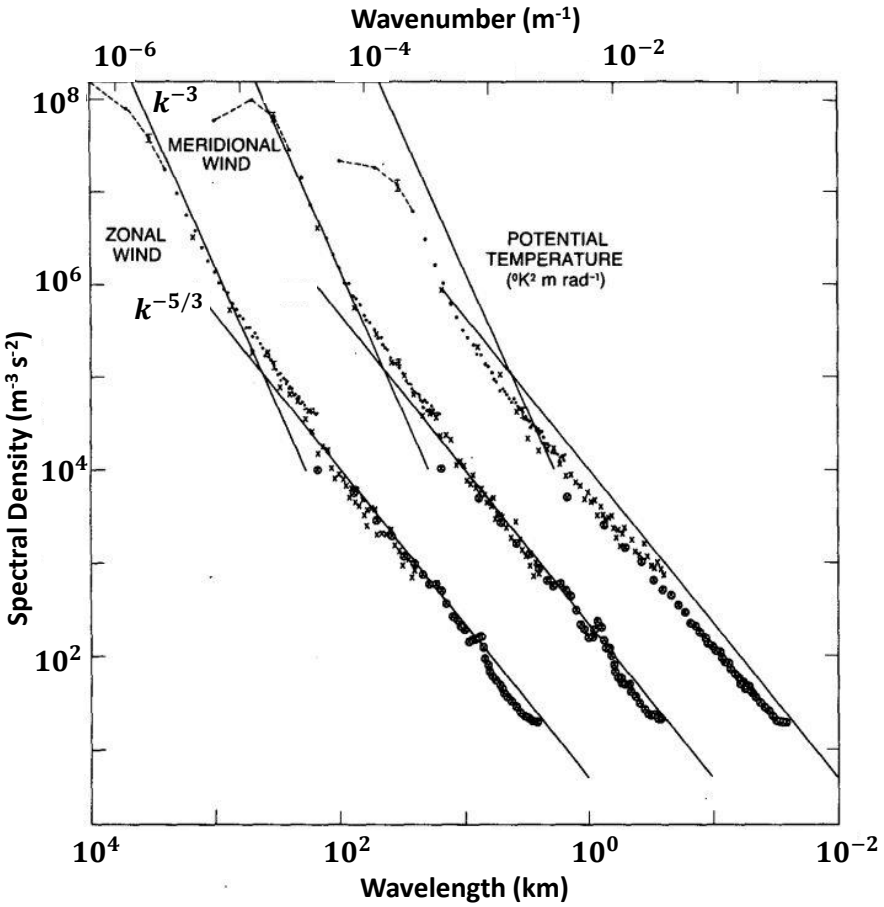

Figure 2.3.: Horizontal wavenumber spectra derived from the GASP in-situ observations of potential temperature, zonal and meridional wind velocity. Spectra of meridional wind velocity and potential temperature are shifted by one and two orders of magnitude, respectively. Figure adapted from Nastrom and Gage (1985).

2.3.2. Observations and derived horizontal wavenumber spectra

Nastrom and Gage (1983), Nastrom et al. (1984), and Nastrom and Gage (1985) conducted pioneering studies focusing on the analysis of the Global Atmospheric Sampling Program (GASP) dataset to investigate the horizontal wavenumber spectra of atmospheric kinetic energy. The GASP dataset is a comprehensive collection of in-situ atmospheric measurements obtained from about 7000 commercial flights conducted in the 1970s. The observations were collected at tropopause and cruising altitudes, different geographical locations, and season, providing a global perspective on atmospheric characteristics.

Figure 2.3 displays the horizontal wavenumber spectra of potential temperature and zonal and meridional wind velocity based on the in-situ observations from the GASP dataset (Nastrom and Gage, 1985). They found that the horizontal wavenumber spectra

exhibit a power-law behavior of approximately k^{-3} on the synoptic scales, which flattens to a power-law behavior of approximately $k^{-5/3}$ on the mesoscales (2.6km $< \lambda <$ 400km). For the planetary scales, spectral slopes are rather shallow or slightly negative.

Various observational studies support the finding of a power-law behavior of the mesoscales, even though deviations from the $k^{-5/3}$-dependence are apparent (Kwon et al., 1990; Gardner, 1991; Hostetler et al., 1991; Hostetler and Gardner, 1994; Gardner, 1995; Qian et al., 1995; Bacmeister et al., 1996; Lindborg, 1999; Schumann, 2019; Dörnbrack et al., 2022). Furthermore, observations show that the variances of atmospheric parameters are larger and a enhancement of spectral energy is evident above orography compared to smooth terrain or ocean (Lilly and Petersen, 1983; Jasperson et al., 1990; Nastrom et al., 1987; Gao and Meriwether, 1998). The spectral energy is enhanced towards higher latitudes and during winter (Nastrom and Gage, 1985; Cho et al., 1999b; Lindgren et al., 2020).

A similar power-law dependence of the mesoscales has also been found in numerical studies, including the variability due to region, altitude and season, under the consideration of model configurations and limitations (Koshyk et al., 1999; Lindborg, 2005; Waite and Snyder, 2009; Skamarock et al., 2014; Bierdel et al., 2016; Sun et al., 2017; Selz et al., 2019; Becker et al., 2022; Avsarkisov et al., 2022; Stephan et al., 2022).

2.3.3. Prevailing theory

The finding of the power-law dependence of the mesoscales instead of the initially expected mesoscale energy gap (Fiedler and Panofsky, 1970) suggests that the mesoscale dynamics are self-similar. Self-similar means that a flow exhibits a similarity across different length scales or time scales (e.g. Pope, 2000). In a self-similar flow, the statistical properties and flow patterns repeat themselves at different scales, which allows for studying the flow behavior and dynamics in a simplified manner. Instead of considering the flow at all individual scales separately, a representative scale and the use of scaling relationships are sufficient to infer the behavior at other scales.

A flow characterized by small-scale, three-dimensional, homogeneous and isotropic turbulence is self-similar, and the statistically derived horizontal wavenumber spectrum obeys (Kolmogorov, 1941; Obukhov, 1949):

$$E(k) \approx \epsilon^{2/3} \cdot k^{-5/3}, \tag{2.19}$$

where ϵ is the energy flux or rate of energy dissipation. In three-dimensional turbulence, energy tends to cascade from large scales (injection scales) to small scales (dissipation scales). In between, an intermediate range of scales exists where neither forcing nor dissipation dominate but purely inertial forces (e.g. Vallis, 2017). This range of length scales over which energy is nonlinearly transferred is called inertial range (or also inertial subrange). Kolmogorov (1941) argued that the statistics of turbulence in the inertial range is universal, meaning it depends only on the energy dissipation rate, but not on specific details of the turbulence-generating mechanism.

The relevance of three-dimensional turbulence theory is rather limited to horizontal scales of a few hundred meters or less in the lower atmosphere (Skamarock, 2004) and

to horizontal scales of a few kilometers in the upper mesosphere (Lübken, 1997). The synoptic scales and mesoscales are so different that other mechanism must be responsible for the self-similarity (universal or canonical power-law dependence). The prevalent theories are

on planetary and synoptic scales:

- *two-dimensional turbulence* or *quasi-geostrophic turbulence*

on the mesoscales:

- *stratified turbulence* or *interacting GWs*.

Two-dimensional turbulence (also called barotropic quasi-two-dimensional turbulence) reveals two inertial ranges: an upscale (inverse) energy cascade following a $k^{-5/3}$-dependence and a downscale enstrophy cascade following a k^{-3}-dependence (Kraichnan, 1967). Enstrophy is related to the vorticity of the fluid. Vorticity is defined as the curl of the velocity field (e.g. Markowski and Richardson, 2010). It quantifies the local rotation or circulation of the fluid. Enstrophy is the square of the vorticity and is a measure of the total vorticity present in a particular region of the fluid (Holton and Hakim, 2013). Two-dimensional turbulence often occurs when vertical motions are suppressed or significantly weaker compared to horizontal motions. Various factors can lead to this constraint, such as stable stratification or the presence of large-scale horizontal flows that inhibit vertical motions. Due to the conservation of enstrophy in two-dimensional flows, the enstrophy tends to accumulate at larger scales, leading to the formation of larger coherent structures (such as vortices and filaments). These structures dominate the flow and lead to the characteristic behavior of two-dimensional turbulence. Gage (1979) proposed that the $k^{-5/3}$-dependence of the mesoscales can be associated as inertial range of two-dimensional turbulence given an energy source at smaller scales, e.g. convection (Lilly, 1989). However, as rotation becomes negligible at horizontal scales of a few kilometers, strong stratification has to be dominant. Numerical studies show that strong stratification permits a downscale energy cascade rather than an upscale energy cascade (Lindborg, 2006; Brethouwer et al., 2007). Observational analysis give rise to a downscale energy cascade for horizontal scales smaller 100 km (Cho and Lindborg, 2001). Furthermore, convection is limited to the troposphere and is not a possible energy source in the middle atmosphere due to the stable stratification of the stratosphere.

Charney (1971) argued that rotation and stratification make the atmosphere quasi-two-dimensional and lead to dynamics similar to two-dimensional turbulence. His so-called geostrophic turbulence theory predicts for a three-dimensional quasi-geostrophic flow, a downscale potential enstrophy cascade following a k^{-3}-dependence for kinetic and available potential energy and an equipartition among both. Thus, the geostrophic turbulence theory only agrees with observations of large scales but deviates from observations of the mesoscales with the $k^{-5/3}$-dependence (Nastrom and Gage, 1985).

Two-dimensional turbulence and quasi-geostrophic turbulence are generally accepted theories for the synoptic scales. The predictions of the enstrophy inertial range have been supported by model studies (Koshyk and Hamilton, 2001), as well as observations

(Lindborg, 1999; Cho and Lindborg, 2001). Tung and Orlando (2003) expanded the quasi-geostrophic turbulence theory and stated that the downscale enstrophy cascade is accompanied by a downscale energy cascade following a $k^{-5/3}$-dependence which will be dominant from a certain transition scale. Furthermore, a direct downscale energy cascade in the frame of surface quasi-geostrophic dynamics has been simulated by Tulloch and Smith (2006)). Vallgren et al. (2011) showed that a direct downscale energy cascade can be generated with a flow of strong stratification and strong rotation.

Stratified turbulence refers to turbulent flows of quasi-horizontal motion with strong vertical shear that occur in a fluid with strong stratification (Lilly, 1983; Lindborg, 2006; Li and Lindborg, 2018). The stratification creates layers or interfaces of different fluid properties within the fluid. While stratification tends to inhibit vertical motions, the turbulent motions are able to cause vertical mixing. Stratified turbulence has no distinct energy source. Thus, it is often associated with breaking GWs or geostrophic turbulence interacting with the quasi-horizontal turbulent layers and sustaining the energy cascade.

Cho et al. (1999a) concluded from the spectral analysis of in-situ airborne observations within the troposphere that at horizontal scales of $1\text{km} < \lambda < 100\text{km}$ rotational modes dominate divergent modes over the Pacific Ocean except in the equatorial zone. They conclude that two-dimensional turbulence outperforms GWs as generating process of the mesoscales. The subsequent analysis by Cho and Lindborg, 2001 of globally distributed observations implies a downscale energy cascade for $1\text{km} < \lambda < 100\text{km}$.

In the lower stratosphere, divergent modes are much stronger than rotational modes (Skamarock et al., 2014; Brune and Becker, 2013), giving rise to a downscale energy cascade produced by interacting GWs (Dewan, 1979; VanZandt, 1982). Further information on the horizontal wavenumber spectrum accompanied by GWs can be found in Chapter 5.

Bacmeister et al. (1996) predicted based on a GW spectrum derived from theory that for horizontal scales larger 1000 km, the energy contribution from the GWs becomes insignificant. The transition of the spectral slope (Fig. 2.3) as shown by Nastrom and Gage (1985) could thus also be explained by a transition from GW regime to a synoptic-scale regime.

An important mechanism for the vertical transport of energy between the troposphere and the middle atmosphere is GW propagation (Gao and Meriwether, 1998; Fritts and Alexander, 2003).

2.4. The airborne Rayleigh lidar technique

2.4.1. The airborne Rayleigh lidar technique for middle atmospheric research

Light detection and ranging (lidar) is an active optical remote sensing technique based on the principles of laser ranging (e.g. Fujii, 2005; Weitkamp, 2005). Laser pulses with a wavelength λ and a duration τ_p are transmitted into the atmosphere for the primary measurement of the distance between the altitude of the transmitter z_0 and the altitude of molecules and particles z_i that backscatter the laser light (Fig. 2.4). The backscattered

radiation is then collected by a telescope, passed to a detector and converted to a electrical signal. The distance or range z results from the range equation:

$$z = \frac{1}{2} c \Delta t \tag{2.20}$$

with c being the speed of light and Δt the transit time of the light pulse. The factor $\frac{1}{2}$ in the range equation (Eq. 2.20) originates from the round-trip of the light. Due to τ_p of the laser pulse, the backscattered light is obtained from the range interval Δz:

$$\Delta z = \frac{1}{2} c \tau_p \tag{2.21}$$

When the laser light passes through the atmosphere, it encounters gas molecules such as nitrogen (N_2) and oxygen (O_2)[7], which scatter light in all directions (Fig. 2.4). This type of scattering of light that occurs when light passes through a medium that contains particles smaller than λ is called Rayleigh scattering (e.g. Wallace and Hobbs, 2006; Kenyon, 2008). It is named after Lord Rayleigh, who first described this phenomenon in the late 19th century. Rayleigh scattering depends strongly on the wavelength with the amount of scattering being proportional to λ^{-4}. This means that shorter wavelengths, such as blue and violet light, are scattered more efficiently than longer wavelengths, such as red light. Therefore, Rayleigh scattering is responsible for the blue color of the sky during daytime and the reddening of the sky during sunset and sunrise.

Another type of light scattering is Mie scattering which was first described by Gustav Mie at the beginning of the 20th century (Mie, 1908). Mie scattering is only weakly dependent of λ and can occur at any λ. According to Mie theory, when light interacts with particles, typically aerosols and cloud particles, that are comparable in size to the wavelength of the light, the scattered light is influenced not only by the size of the particles but also by their refractive index, which is different from its surrounding media. But Mie theory is not limited to a certain size of particles but provides a solution for scattering by a sphere including Rayleigh scattering. Mie scattering is responsible for the white color of clouds, as well as the iridescence of certain materials, such as butterfly wings and peacock feathers. It is also used in various applications, such as particle size analysis, aerosol research, and optical remote sensing. Lidar systems that use laser light to measure atmospheric particles rely on Mie scattering to make accurate measurements of the concentration and size distribution of particles in the atmosphere.

Rayleigh and Mie scattering are elastic scattering processes, which means that the energetic state of the particles and the wavelengths of the incident and scattered light remain unchanged if Doppler effect are neglected.

The Rayleigh lidar technique is based upon the elastic Rayleigh scattering, therefore also known as backscatter lidar or Rayleigh backscatter lidar, and is used to measure atmospheric densities and temperatures in the altitude range from 30 km to approximately

[7] Nitrogen and oxygen are the most common gases in today's atmosphere and are mainly present as dimeric molecules N_2 and O_2, respectively (Wallace and Hobbs, 2006). Atomic oxygen (O) achieves the concentration of O_2 primarily above 110 km altitude (above the turbopause) due to the seperation of atmospheric components (Kelley, 2009).

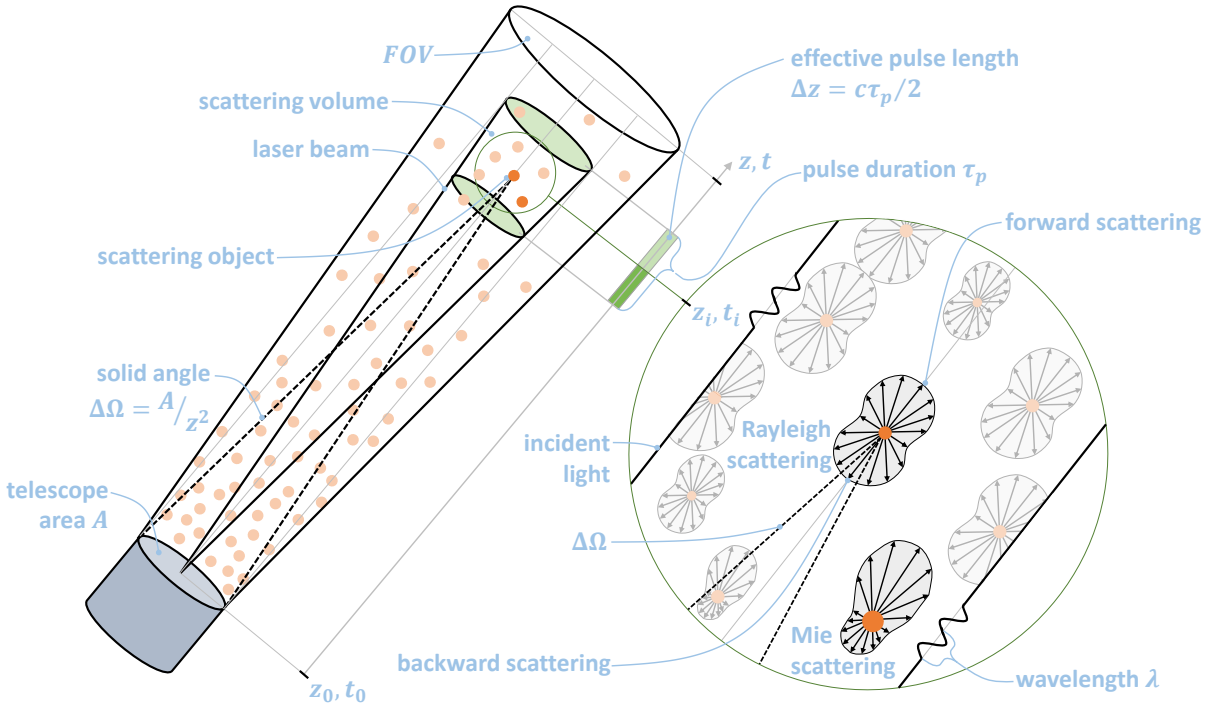

Figure 2.4.: Schematic illustration of the lidar technique and Rayleigh and Mie scattering processes.

80 km to 100 km depending on the laser power. Rayleigh lidar is together with fluorescence (or resonance scattering) lidar the most widely used lidar technique for observing and studying middle atmospheric temperatures (e.g. Gardner, 2004; Alpers et al., 2004; Kaifler and Kaifler, 2021).

Fluorescence lidars rely on the absorption and reemission of the laser radiation by metallic atom (Na, Fe, K, Li, Ca, Ca^+) in metallic layers in the altitude range from 80 km to 105 km, which originate from the ablation of meteors. Na atoms in this altitude range experience a natural excitation, resulting in the emission of a faint glow at a wavelength of 589 nm, commonly referred to as Na-D line. Atmospheric temperature and wind can be inferred from measurements of the Doppler broadening and shift of the Na-D line following the artificial stimulation of Na atoms by the laser radiation of a Na lidar (e.g. Fricke and von Zahn, 1985).

Another lidar technique for measuring the atmospheric temperature below 30 km is the Raman lidar. These lidars are based on Raman scattering, an inelastic scattering process that involves a change of the wavelength of the reemitted radiation due to a change of the vibrational-rotational energy of the scattering molecule.

The invention of the first laser, a ruby laser, in 1960 by Theodore Maiman (Maiman, 1960) promoted the technique of lidars and a whole new branch of atmospheric research using lidar for profiling the atmosphere. The first atmospheric observations with a ruby

laser as light source between 60 km to 140 km were reported in the early 1960s (Fiocco and Smullin, 1963) while the first Na lidar observations of temperature observations of the MLT region were made shortly after (Bowman et al., 1969).

The principle of using light for the profiling of the atmosphere already goes back to the 1930s when searchlight beams were used for measuring atmospheric density profiles (Synge, 1930; Johnson et al., 1939) and cloud base heights (Middleton, 1939). Following, Elterman (1953) used density measurements based on the searchlight technique to derive atmospheric temperature profiles up to 67 km altitude.

Kent and Wright (1970) calculated temperature profiles from one of the first lidar systems analogously to the approach from Elterman (1953). A method for calculating temperature from Rayleigh lidar backscatter profiles was later developed by Hauchecorne and Chanin (1980).

Table 2.1.: Examples of past campaigns operating airborne Rayleigh, Na and / or Raman for middle atmospheric research

Year	Campaign & Aircraft	Lidar	Altitude (km)	Location	Literature
1983	- NCAR Electra	Na	-	USA	Kwon et al. (1990)
1986	- NCAR Electra	Na	82-105	USA	Kwon et al. (1990)
1990	**ALOHA-90** NCAR Electra	Na, Rayleigh	80-105 25-55	USA, Hawaii	Gardner (1991)
1991	**EASOE** ARAT-Fokker 27	Rayleigh (LEANDRE)	8-25	Scandinavia	Godin et al. (1994)
1993	**ALOHA-93** NCAR Electra	Na	80-100	USA, Hawaii	Gardner (1995)
1999-2000	**SOLVE**	Rayleigh, Raman (AROTEL)	12-60 12-25	Scandinavia	Burris et al. (2002)
2014	**DEEPWAVE** NCAR Gulfstream V	Rayleigh, Na	20-60 75-100	New Zealand, Southern Ocean	Fritts et al. (2016)
2019	**SOUTHTRAC** HALO	Rayleigh (ALIMA)	20-80	Southern Andes, Antarctic Peninsula	Rapp et al. (2021)

In the 1970s then, lasers with doped crystalline lattices, namely the Neodymium-Doped Yttrium Aluminum Garnet (Nd:YAG), entered the market and were used for lidar (e.g. Hauchecorne, 1995). The Nd:YAG laser was developed in 1964 by a team from the Bell Laboratories (Geusic et al., 1964) quiet soon after the invention of the ruby laser by Maiman (1960). The doped Nd atoms are responsible for the lasing process of the Nd:YAG crystal and emit light at a $\lambda = 1064$ nm, which can be frequency doubled to generate a $\lambda = 532$ nm or at higher harmonics. Harmonics generation is a nonlinear optical process which involves the interaction of intense longer λ laser light with a nonlinear optical crystal. Using a smaller λ for Rayleigh lidars increases the backscattered signal while maintaining the same laser power due to the λ^{-4} dependency of Rayleigh scattering. Today, Nd:YAG laser are most commonly used for Rayleigh backscatter lidars because of their high pulse energy at comparatively low costs.

Some examples of ground-based lidars for middle atmospheric research are the COmpact Rayleigh Autonomous Lidar (CORAL) in Tierra del Fuego, Argentina (e.g. Kaifler et al., 2020b; Kaifler and Kaifler, 2021; Reichert et al., 2021)[8], the Arctic Lidar for Middle Atmosphere Research (ALOMAR) in Norway (e.g. von Zahn et al., 2000; Baumgarten, 2010), the Rayleigh-Mie-Raman (RMR) in Kühlungsborn, Germany (e.g. Gerding et al., 2016) and the RMR Lidar Température et Aérosols (LTA) at the Observatoire de Haute-Provence, France (e.g. Wing et al., 2018b; Wing et al., 2018a) and the Purple Crow Lidar (PCL) in Western Ontario (e.g. Sica and Haefele, 2015).

The airborne operation of lidars became established for middle atmospheric research since the 1980s (Kwon et al., 1990). The deployment of airborne lidar for middle atmosphere research has certain limitations, such as cost, aircraft availability, flight logistics, and instrument stability, and thus requires careful planning, coordination, and resources. The airborne operation of a lidar offers several advantages compared to a ground-based lidar when conducting middle atmospheric research:

1. **Mobility and targeted observations**: Airborne lidar offers the flexibility to conduct targeted observations in specific regions of interest. Researchers can strategically plan flight paths to target remote regions or specific atmospheric features, such as mesoscale meteorological events. This mobility allows for adaptive sampling and focused investigations.

2. **Spatial resolution**: Airborne lidar provides horizontally resolved observations in extended regions with high spatial resolution. This horizontal resolution enables researchers to capture the horizontal and vertical structure of atmospheric phenomena.

   Especially, the horizontal structure of stationary MWs becomes observable using airborne lidar. Stationary MWs are characterized by $c_{px} = 0$ and $\omega = 0$ and exhibit horizontal phase lines in time-height cross-sections of ground-based lidar observations (e.g. Dörnbrack et al., 2017).

[8]You can find observations from CORAL here.

3. **Time scale**: Airborne lidar allows for measurements over large spatial regions in a time frame much shorter than the ambient large scale atmospheric motions such that these large-scale processes are observable.

4. **Proximity to the middle atmosphere**: The laser beam of an upward pointing airborne lidar experiences less attenuation due to Rayleigh extinction in the troposphere as in ground-based systems because airborne instruments are typically operated at flight altitudes with a significant fraction of the air mass below. Furthermore, the proximity of an airborne lidar to the middle atmosphere causes stronger backscattered signals due to a larger solid angle $\Delta\Omega$ (see Fig. 2.4)

5. **Cloud independency**: An upward-pointing airborne lidar is not affected by tropospheric clouds if the flight altitude is above the cloud top heights.

6. **Campaign-based studies**: Airborne lidar enables researchers to conduct focused measurement campaigns in specific regions or during particular atmospheric events. This capability is particularly useful for studying dynamic phenomena or conducting coordinated measurements alongside other airborne instruments, such as in-situ sensors or remote sensing devices.

7. **Validation and calibration**: Airborne lidar can serve as a valuable tool for validation and calibration of spaceborne measurements. By flying underneath satellite orbits, airborne measurements can be compared and correlated with spaceborne data, helping to assess the accuracy and performance of space-based instruments.

Examples of past airborne campaigns using an airborne Rayleigh, Na and / or Raman lidar are listed in Table 2.1.

2.4.2. The lidar equation for airborne application

The physics of a detected lidar signal from an airborne application of an upward-pointing Rayleigh lidar can be described by the lidar equation (Fujii, 2005; Weitkamp, 2005):

$$P_R(\lambda,z) = \Bigg(\underbrace{P_L(\lambda)}_{I} \cdot \Big(\underbrace{\sigma_{mol}(\lambda) \cdot \frac{R_d \cdot \rho(z)}{k_B} + \sigma_{aer}(\lambda) \cdot N_{aer}(z)}_{II} \Big) \cdot \underbrace{\mathrm{d}z}_{III} \cdot \underbrace{e^{-\tau_{Ray}(\lambda,z)-\tau_{o3}(\lambda,z)}}_{IV} \cdot \underbrace{\frac{A}{(z-z_L)^2}}_{V} \cdot \underbrace{\eta_{FOV}(z)}_{III} + \underbrace{P_{BG}(z)}_{VI} \Bigg) \cdot \underbrace{\eta_{trans} \cdot \mathrm{d}t \cdot f_{rep}}_{III} \tag{2.22}$$

where $P_R(\lambda, z)$ is the count rate of backscattered photons per laser pulse and at an altitude z for a given laser wavelength λ.

The lidar equation (Eq. 2.22) takes into account the technical setup of the lidar (terms *I*, *III* and *V*), the atmospheric conditions and ability to backscatter the emitted laser pulses (terms *II* and *IV*) and the contribution of the background (term *VI*).

Term I depicts the number of initially emitted photons by the laser per pulse:

$$P_L(\lambda) = \frac{E \cdot \lambda}{h \cdot c} \tag{2.23}$$

with E being the laser pulse energy and h the Plank constant.

The term III includes the lidar system parameters $\mathrm{d}z$ as vertical bin resolution, η_{FOV} being the efficiency of the Field Of View (FOV) which describes how well the laser beam is aligned with the FOV of the receiver, η_{trans} being the optical efficiency of all lidar components included in the transmission and detection of the backscattered signal within the receiver unit, $\mathrm{d}t$ as integration period and f_{rep} as pulse repetition frequency. The lidar geometry, namely the solid angle $\Delta\Omega$ for an airborne application, with A being the lidar telescope area and $z_L(t)$ the altitude of the lidar, is given by the term V. The solid angle expresses the lidar telescope perception of the fraction of the spherical wave created by scattering of light at a particle at an altitude z (Fig. 2.4). On the one hand, a large $\Delta\Omega$ allows a lidar system to collect more scattered photons. This results in an improved collection efficiency, a higher Signal-to-Noise Ratio (SNR) and statistical accuracy. On the other hand, a large $\Delta\Omega$ requires a large receiving telescope which is difficult to fit into an aircraft. The solid angle is the only term that is different in the lidar equation for an airborne application compared to a ground-based application. The flight altitude of an aircraft (as platform of the lidar), namely z_L, varies in the course of a flight compared to the constant altitude of a ground-based lidar.

The interaction of the laser photons with the atmosphere is described by the backscatter coefficient $\beta(\lambda, z)$ (the scattering coefficient for the scattering angle of 180°) which is depicted by term II in the lidar equation (Eq. 2.22), where R_d is the gas constant of dry air, k_B is the Boltzman constant, $\rho(z)$ is the atmospheric density and $N_{aer}(z)$ is the number density of aerosols. Generally, $\beta(\lambda, z)$ of the atmosphere includes contributions from molecular (mol) and particulate scattering (aer), thus mainly Rayleigh and Mie scattering, respectively:

$$\begin{aligned} \beta(\lambda, z) &= \beta_{mol}(\lambda, z) + \beta_{aer}(\lambda, z) \\ &= \sigma_{mol}(\lambda) \cdot N_{mol}(z) + \sigma_{aer}(\lambda) \cdot N_{aer}(z) \end{aligned} \tag{2.24}$$

with $\sigma_{mol}(\lambda)$ and $\sigma_{aer}(\lambda)$ as molecular and particulate backscattering cross sections, respectively. The molecular (Rayleigh) backscattering cross section is derived from the total scattering cross section $\sigma_{mol,tot}(\lambda)$ as:

$$\begin{aligned} \sigma_{mol}(\lambda) &= \frac{1}{4\pi}\frac{3}{2}\sigma_{mol,tot}(\lambda) \\ &= \frac{1}{4\pi}\frac{3}{2} \cdot 5.16 \cdot 10^{-32}\ \mathrm{m}^{-2} = 6.16 \cdot 10^{-32}\ \mathrm{m}^{-2} \end{aligned} \tag{2.25}$$

for $\lambda = 532$ nm (Bucholtz, 1995). Particulate backscattering is highly variable in space and time, whereas molecular scattering originates mainly from N_2 and O_2 and thus depends mainly on the atmospheric density since the atmosphere is well mixed with respect to its main constituents below approximately 100 km. The large dynamic range

of a lidar signal with an upward-pointing laser beam with altitude is primarily caused by the density decrease with altitude and secondarily caused by the quadratic dependence of the solid angle.

Term *IV* describes the atmospheric transmission, namely it takes the round-trip extinction of the laser beam into account, which is given by the optical depth τ. The major contributions to the round-trip extinction at $\lambda = 532$ nm are the Rayleigh extinction $\tau_{Ray}(\lambda, z)$ and the absorption by ozone (O_3) $\tau_{O_3}(\lambda, z)$:

$$\tau_{Ray}(\lambda, z) = 2 \cdot \frac{R_d}{k_B} \cdot \sigma_{mol,tot}(\lambda) \cdot \int_{z_L}^{z} \rho(z') \cdot \delta z' \tag{2.26}$$

$$\tau_{O_3}(\lambda, z) = 2 \cdot \sigma_{O_3}(\lambda) \cdot \int_{z_L}^{z} N_{O_3}(z') \cdot \delta z' \tag{2.27}$$

with the ozone absorption cross section $\sigma_{O_3}(\lambda)$ and the number density of O_3 (Voigt et al., 2001).

Finally, the photon background contribution is considered in term *VI*. The photon background on the one hand includes foreign light sources as the sun at daytime, the moon and stars at nighttime, as well as artificial light sources excluding the laser transmitter. On the other hand it includes the dark counts from the detectors (the dark current) and the signal induced noise. The photon noise is a statistical fluctuation that is a consequence of the quantum nature of photons, which becomes noticeable in particular at low signal levels. The signal induced noise is a source of nonlinear noise that results from signal induced physical changes within the detector, e.g. the heating of the semiconductor junction due to the current flowing across the junction in the Avalanche Photodiodes (APD). The ratio of the desired photon signal to the photon background contribution due to the dark current is quantified through the SNR and can be calculated as:

$$\mathrm{SNR}(z) = \frac{P_R(\lambda, z) - P_{BG}(z)}{\sqrt{P_R(\lambda, z)}} \tag{2.28}$$

2.4.3. The hydrostatic temperature retrieval

Making the assumptions discussed below, the lidar equation (Eq. 2.22) can be reduced to:

$$P_R(\lambda, z) = \frac{C}{(z - z_L)^2} \cdot \sigma_{mol} \cdot N_{air}(z), \tag{2.29}$$

where C summarizes the lidar system parameters to an unknown constant and $\sigma_{mol} \cdot N_{air}(z)$ depicts the molecular Rayleigh backscatter with $N_{air}(z)$ as number density of air. Consequently, the lidar backscatter profiles relate to the atmospheric density as:

$$P_R(\lambda, z) \cdot (z - z_L)^2 \propto N_{air}(z) \propto \rho(z). \tag{2.30}$$

The reduced expression of lidar equation (Eq. 2.29) and the proportionality given by Equation 2.30 are only valid under the following conditions:

1. **In the absence of aerosols**: It is assumed that only molecular Rayleigh scattering contributes to the lidar backscatter profiles. Aerosols prevail in the middle atmosphere below 30 km (Junge et al., 1961), where they play a role in the radiative balance of the atmosphere and in the formation of Polar Stratospheric Clouds (PSCs) (Kremser et al., 2016). Aerosols also prevail in the upper mesosphere, where they influence the formation of Polar Mesospheric Clouds (PMCs) (Gadsden, 1982) and polar mesosphere summer echoes (PMSE; Rapp and Lübken, 2004). If these aerosols contribute to the lidar backscatter profile, the latter is not directly proportional to $\rho(z)$ anymore and causes an increase in $\rho(z)$ and cold bias in $T(z)$.

2. **With accounted atmospheric transmission**: Rayleigh scattering and the photodissociation of ozone caused by molecular absorption in the Chappuis band ($400 \leq \lambda \leq 650$ nm) are the major contributions of the altitude-dependent round-trip laser beam attenuation for e.g. a laser λ of 532 nm. The application of a transmission correction based on Equations 2.26 and 2.27 eliminates the impact on the lidar backscatter profiles.

3. **With accounted lidar system parameters**: Further corrections are suggested to reduce the impact of C on the proportionality, namely, a background correction and a dead time correction.

The mentioned corrections (transmission, range, background and dead time) applied to P_R will be elaborated in Section 3.2.1.

Assuming that the atmosphere is in hydrostatic equilibrium

$$\mathrm{d}p = -\rho(z) \cdot g(z) \cdot \mathrm{d}z \tag{2.31}$$

and obeys the ideal gas law (Eq. 2.5), the lidar backscatter profiles can be converted to temperature profiles by integration (Kent and Wright, 1970; Hauchecorne and Chanin, 1980):

$$T(z) = -\frac{M}{k_B} \cdot \left(\int_{z_L}^{z_0} \frac{\rho(z')}{\rho(z)} \cdot g(z') \cdot \mathrm{d}z' + \int_{z_0}^{\infty} \frac{\rho(z')}{\rho(z)} \cdot g(z') \cdot \mathrm{d}z' \right), \tag{2.32}$$

with M being the mean molecular mass of air which originates from $\rho(z) = k_B N_{air}(z) = N_{air}(z)M$. Equation 2.32 is split into two integrals where z_0 is the highest altitude with acceptable SNR. The second integral covers altitudes with noise dominating any signal and is, therefore, assumed to be equal to the conditions at z_0. This yields:

$$T(z) = \frac{\rho(z_0) \cdot T(z_0)}{\rho(z)} + \frac{M}{k_B} \cdot \int_{z_0}^{z_L} \frac{\rho(z')}{\rho(z)} \cdot g(z') \cdot \mathrm{d}z'. \tag{2.33}$$

The temperature integration is performed top-down with initialization conditions $T(z_0)$ which have to be estimated, e.g. from proximate satellite measurements (e.g. Alexander et al., 2011; Kaifler and Kaifler, 2021), other lidar observations (e.g. Rauthe et al., 2006; Rauthe et al., 2008), or climatology (e.g. Hauchecorne and Chanin, 1980). The a-priori temperatures may only accord to a varying degree with the actual temperatures

at the time of the lidar sounding because of the different temporal resolutions, the geographic validity or because the measurement took place at a different point in time. Advantageously, uncertainties related to the initialization conditions decrease exponentially with decreasing altitude in the top-down approach because of the $\rho(z)^{-1}$ dependence in Equation 2.33.

To be precise, a local hydrostatic equilibrium and a local thermodynamic equilibrium are assumed for the validity of Equation 2.32 and 2.33 (Wing et al., 2018b). Both assumptions are potentially problematic, especially for GW measurements. The effects of non-hydrostatic modes on the temperature retrieval will be explored in Section 3.4.

3. Detailed analysis of the error budget of the Airborne Lidar for Middle Atmospheric research

In September 2019, ALIMA made its debut aboard the research aircraft High Altitude and Long Range (HALO) and inaugurated a new era in middle atmospheric observation. The novel instrument ALIMA is the outcome of advances in the laser technology of the last 20 years. ALIMA's deployment markes a critical step towards unveiling the secrets of the middle atmosphere and for advancing the understanding of its dynamics.

New instruments inherently present unknown uncertainties and biases. The detailed analysis of the error budget of ALIMA is inevitable for the accurate quantification of uncertainties, establishing a foundation for the reliable utilization and interpretation of the acquired observational data of ALIMA.

3.1. The ALIMA instrument

ALIMA is a novel instrument for middle atmospheric research developed by Deutsches Zentrum für Luft- und Raumfahrt (DLR) for the airborne operation onboard the German research aircraft HALO. Head scientist and developer of the lidar is Bernd Kaifler. He operated the instrument during the SouthTRAC-GW campaign in September 2019, provided the main retrieval code, the binned lidar backscatter profiles and retrieved standard temperature profiles.

Figure 3.1 shows the principle setup of ALIMA as it was operated during SouthTRAC-GW. A laser test of ALIMA and the transmitter and receiver unit onboard HALO are shown in Figures 3.2a and 3.2c. Figure 3.2b illustrates how one can imagine the airborne measurements by ALIMA as atmospheric curtains dragged behind the laser beam. The main technical parameters of ALIMA are summarized in Table 3.1. Parts of this Section 3.1 can be found in Knobloch et al. (2022).

Transmitter and receiver

The transmitter (laser box; Fig. 3.1) of ALIMA consists of a diode-pumped and pulsed Nd:YAG laser. The initial λ of the laser is frequency-doubled (secondary harmonic generation) to $\lambda = 532$ nm. The laser pulses are then directed to the center of the window in the aircraft's ceiling, where a smaller window is embedded as outlet of the laser beam.

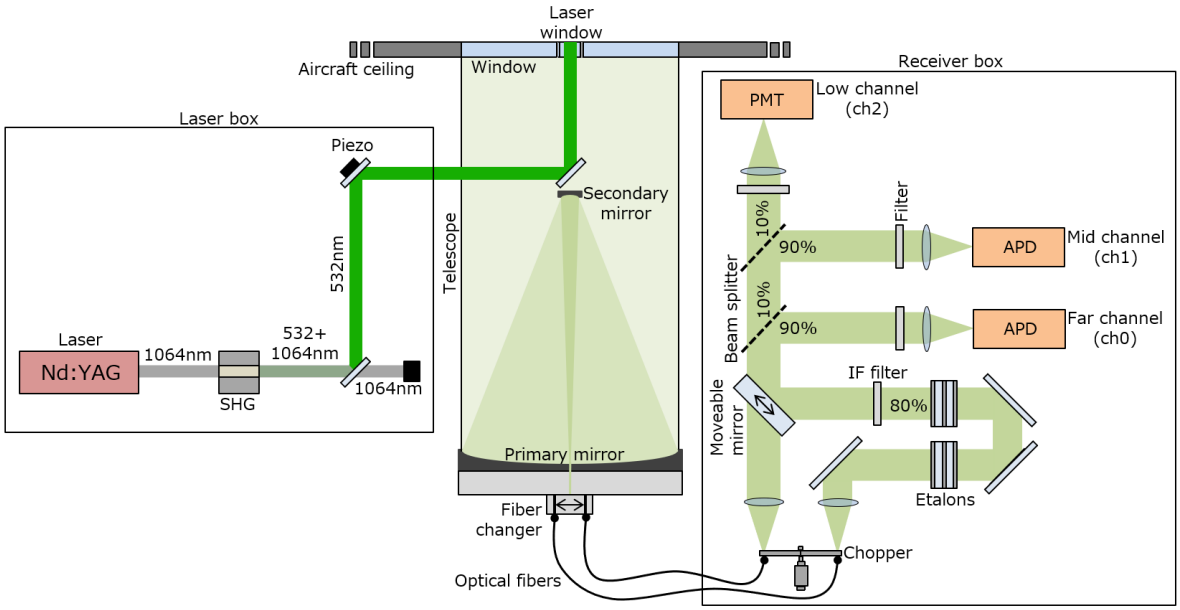

Figure 3.1.: Schematic illustration of the ALIMA instrument as used during the SOUTHTRAC-GW campaign 2019.

ALIMA's primary range resolution is dicated by the duration of the laser pulses τ_p of 8 ns, which corresponds to a length of 2.4 m. The finest possible horizontal resolution is determined by the velocity of the aircraft and f_{rep} of 100 Hz. With typical ground speeds GS_{HALO} ranging between 200 ms^{-1} to 300 ms^{-1}, the horizontal resolution limit is between 2 m to 3 m. However, the measurements have to be binned to coarser resolutions to increase the SNR.

The first major component of the receiver unit is the telescope collecting backscattered photons with a primary parabolic mirror at the bottom and a hyperbolic mirror at the top (Cassegrain telescope). The collected photons are focused into an optical fiber, which connects the telescope with the second major component of the receiver unit, the optical bench.

The beam of collected photons passes a mechanical chopper which blocks the fraction of photons from the lowest altitudes in order to protect the detectors from saturation by very strong signals. The beam is then split by two beam splitters with a transmission of 10 % into three elastic detector channels: two channels (far channel – *ch0* and mid channel – *ch1*) are equipped with APDs; and one channel (low channel – *ch2*) uses a Photomultiplier Tube (PMT) as detector. The far channel receives 90 %, the mid channel 9 % and the low channel 1% of the collected photons. All channels use narrowband interference filter in front of the detectors to reduce the broadband photon background. The splitting of the lidar return signal into different channels is necessary because the strength of the lidar signal changes by more than eight orders of magnitudes from 20 km to 90 km and thus exceeds the dynamic range of a single detector.

The optical bench consists of two branches, a nighttime branch and a daytime branch.

Table 3.1.: Technical parameters of the transmitter and receiver unit of the ALIMA system and data processing parameters.

Transmitter	
Laser pulse energy E	140 mJ
Laser pulse duration τ_p	8 ns
Laser pulse length	2.4 m
Laser pulse repetition frequency f_{rep}	100 Hz
Laser wavelength λ	532 nm
Primary vertical resolution $\Delta z'$	2.4 m
Receiver	
Telescope area A	0.18 m^2
Telescope diameter d	0.48 m
Transmission efficiency η_{trans}	0.239
Surfaces	0.477
Quantum efficiency of detectors	0.5
Dead time of detectors τ_D	22 ns
Dark current rate	10 - 30 Hz (The dark current rate varies from detector to detector)
Operation	
Ground speed HALO GS_{HALO}	200 - 300 ms^{-1}
Primary horizontal resolution $\Delta x'$	2 - 3 m
Processing	
Vertical resolution Δz	100 m
Temporal resolution Δt	10 s

The latter includes an optical circuit with etalons and additional interference filters. These are needed to filter other wavelengths of the solar radiation from the desired signal. A fiber changer at the telescope and a movable mirror at the junction of the two optical branches is used to switch between the daytime and nighttime branches.

The number of backscattered photons arriving at the aircraft's window does not equal the number of photons that are detected. Losses occur due to imperfect optical coatings of the window, telescope mirrors and receiver optics. The refractive index of the optical components determines the transmission efficiency of the receiver. The refractive index changes twice for glass components, e.g. laser and telescope windows and lenses, and once for mirrors. Overall, 28 optical surfaces, e.g. on windows, telescope, dichroic mirror, lenses, beam expander, optical fibers and interference filters, with transmissions between 80 % and 99.5 % are incorporated in the optical transmission of the receiver. Taking into account the quantum efficiency of the detectors (e.g. quantum yield of the photocathode

of a PMT) being smaller than one, the detected light intensity is reduced compared to the incoming light intensity according to the efficiency value η_{Trans}.

In total, within the ALIMA system, only 23.9 % of the incoming photons are converted into an electrial system due to various losses (Tab. 3.1). A potential nonlinear behavior of the detectors may cause an additional reduction of the detected photon counts (reduced photon detection efficiency). Nonlinearity causes the number of incident and counted photons to be unproportional. One contributing factor is the potential pileup of pulses as consequence of the deadtime of the detectors. Another factor is signal-induced noise. Typically, the nonlinear behavior cannot be neglected anymore if the photon count rates exceed approximately 1 MHz. Experiments in the laboratory showed that the commonly used procedures for correcting dead-time effects work well for the detectors used in ALIMA ($\tau_D < 22$ ns) until about 5 MHz. For that reason, maximum count rates are generally limited to 5 MHz with the help of the chopper and through gating of the detectors.

Vibrations of the aircraft potentially influence the co-alingment of the laser beam and the FOV of the telescope. However, as long as both components vibrate in the same frequency and phase, the system appears balanced. In case of ALIMA, the receiving telescope and laser transmitter are mounted on a common platform which is vibrationally isolated from the aircraft frame through the use of shock mounts.

3.2. Data processing

In the processing of the photon dataset, the detected photon count profiles are stored in discrete predefined bins with a temporal resolution Δt of 10 s, which involves 1000 laser pulses, and with a vertical resolution Δz of 100 m. The profiles cover all altitudes up to 300 km, however bins with altitudes smaller z_L will be set to Not a Number (NaN). Following, various corrections are applied to the photon counts profiles which are afterwards used to retrieve atmospheric temperatures.

3.2.1. Corrections

So far, P_R was expressed for one laser pulse or a sum of laser pulses representing one time step (one measurement) depending on λ and z. The following corrections will now be expressed for time-dependent P_R(t, z) curtains. The corrections are implemented in the retrieval code and are applied by default. A transmission correction for O_3 absorption is currently not implemented (see Section 3.3 for more details about an ozone absorption correction).

Background removal

The $P_{BG}(t, z)$ contribution can be estimated from the lidar backscatter profiles above approximately 110 km altitude where the lidar signal due to Rayleigh backscattering becomes negligible. The time scales of variations of $P_{BG}(t, z)$ are larger than the round-trip time of the laser pulses and, thus, they constitute a background which is constant

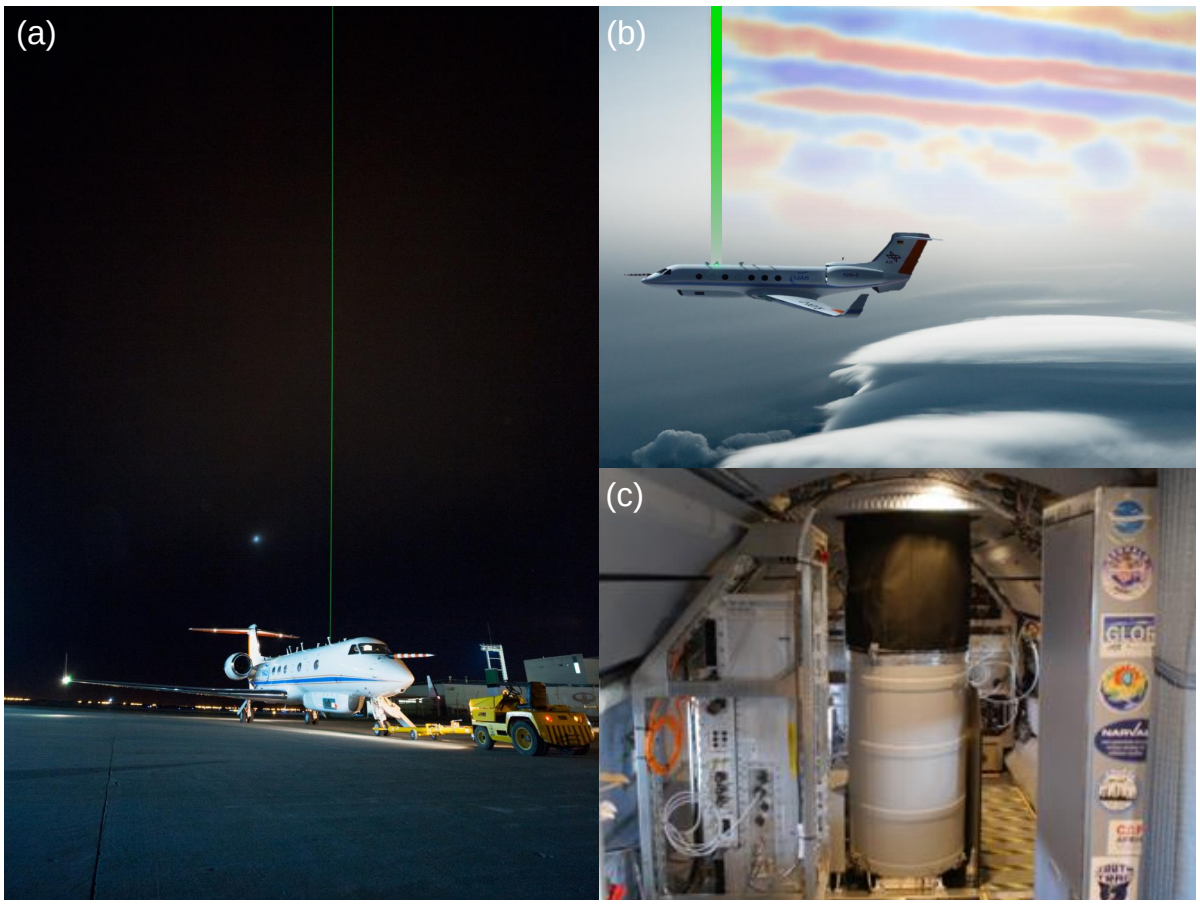

Figure 3.2.: (a) HALO with switched on ALIMA and its visible laser beam at the airport in Rio Grande, Argentina. Photography by BigAir, DLR. (b) Photo composition of the operation of ALIMA during a flight und illustrate the airborne lidar technique measuring atmospheric curtains. Background photography by BigAir, DLR; overlaid temperature perturbations are measurements from research flight ST08. (c) Setup of ALIMA in HALO with the telescope in the middle and the laser and receiver unit in the left rack. Photography by Andreas Minikin.

with altitude (Keckhut et al., 1990). With ALIMA, photon counts are received up to 300 km altitude. The thermospheric altitude range is used to precisely measure $P_{BG}(t,z)$. $P_{BG}(t,z)$ is evaluated between 125 km to 190 km altitude for the far channel and between 115 km to 180 km altitude for the mid and low channels.

Based on the assumption of a constant background with altitude, an average $\overline{P_{BG}(t)}$ is estimated an subtracted:

$$P_{R,BGC}(t,z) = P_R(t,z) - \overline{P_{BG}(t)}. \tag{3.1}$$

Range correction

The photon count profiles have to be scaled by the inverse of the range term in order to ensure the proportionality of equation 2.30:

$$P_{R,RC}(t,z) = P_R(t,z) \cdot (z - z_L(t))^2. \tag{3.2}$$

The range term is time-dependent for the airborne operation in contrast to a ground-based operation and has to be determined for each photon count profile individually. The range correction compensates the decrease in signal strength with altitude due to the decrease of the solid angle $\Delta\Omega$.

Dead time correction

An ideal detector operated in single photon counting mode should obey a linear behavior (Donovan et al., 1993). However, nonlinearity can appear in the detector's response, which leads to the ratio of incident and detected photons being dependent on the rate of the incident photons. Above certain rates of incident photons, it becomes increasingly likely that a photon arrives at the detector during the dead time following the detection of a previous photon. As a consequence, the new photon is not detected and the detection efficiency decreases with increasing photon incident rates. The nonlinearity caused by the dead time can become especially noticeable at lower altitudes with larger signals.

To mitigate the effect of the dead time of the APDs and PMT, a dead time correction is applied to the counted photon profiles which scales the counted photon profiles for compensation of dead time effects (e.g. Polyakov, 2013):

$$P_{R,DTC}(t,z) = \frac{P_R(t,z)}{(1 - P_R(t,z) \cdot \tau_D)}. \tag{3.3}$$

The equation above describes a *nonparalyzed model* which is a theoretical model and assumes that the detector is nonparalyzed. Non-paralyzable detectors are unable to detect any other photon arriving during the dead time, so that with an increasing rate of incident photons the detector will reach a saturation equal to τ_D^{-1}.

Note that the reason for splitting the lidar return signal into different channels is not only given by the desire to increase the measurable dynamic range but also to ensure that the rate of incident photons stays approximately 10 times below the maximum detectable rate $\approx \tau_D^{-1}$. In this regime the nonlinearity can be approximated using Equation 3.3 and, after correction, linearity can be assumed.

Rayleigh extinction

The correction for the effect of atmospheric transmission, the extinction of the laser beam due to Rayleigh extinction, is based on the Equation 2.26:

$$\tau_{Ray,REC}(t,z) = 2 \cdot \frac{R_d}{k_B} \cdot \sigma_{mol,tot}(\lambda) \cdot \rho_{ref}(t)^{-1} \cdot \int_{z_L}^{z} P_R(t,z') \cdot \delta z', \tag{3.4}$$

where the air density is estimated based on the relative density from ALIMA measurements and the reference density ρ_{ref} from e.g. satellite observations or climatology. Since $P_R(t,z)$ itself is influenced by Rayleigh extinction, the correction scales the photon count profiles for the atmospheric transmission by Rayleigh extinction and sets the profiles relative to the reference altitude z_{ref}:

$$P_{R,REC}(t,z) = \frac{P_R(t,z) \cdot e^{-\tau_{Ray,REC}(t,z_{ref})}}{e^{-\tau_{Ray,REC}(t,z)}}. \tag{3.5}$$

It is important that z_{ref} is high enough to be at altitudes where the Rayleigh extinction is negligible. Thus, the altitude-dependent atmospheric transmission due to Rayleigh extinction can be sufficiently removed.

With all corrections applied, the proportionality of the photon count profiles to atmospheric density (Eq. 2.30) is ensured with a high probability. The scaled and range-corrected backscatter profile can already be used for atmospheric investigations, e.g. as done in Chapter 5. However, one has to keep in mind that the scaled and range-corrected backscatter profile depicts the relative atmospheric density. That means it still lacks a reference and has to be scaled to a reference density if the variable shall be used as absolute atmospheric density.

3.2.2. Temperature retrieval

The atmospheric temperature is retrieved from the scaled and range-corrected backscatter profiles following Equation 2.33 (see Section 2.4.3). The following procedure (see Kaifler and Kaifler, 2021) is executed for all three detector channels individually. The resulting three temperature profiles retrieved from the corresponding scaled and range-corrected backscatter profiles are afterwards merged into a single temperature profile spanning the full altitude range.

First, the photon count profiles are vertically smoothed to an effective vertical resolution in order to improve the SNR. Typical filter widths are 900 m or 1500 m depending on the quality of the data and the planned investigation. In this thesis, only ALIMA data with 900 m resolution are used. A spectral examination of vertical scales indicated that for a reasonable temporal resolution of $\Delta t = 1$ min, the signal approaches the noise floor for vertical scales of approximately 1 km to 3 km depending on the altitude (at larger vertical scale at larger altitudes). A 900 m filter width already attenuates most of the vertical scales dominated by noise (For more information on the spectral analysis see Chapter 5.2; and for results of the vertical wavenumber spectra see Appendix D). The vertical filter is applied as running mean, therefore, the vertical resolution of the binned data Δz of 100 m remains but grid points within the filter widths are not independent.

Second, the initialization conditions at the reference altitude z_0 have to be determined. Temperatures are taken from adjacent measurements by the Sounding of the Atmosphere using Broadband Emission Radiometry (SABER) instrument on the Thermosphere Ionosphere Mesosphere Energetics Dynamics (TIMED) satellite for the initialization of the far channel. The mid and low channel are initialized with temperatures from the far

and mid channel, respectively, since the channels overlap vertically. The height of z_0 is determined as highest altitude where a certain SNR is first undershoot and the number of photon counts is larger than 10 counts per 100 m bin. A SNR = 4 is used as threshold for the far channel and SNR = 8 for the mid and low channel.

Third, an iterative approach for higher temporal resolutions is started. The temperature integration is applied for a nightly mean at first. Therefore, the photon count profiles are temporally integrated to a nightly mean photon count profile and the integration is initialized with the a-priori value at z_0 determined from SABER data. The temporal integration boosts the signal and reduces the photon noise. The nightly mean photon count profile has thus the greatest SNR and the initialization happens at the greatest possible altitude. Subsequently, the photon count profiles are temporally binned with decreasing Δt of 120 min, 60 min, 30 min, 20 min, 15 min, 10 min, 4 min, 2 min and 1 min in an iterative approach. At each Δt, the temperature integration is initialized with temperatures derived from the previous larger Δt. The SNR decreases with Δt and is consistently lower or equal to the SNR of the previous iteration with larger Δt which enables this temperature initialization. This iterative approach provides initialization temperatures that are closer to the actual temperatures for the integration of high temporal resolution photon count profiles.

Similar as for the vertical resolution, the temporal integration is applied as running mean. This results in an effective temporal resolution Δt, while the actual grid spacing is 30 min, 15 min, 10 min, 5 min, 5min, 2 min, 1 min, 20 s, and 10 s, respectively.

The retrieved temperatures are stored in files with the respective acronym for their temporal and vertical resolution, e.g. T1Z900 for Δt of 1 min and Δz of 900 m, and so forth.

3.3. Testing the sensitivity of ALIMA measurements with lidar simulation

With regard to question **(1)**, the sensitivity of the retrieved temperatures to the atmospheric transmission, the temperature initialization, the photon background, photon noise and the magnitude of raw photon counts $P_R(\lambda, z)$ were investigated using simulated ALIMA measurements. The lidar simulations are based on the instrument characteristics of ALIMA listed in Table 3.1 for the flight ST08 of the SouthTRAC-GW campaign. Parts of this Section 3.3 can be found in Knobloch et al. (2022).

Equation 2.22 is used for the simulation of photon counts, where the atmospheric input of $\rho(z)$ is based on ECMWF Reanalysis v5 (ERA5) temperature data. The four-dimensional ERA5 dataset is interpolated in space and time from hourly resolved fields (0.25° x 0.25° x 137 levels) to the coordinates of the ST08 flight track with a resolution of 10 s in time (can be translated to approximately 2 km in horizontal space depending on the speed of the aircraft) and 100 m in the vertical. The smallest scales of GWs that can be represented in the lidar simulation are therefore limited by the resolution of the ERA5 data and limited to hydrostatic GWs due to the underlying hydrostatic model and

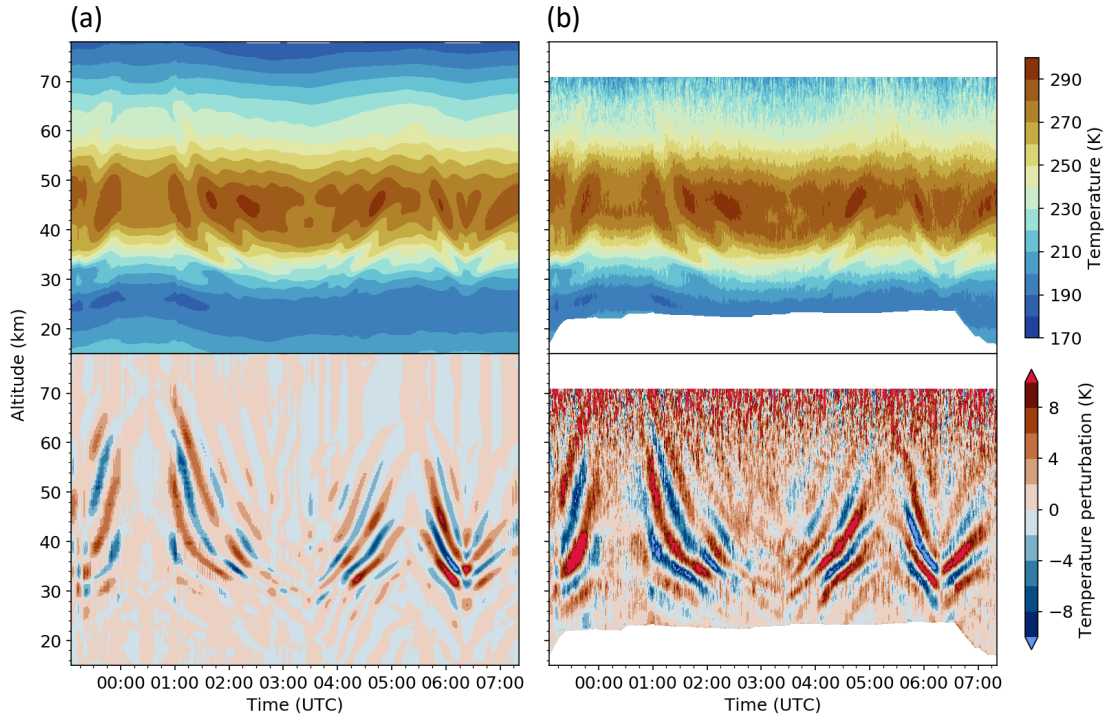

Figure 3.3.: Timeseries of temperature and temperature perturbations (derived by subtracting a 30 min running mean) along the flight track of ST08 from (a) ERA5 and (b) lidar simulation with ERA5 density as atmospheric input. Temperatures of (b) are retrieved as T1Z900. Peak amplitudes of temperature perturbations smaller than -10 K are shown in bright blue and larger 10 K in bright red.

the used data assimilation in the ERA5 model (Hersbach et al., 2020). Hence, we do not expect a perfect agreement between the measurements and model results. Difficulties in the ERA5 representation of upper stratospheric temperatures (Simmons et al., 2020) may also preclude an agreement between the ALIMA measurements and the corresponding simulations. To be clear, it is not the goal of this Section to obtain a good agreement between ERA5 data and the actual measurements performed by ALIMA. Rather, the ERA5 data are used as realistic input data for the lidar simulations.

Furthermore, two data sets for the simulation of ozone absorption are used: an ozone climatology and satellite observations. The ozone climatology by Paul et al. (1998) provides monthly mean zonal mean ozone values for 17 10° wide zonal bands at 19 pressure levels ranging from 0 km to 59 km. These ozone values are based on measurements from 30 ozonesonde stations around the world and solar backscattered ultraviolet (SBUV-SBUV/2) satellite observations. The climatological ozone profile for September for the meridional band 55°S to 65°S is employed in the calculation of the

atmospheric transmission. Additional ozone satellite measurements for the time period of ST08 were obtained from the Earth Observing System (EOS) Aura Microwave Limb Souder (MLS), which measures radiance near 240 GHz for deriving ozone between 261 hPa to 0.001 hPa.

Figure 3.3a shows the ERA5 temperature data and temperature perturbations derived by the subtraction of a 30 min running mean. Figure 3.3b shows the corresponding temperature data retrieved from simulated ALIMA measurements. The comparsion of ERA5 temperature data and resulting simulated temperature data shows the reasonable performance of the lidar simulations and the temperature retrieval. The main differences are the results of the photon noise: the increase of temperature fluctuations with increasing altitude and the apparent amplification of temperature perturbations.

Recognizing that a real lidar system inevitably produces noise due to the inherent probabilistic nature of photons (e.g. Gatt et al., 2007; Goodman, 2000), Poisson-distributed photon noise is also incorporated in the lidar simulations. In this manner, the simulated photon counts include not only the signal but also have contributions of the photon noise intrinsic to the signal, the photon background, and the dark current photons stemming from the detector. While the photon counts are computed as real numbers following Equation 2.22, simulated photon counts are subsequently converted to integers before the Poisson-distributed photon noise is added, mirroring the discrete nature of photons. Introducing photon noise into the simulation results in amplified temperature fluctuations (Fig. 3.3b). As a result, the temperature perturbations obtained from the lidar simulation exhibit a much closer resemblance to the ALIMA measurements shown in Figure A.1b than those present in the ERA5 dataset (Fig. 3.3a) despite the limited vertical altitude range and the absence of horizontal scales smaller the effective horizontal resolution of ERA5.

3.3.1. Photon background

Figure 3.4 illustrates an example of range-corrected photon count profiles observed by ALIMA during ST08. To achieve comparable photon counts, the theoretical transmission and quantum efficiency of ALIMA (Tab. 3.1), $\eta_{trans} = 0.239$, needed to be reduced to $\eta_{trans} = 0.08$ during the simulation. The decreased efficiency can be attributed to icing that occurred on the aircraft laser window during the flight or to lower transmission of the optical components due to issues with the alignment.

The ALIMA measurements exhibit a smooth transition between the signal plus background to only background contributions (Fig. 3.4). The transition can be estimated from the standard deviation σ of the timeseries of photon counts. σ becomes constant with altitude if the measured signal is only constituted by the photon background. The photon background follows a Poisson distribution for which $\sigma = \sqrt{\lambda_{PD}}$ with λ_{PD} as expected value of the photon background. Therefore, the photon background $P_{BG}(t)$ is as well constant with altitude if σ is constant. The constant σ confirms the stated assumption of a constant background (Section 3.2.1).

The photon background $P_{BG}(t)$ of the far channel exhibits a temporal variability for research flights ST08, ST09, and ST10. ST08 and ST09 were conducted under almost

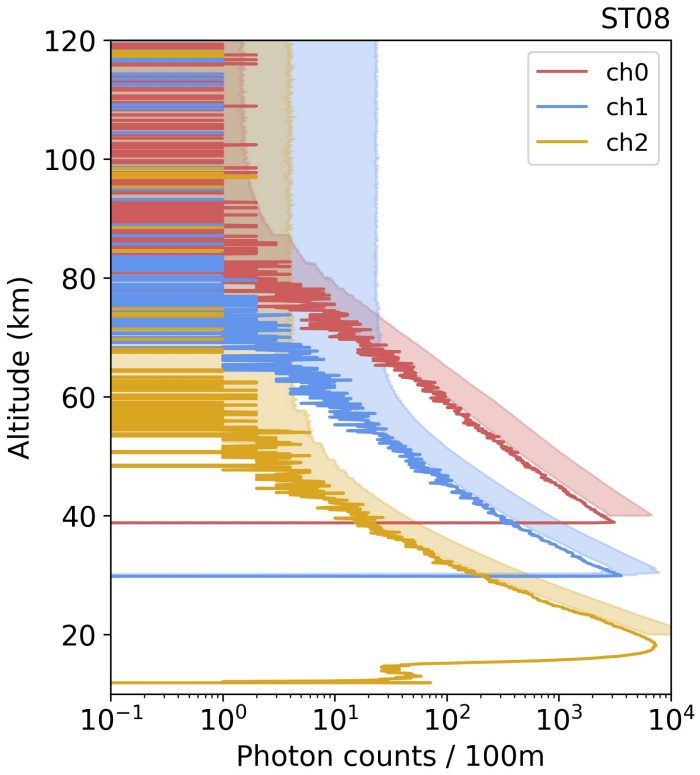

Figure 3.4.: Photon count profiles by ALIMA of the far, mid and low channel of flight ST08 of one 10 s bin at 02:00 UTC. Shaded areas indicate plus one standard deviation ($+\sigma$) of the whole time series of ST08. $-\sigma$ is omitted in the graph due to the logarithmic scale.

full moon conditions, resulting in the highest photon backgrounds (Tab. 3.2). An additional increase in the photon background during ST09 and ST10 can be explained by the occurrence of icing on the aircraft window. $P_{BG}(t)$ shows no significant temporal variability during the other flights. The lowest photon background condition occurred during ST14 which was conducted during new moon. The P_{BG} rates of the mid and low channel are generally much smaller than those of the far channel, and these only constitute a minor contribution of the photon background.

Since the altitude at which the temperature initialization occurs is determined not only by the SNR but also by the requirement of counting at least 10 photon per altitude bin, the photon background lead to minor contribution of less than 1% to 2% in photon counts at the initialization altitude during night-time flights. The influence of the photon background on the signal becomes even less significant as the signal strength increases downwards. Consequently, the photon background has a minimal impact on the uncertainty in temperature and the night-time data quality of ALIMA.

In contrast to Figure 3.4, the simulated photon count profiles exhibit a distinct disparity between above and below 78 km altitude, which is the top of the ERA5 data. The bins below 78 km altitude contain the simulated photon signal while bins above solely contain

the simulated photon background, due to the limited vertical extent of the ERA5. In order to prevent this discontinuity during the temperature retrieval, the initialization of the hydrostatic integration of simulated lidar data is restricted to altitudes below 78 km. Furthermore, the temperature retrieval for the simulated photon count profiles uses $T(z_0)$ determined from a mean temperature profile of the ERA5 temperatures along the flight track of ST08.

Table 3.2.: Temporal mean of the photon background of the six night-time research flights with ALIMA and of the simulated flight ST08 (SimST08). The periods of time before detector switch-on, take-off and landing are excluded from the calculation.

	ST08	SimST08	ST09	ST10	ST11	ST12	ST14
$\overline{P_{BG}}$ rate (per 10 s)	2801	2500	3916	2365	1531	1502	1499
$\overline{P_{BG}}$ counts (per 100 m)	0.194		0.261	0.158	0.102	0.099	0.100
Remarks	Nearly full moon		Icing, full moon	Icing			New moon

3.3.2. Atmospheric transmission

To quantitatively assess the influence of Rayleigh extinction and O_3 absorption on the retrieved temperatures, multiple lidar simulations are conducted employing different configurations. The configurations include simulations:

(v1) without considering atmospheric transmission and no correction applied in the temperature retrieval,

(v2) considering Rayleigh extinction but without a correction applied, and

(v3) considering O_3 absorption but without a correction applied.

The initial simulation **v1** serves as a reference case. It is assumed that **v1** yields the same outcome as when attenuation by Rayleigh extinction and O_3 absorption does have an impact on the laser beam and its backscattered fraction, but with ideal corrections implemented in the temperature retrieval.

Generally, the lidar simulations show that a 1 % difference in photon counts translates to a ΔT of 0.5-0.65 K.

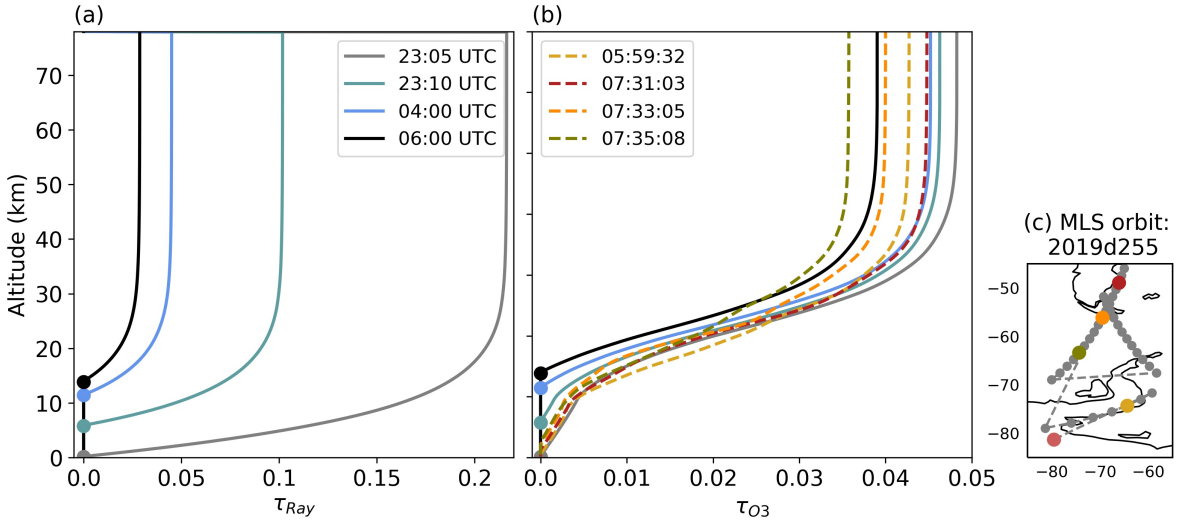

Figure 3.5.: (a) Rayleigh extinction and (b) ozone absorption for an airborne lidar with varying flight altitude. Solid lines in (b) show τ_{O_3} based on the O_3 climatology from Paul et al. (1998) and dashed lines show τ_{O_3} based on measurements from MLS shown in (c).

Rayleigh extinction

The attenuation caused by Rayleigh extinction varies with the flight altitude (Fig. 3.5a). Alterations in flight altitude during airborne lidar measurements modify the sampling volume above the aircraft. As the aircraft ascends, the number of air molecules within the sampling volume decreases, resulting in reduced interactions with the laser beam. Consequently, the influence of Rayleigh extinction diminishes at higher flight altitudes. For flight altitudes ranging from 10 km to 14 km (Fig. 3.5a, black and blue lines), the optical depth τ_{Ray} of the air masses above the aircraft reaches approximately 0.025 to 0.035, corresponding to an absolute attenuation of around 2.5 % to 3.5 %. In the case of a ground-based lidar which which corresponds to a flight altitude of 0 km in the simulations (Fig. 3.5a, grey line), the total optical depth due to Rayleigh extinction is approximately 0.21 to 0.22, resulting in a loss in photon counts of 19 % to 20 %. Above 30 km, the Rayleigh extinction becomes negligible due to the exponential decrease of air molecules with altitude.

The vertical change of attenuation is the determining factor that impacts the retrieved temperatures. Rayleigh extinction significantly affects lidar measurements below 30 km, while its impact becomes insignificant above 40 km. Figure 3.6a shows the retrieved temperatures for the different lidar simulation configurations together with the reference ERA5 temperature profile. Figure 3.6b shows the $\overline{\Delta T}$ due to Rayleigh extinction which is represented by the difference between simulation configuration **v1** and **v2**. The largest $\overline{\Delta T}$ of 1.5 K is located at the bottom of the profile at approximately 18 km and decreases to zero at approximately 30 km in accordance with the vertical change of τ_{Ray}. The small perturbations of $\overline{\Delta T}$ and the range of the standard deviation σ mainly originates from

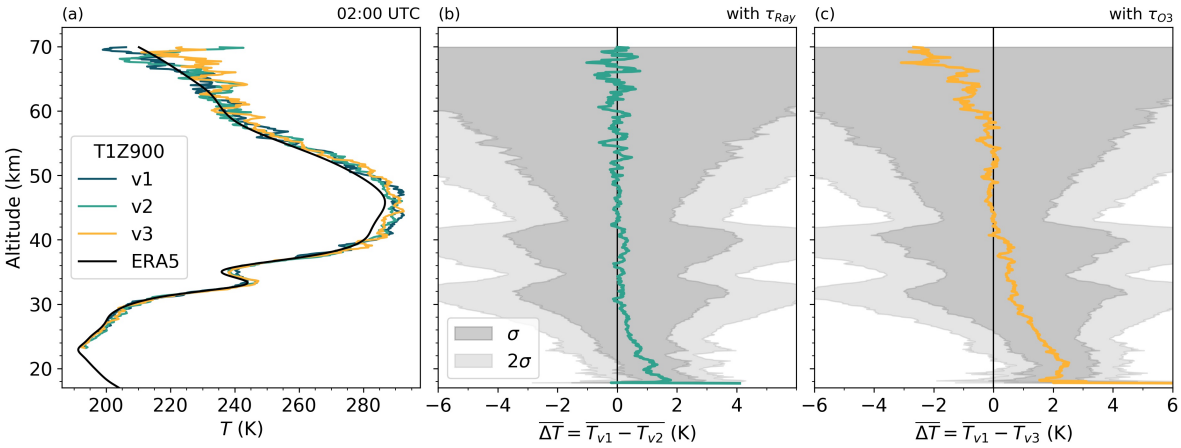

Figure 3.6.: Difference between the ERA5 temperatures and the lidar simulations v1, v2 and v3, where (a) shows the respective temperature profiles at 02:00 UTC, (b) the average difference of temperature $\overline{\Delta T}$ between v1 and v2 indicating the impact of Rayleigh extinction and (c) $\overline{\Delta T}$ between v1 and v3 indicating the impact of absorption by ozone. Dark and light grey shaded areas give one and two standard deviations of $\overline{\Delta T}$, respectively.

photon noise, smoothing and the hydrostatic integration.

Absorption by ozone

The number density of O_3, N_{O3}, peaks at about 20 km to 25 km altitude. Below, N_{O3} decreases to tropospheric values of N_{O3} of about one quarter of the peak value. The influence of absorption by ozone on the laser beam and its backscattered fraction thus depends on the flight altitude (Fig. 3.5b). Between flight altitudes and 40 km altitude, the maximum of optical depth due to absorption by ozone τ_{O3} based on the ozone climatology reaches values between 0.038 to to 0.048, corresponding to approximately 3.7 % to 4.7 % absolute change in photon counts. The lower optical depths correspond to higher flight altitudes, since less O_3 molecules are present in the observational volume at higher flight levels, therefore, less absorption by ozone attenuates the laser beam. Above 40 km, τ_{O3} becomes constant with altitude and the impact of absorption by ozone on the laser beam becomes insignificant. Here, N_{O3} profiles only up to 78 km are considered. To be mentioned, O_3 mixing ratios increase to a secondary maximum in the upper mesosphere and lower thermosphere with comparable magnitude during night-time as in the stratosphere (e.g. Evans and Llewellyn, 1972; Hays and Roble, 1973). However, absolute N_{O3} are small compared to the stratospheric maximum, and therefore, mesospheric O_3 has little impact on the transmission of the laser beam.

The calculated transmission is slightly smaller for MLS observations of O_3: the maximum of the optical depth τ_{O3} reaches 0.035 to 0.045 up to 40 km altitude, corresponding to about 3.4 % to 4.5 % absolute change in photon counts. The values of τ_{O3} based on MLS observations are all calculated for a single z_L of 0 km. For higher flight levels, the

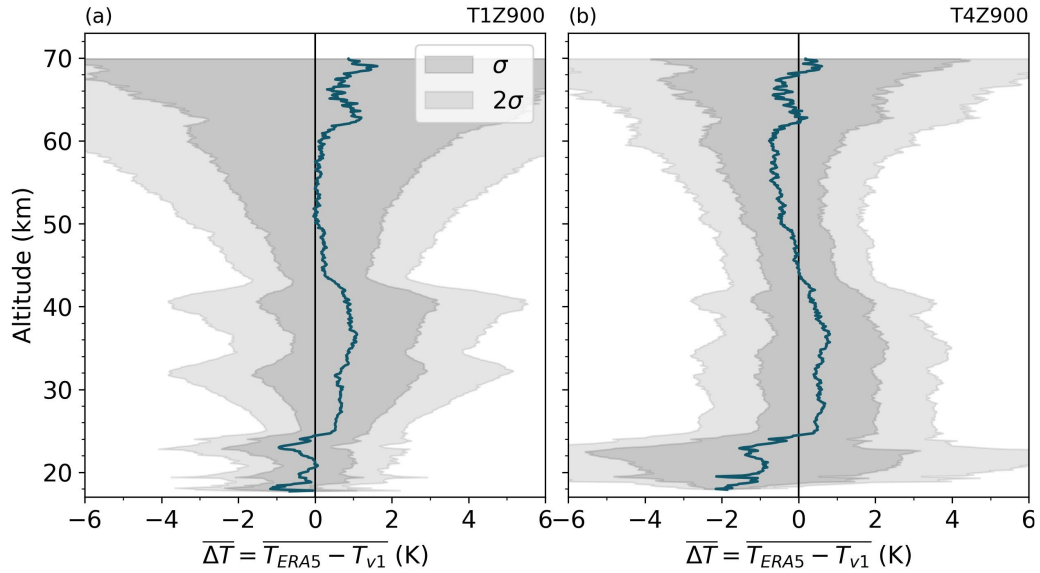

Figure 3.7.: Difference between the ERA5 temperatures and retrieved temperatures based on simulation configuration **v1** for (a) $\Delta t = 1$ min and (b) $\Delta t = 4$ min. Dark blue lines

maximum of τ_{O3} is even smaller. τ_{O3} decreases by 0.01 and photon counts increase by 1 % if the flight altitude is changed from 0 km to 14 km (grey and black lines in Fig. 3.5b). Similarly, τ_{O3} based on MLS observations drops to 2.4 % to 3.5 % for flight altitudes of 14 km.

The variability in absorption by ozone due to different flight altitudes is as distinct as the variability in absorption by ozone due to observations at different geographical locations (even though the MLS observations are partly only 2 minutes later). However, the limited factor for the retrieved temperature profiles is the variability of atmospheric transmission with altitude.

Figure 3.6c shows the $\overline{\Delta T}$ due to absorption by O_3 which is represented by the difference between the outputs of simulation configuration **v1** and **v3**. Here, the ozone climatology was used in the lidar simulation. The largest $\overline{\Delta T}$ of 2.5 K occurs at about 22 km in accordance with the largest vertical change in τ_{O3} at the same altitude. $\overline{\Delta T}$ decreases and vanishes at 40 km and beyond.

Due to the lack of sufficient N_{O3} observations and the knowledge of the distinct geographical variability of ozone, so far no correction is implemented in the temperature retrieval for ALIMA observations.

3.3.3. Photon noise

Figure 3.7 showcases the disparities between temperatures retrieved from the simulated photon count profiles with the simulation configuration **v1** and the actual temperatures taken from ERA5 data. When using short integration periods like $\Delta t = 1$ min (Fig.

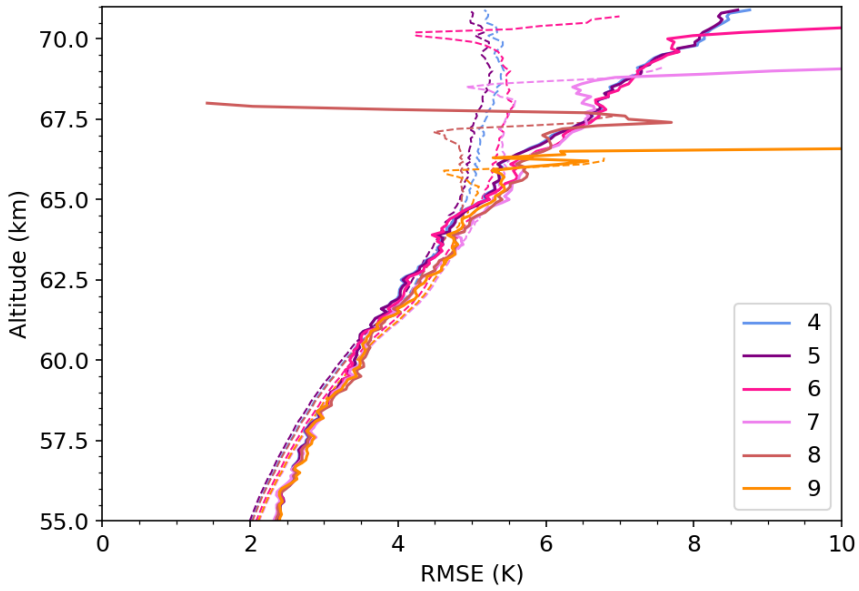

Figure 3.8.: RMSE of ΔT between retrieved temperatures from lidar simulation and ERA5 temperatures for different SNR threshold (colored lines) for the far channel. Dashed lines show the result for a simulation without the addition of Poisson-distributed photon noise. Large outliers at the top of the profiles arise due to varying number of profiles that go into statistics and should not be considered.

3.7a), there is on average an altitude-dependent temperature bias $\overline{\Delta T}$ of approximately ± 1 K. $\overline{\Delta T}$ is most prominent in the stratosphere and upper mesosphere. The standard deviation σ of ΔT features local peaks at 32 km and 40 km and increases to its maximum of ± 7 K at the top. The minimum/maximum values of ΔT peak at the top (at 70 km) with values up to at ± 25 K.

The large altitude-dependent uncertainty (spread in ΔT) arises mainly from the including photon noise in the simulations. The photon noise leads, on average, to a cold bias in the upper mesosphere (McGee et al., 1995; Thayer et al., 1997). Lower retrieved temperatures are typically observed at altitudes with weaker signal levels for smaller integration periods due to less effective smoothing of photon noise. Photon noise adheres to a Poisson distribution, leading to a higher likelihood of exceeding the expected value for small signals due to the distribution's positively skewed tail. Larger photon counts indicate higher density, resulting in lower temperatures from the hydrostatic integration.

The notable $\overline{\Delta T}$ in the stratosphere (Fig. 3.7a) can be attributed to increased uncertainty σ of ΔT resulting from channel switching (approximately at 32 km and 40 km) and the accompanying sudden reduction in photon counts.

The operation of ALIMA on an airborne platform introduces challenges in utilizing larger integration periods, such as $\Delta t = 4$ min (Fig. 3.7b). The large speed of HALO and

the larger temporal integration causes coarser horizontal resolutions. Even though the effect of photon noise is strongly reduced (smaller σ of ΔT at the top and at altitudes of channel transitions) $\overline{\Delta T}$ is present just more centered around zero instead of being dominantly a cold bias.

Flight maneuvers disturb the temporal integration of photon count profiles. The observational volume alters when the aircraft ascends or descends, which introduces varying uncertainties in photon count profiles. Furthermore, during turns, ascends or descends, the aircraft rotates around the roll (longitudinal) and/or pitch (lateral) axes. The aircraft's change in orientation causes the laser beam to deviate from the vertical axis. This leads to the sampling of a different observational volume. The altitude range of ALIMA might be limited during flight maneuvers which include an oblique laser beam as the path through the atmosphere is longer and the beam experiences larger attenuation.

The effects of flight maneuvers are not incorporated in the lidar simulations since flight segments including any flight maneuvers are excluded in the following analysis described in Chapter 5.

Note that below 25 km in Figure 3.7a, b, $\overline{\Delta T}$ and σ have a lower statistical significance. This is a result from a reduced number of photon count profiles, and consequently, temperature profiles, included in the statistical analysis. The reduction results in the truncation of profiles where the detected photon rate surpasses 5 MHz. The variations of photon rates at constant altitude in time are typically related to changes in different flight altitudes. For example, when the aircraft ascends, the distance to a target at a constant altitude above become smaller, the solid angle larger, and hence, the photon count rates increase. Conversely, when the aircraft descends, the photon count rates decrease.

Figure 3.8 shows the Root Mean Square Error (RMSE) of ΔT for different SNR used as threshold for determining the initalization altitude z_0 of the far channel. The aim to ensure that the signal is sufficiently strong can be approached by using a certain SNR threshold for determining the initialization altitude z_0. The RMSE exhibits only slight variation between different used SNR thresholds, remaining below 0.2 K. The most discernible outcome is that a higher SNR threshold for the far channel results in a lower starting altitude z_0 for the hydrostatic temperature integration and thereby yields shorter retrieved temperature profiles. The RMSE diminishes as the signal strength increases at lower altitudes. Consequently, adopting a larger SNR threshold provides no advantage if the objective is to reduce the temperature uncertainty arising from photon noise.

SNR thresholds between 1 and 3 are initially achieved at altitudes where approximately 10 photons per bin are registered. However, the SNR should not be small, as this would lead to an larger ΔT attributable to photon noise. Consequently, for ALIMA, a SNR of 4 is chosen for the far channel (a SNR of 8 is used for the mid and low channel).

When the temperature is retrieved from simulated photon counts without the inclusion of Poisson-distributed photon noise (dashed lines in Fig. 3.8), the RMSE is reduced by up to 3 K above 65 km, compared to the lidar simulation with photon noise included (solid lines in Fig. 3.8). Below 65 km, the RMSE remains relatively consistent between the two lidar simulations. This suggests that the uncertainty stemming from photon noise becomes clearly distinguishable from other effects causing a ΔT only above 65 km.

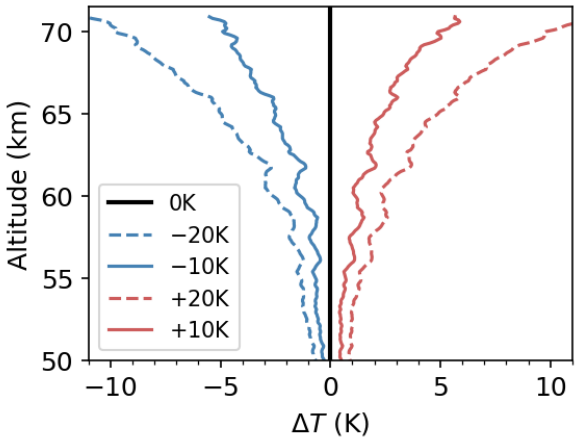

Figure 3.9.: Mean temperature deviation between retrieved temperatures from lidar simulations of ST08 with any initialization bias (black curve), with a ± 10 K bias and a ± 20 K bias. Based on simulation configuration **v1** and for a $\Delta t = 10$ min and an initialization altitude $z_0 = 78$ km.

3.3.4. Choice of the initial value for the temperature integration

The simulations, whose results are shown in Figure 3.7, did not include any bias in the initial value used for the initialization of the hydrostatic temperature retrieval with an averaged ERA5 temperature profile of the ST08 flight track.

However, for real atmospheric applications, the temperature used in the initialization of the hydrostatic integration $T(z_0)$ cannot be reliably determined, and deviations from the estimated a priori values are inevitable (except for rare occasions when independent measurements at the relevant altitudes and location are available).

Figure 3.9 illustrates how different choices of a-priori values for $T(z_0)$ impact the results. The hydrostatic integration of simulated photon count profiles is initialized with $T(z_0)$ values that differ by up to ± 20 K from the actual temperature at 78 km. This range encompasses plausible deviations, e.g. the largest variability in temperature at these altitudes is caused by GWs with amplitudes up to 50 K in the vicinity of the Southern Andes (Reichert et al., 2021). The discrepancy is halved at an altitude of 70 km, and only a fraction, one-tenth, of the initial deviation persists at 60 km (equivalent to 2.5 scale heights H). The downward integration ensures that the influence of any bias in the initial value diminishes rapidly as the air density increases. Below 50 km, any residual temperature bias resulting from inaccuracies in $T(z_0)$ is less than 1 K.

The total temperature bias and uncertainty is however not solely caused by instrumental effects (photon noise, channel transitions) and the initialization. Assumptions and simplifications made in the temperature retrieval may also result in deviations in the temperatures. Numerical effects such as errors related to the interpolation and smoothing of photon count and temperature profiles in the retrieval process may play a role as well. The potential impact of the assumption of hydrostatic equilibrium in the temperature

retrieval will be explored in the following Section 3.4.

3.4. Uncertainty in determined gravity wave parameters as a consequence of the hydrostatic assumption

The temperature retrievals used in the analysis of data produced by the majority of middle atmospheric Rayleigh lidar systems are based on the assumption of an atmosphere being in local hydrostatic equilibrium as presented in Sections 2.4.3 and 3.2.2 (Method based on Hauchecorne and Chanin, 1980). Examples od data sets for which this retrieval has been applied are data of the CORAL system in Tierra del Fuego, Argentina (e.g. Kaifler et al., 2020b; Kaifler and Kaifler, 2021; Reichert et al., 2021), the Balloon Lidar Experiment (BOLIDE) (e.g. Kaifler et al., 2020a), the Temperature Lidar for Middle Atmosphere research (TELMA) operated in New Zealand during the Deep Propagation (DEEPWAVE) campaign (Kaifler et al., 2015), the ALOMAR system in Norway (e.g. von Zahn et al., 2000; Baumgarten, 2010), the RMR lidar in Kühlungsborn, Germany (e.g. Gerding et al., 2016) and the RMR LTA at the Observatoire de Haute-Provence, France (e.g. Wing et al., 2018b; Wing et al., 2018a).

The hydrostatic assumption is the base of the hydrostatic integration and is the established method for the temperature retrieval of lidar observations. However, it is acknowledged that the hydrostatic assumption is violated under certain atmospheric conditions, e.g. for smaller mesoscale atmospheric processes. The temperature retrieval may result in deviations between the actual atmospheric temperature and the derived temperature based on the hydrostatic integration. These temperature errors resulting from the violation of the underlying assumption have not been systematically quantified to date and have been neglected due to a lack of better knowledge.

One approach for quantifying the effect of the hydrostatic assumption is through the comparison of results with a retrieval that does not presuppose the hydrostatic assumption, such as the Optimal Estimation Method (OEM). The PCL in Western Ontario is the only Rayleigh lidar system for which a temperature retrieval based on the OEM has been applied (e.g. Sica and Haefele, 2015; Jalali et al., 2018; Jalali et al., 2019). The OEM is constructed to overcome shortcomings of the hydrostatic temperature retrieval, namely the assumption of a hydrostatic balance. This approach uses forward models to fully characterize the measurement process, enabling the simultaneous retrieval of temperature, dead time, and background parameters. The OEM method yields a comprehensive uncertainty budget for each temperature profile, encompassing statistical uncertainties, smoothing errors, and various sources of uncertainty such as Rayleigh extinction, ozone absorption, and lidar constants.

However, the statistical nature of the OEM algorithm comes with certain limitations. The quality and accuracy of the retrieved temperature estimates heavily depend on the accuracy of the assumed a prior information. The OEM involves iterative calculations and matrix inversions, which can be computationally demanding. The relationship between

the measurements and the parameters is highly nonlinear, thus the OEM might struggle to converge. Furthermore, the OEM assumes that errors in measurements and models follow a Gaussian distribution. In real-world situations, this assumption might not hold true, leading to underestimation or overestimation of uncertainties in the retrieval.

The limitations complicate the quantification of any potential temperature error due to the hydrostatic assumption when comparing the two methods. The shortcomings of the hydrostatic temperature retrieval are of physical nature compared to the statistical shortcomings of the OEM. Thus it might be more intuitive to use the hydrostatic temperature retrieval and characterize its limitations on its own. This thesis employs a non-hydrostatic model to characterize the uncertainty in hydrostatically retrieved temperatures by incorporating the influence of the non-hydrostatic modes on the simulated temperatures.

In the scope of GW measurements, especially of MWs, non-hydrostatic wave responses can be present. Indeed, non-hydrostatic GWs are the preferred atmospheric mode for tropospheric winds which increase with altitude (Wurtele et al., 1987; Keller, 1994). Therefore, the following questions arises:

- Is an error introduced to the temperatures when using the hydrostatic temperature retrieval in presence of non-hydrostatic GWs or when the hydrostatic equilibrium is not given?
- If yes, does the error depend on the amplitude, altitude, or wavelength of the GWs?

These questions are approached in the following Sections 3.4.1-3.4.4 and constitute a detailed aspect of question **(1)**, which is summarized in Section 3.5.

3.4.1. Hydrostatic balance

The vertical momentum equation 2.1 gives the vertical acceleration of a fluid parcel:

$$\frac{\mathrm{d}w}{\mathrm{d}t} = -g - \frac{1}{\rho}\frac{\partial p}{\partial z}, \tag{3.6}$$

with the solution ($\overline{w} = 0 \Rightarrow w = w'$):

$$w' = \Re\Big\{\sum_k \tilde{w}_k e^{i(kx-\omega_k t)}\Big\} \quad \Rightarrow \quad w' = \Re\Big\{\sum_k w_k e^{ikx}\Big\} \quad \text{(for steady state)}. \tag{3.7}$$

If $\mathrm{d}w/\mathrm{d}t$ is small, the vertical components of the pressure gradient force $\vec{F}_P$ and gravity $\vec{F}_G$ balance each other, so that the fluid is in hydrostatic equilibrium:

$$\frac{\mathrm{d}p}{\mathrm{d}z} \approx -\rho g. \tag{3.8}$$

Vice versa, if $\mathrm{d}w/\mathrm{d}t$ is not small, the hydrostatic equilibrium is not valid. If it is assumed that $\mathrm{d}w/\mathrm{d}t$ is small a priori, without knowing the magnitude of $\mathrm{d}w/\mathrm{d}t$, that is called the *hydrostatic assumption* or *hydrostatic approximation*.

The hydrostasy is related to the curvature of fluid parcel streamlines, or simpler, how quickly $w(x)$ changes along the x-direction. For wave modes with large $\lambda_k(x) \Leftrightarrow$ small $k(x)$, the vertical acceleration will be slow and gradual (Eq. 3.7). Whereas, the vertical acceleration will be more important and stronger for wave modes with small $\lambda_k(x) \Leftrightarrow$ large $k(x)$ since the fluid parcel streamlines will oscillate more rapidly. Thus, the larger $k(x)$ gets, the more non-hydrostatic the flow will become.

The hydrostatic assumption is very powerful, as is simplifies the governing equations 2.1-2.3 by setting the vertical momentum equation to be Equation 3.8. The hydrostatic assumption corresponds to neglecting the k^2 term (non-hydrostatic term) of the Taylor-Goldstein equation 2.7. However, the assumption excludes the solution of non-hydrostatic modes and the downstream trapping of non-hydrostatic MWs (see Section 2.2).

Keller (1994) showed that hydrostatic and non-hydrostatic modes are possible under conditions that the classical theory from Queney (1948) (see Section 2.2) does not feature, e.g. hydrostatic mode for narrow mountains ($\approx$ 2.5 km) and non-hydrostatic mode for broad mountains ($\geq$ 16 km). Numerical model simulations of wave propagation showed that a vertical nonuniform wind and stability determines the wave modes instead of the orography (Wurtele et al., 1987), while the orography modulates the relative amplitudes (Ralph et al., 1997). Therefore, in presence of a nonuniform flow it cannot be assumed a priori that the hydrostatic assumption is valid as long as the mountain is broad (Keller, 1994).

3.4.2. Methods and data

EULAG

Idealized simulations for hydrostatic and non-hydrostatic wave responses are conducted with the EUlerian/semi- LAGrangian fluid solver (EULAG). EULAG is a nonlinear solver of the governing equations with 2^{nd} order accuracy (Smolarkiewicz and Margolin, 1997). Explicitly, EULAG solves the momentum conservation equation (2.1) for all three directional components, the energy conservation equation (2.2) for potential temperature perturbations and the mass conservation equation (2.3). Since EULAG solves the vertical momentum equation explicitly, it includes non-hydrostatic behavior. The environmental reference atmosphere is at rest, namely in hydrostatic balance and the gravitational acceleration g is set constant with altitude.

Simulation set-up and hydrostatic temperature integration

For this analysis, EULAG is used to generate MWs above a two-dimensional isolated mountain with a mountain height $h_0 = 628.3$ m and three different mountain half widths $a = [50, 10, 2]$ km. Following the classical theory by Queney (1948) (see section 2.2), these different a values generate, respectively, Hydrostatic Mountain (HSM), limiting case of hydrostatic and Non-Hydrostatic Mountain (NHSM) wave responses. The simulations are performed for a two-dimensional grid (x, z) with a total domain size in x-direction of 624 km (limiting case and hydrostatic case) and 100 km (non-hydrostatic case). The

horizontal resolution is 500 m (limiting case and hydrostatic case) and 200 m (non-hydrostatic case); the vertical resolution is 200 m for all cases. The output is saved at specific locations in the x-direction, specifically at $[-156, -78, 0, 78, 156]$ km relative to the mountain peak and in 15 min temporal resolution in order to resemble ground-based lidar data.

The simulations are started with atmospheric conditions as shown in Figure 3.10. The temperature profile $\overline{T_{EULAG}}$ decreases throughout the troposphere followed by a transition from constant temperature (between 10 km to 20 km), reproducing the tropopause, to the stratosphere with increasing temperature. The temperature gradient remains constant above, hence there is no stratopause and mesosphere. The temperature changes of the stratopause and mesosphere had to be omitted due to numerical stability of the simulations. The zonal background wind $\overline{u}$, which is the component perpendicular to the mountain, contains two local maxima, one tropospheric jet stream at about 10 km and one depicting the PNJ at about 55 km. Above, the wind decreases and reverses at 90 km, depicting a critical level for MWs. The meridional wind $\overline{v}$ is set to zero as the simulations are two-dimensional. Due to the vertically nonuniform zonal wind, the wave responses in the different cases may not resemble the strict separation of hydrostatic and non-hydrostatic GWs (Wurtele et al., 1987). A simulation with a constant wind profile was unsuccessful due to numerical instability.

The background profiles of $\overline{T_{EULAG}}$ and $\overline{u}$ remain constant in the course of the simulation. Thus, they remain uninfluenced by the developing GW induced perturbations. Furthermore, the background vertical velocity $\overline{w} = 0$, thus $\Rightarrow w = w'$.

The impact of the hydrostatic assumption on the hydrostatic temperature retrieval is determined by comparing the EULAG temperature T_{EULAG} with a hydrostatically calculated temperature $T_{HYDROSTATIC}$. First, $T_{HYDROSTATIC}$ is calculated from the EULAG density output via the hydrostatic integration (see section 2.4.3). Second, perturbation quantities T'_{EULAG} and $T'_{HYDROSTATIC}$ are derived following Equation 2.6. The impact is quantified as difference between both temperatures:

$$\Delta T' = T'_{HYDROSTATIC} - T'_{EULAG} \tag{3.9}$$

By testing various vertical resolutions, it is ensured that numerical effects first start to influence the integration for a vertical grid spacing of 1 km or larger. For smaller vertical resolution, numerical effects are negligible for the hydrostatic integration.

Furthermore, data which is influenced by nonlinear phenomena, e.g. wave breaking downstream the mountain or selective filtering at the critical level (at about 90 km), is excluded. For these data, the linearization and the polarization equations 2.11-2.13 are not valid anymore. Simulation results downstream the mountain are not taken into account as nonlinear phenomena dominate the simulated atmospheric structures. Following, the minima and maxima amplitudes of the GW perturbations are identified and analyzed. See Figures 3.11 and E.1, E.2 and E.3 in Appendix E for examples of vertical timeseries of T' and $\Delta T'$ of the HSM and NHSM simulations.

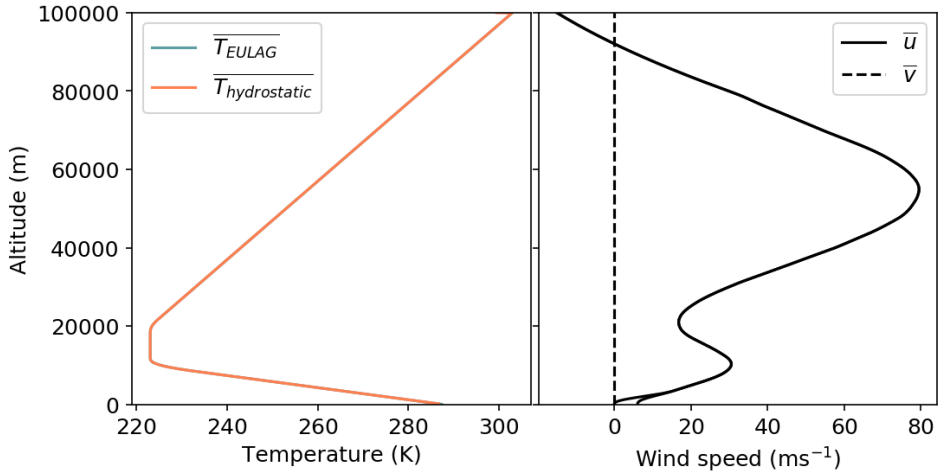

Figure 3.10.: Profiles of EULAG background temperature (turquoise line), hydrostatically integrated background temperature profile (orange line) and the zonal (solid line) and meridional (dashed line) wind profiles as used in the three simulations. Note that both temperature profiles follow each other closely and result in overlapping lines in the diagram, as well as, there is no stratopause and mesophere included in the temperature profile due to numerical stability of the simulations.

3.4.3. Results

Amplitude error $\Delta T'$

Initially, the hydrostatic temperature integration is validated by integrating the EULAG background density and the density within the first hours of the start of the simulation when MW perturbations are not yet developed. Figure 3.10 shows that the hydrostatically integrated profile $T_{HYDROSTATIC}$ equals the EULAG background temperature profile T_{EULAG} which is in hydrostatic balance. The hydrostatic integration performs equally well for the temperature prior to the development of GW induced perturbations.

This test proves, firstly, the ability of EULAG as non-hydrostatic model to reproduce hydrostatic conditions and, secondly, it proves the quality of the hydrostatic temperature integration.

The vertical timeseries of the NHSM simulation above the mountain is shown in Figure 3.11. After a spin up time of about 10 h of the model, MW induced temperature perturbations are present (Fig. 3.11a). Below 40 km, T'_{EULAG} is stationary. Above 50 km, the phase lines of T'_{EULAG} feature a tilt in time which flattens toward the end of the simulation time, indictaing that the simulation has reached a fully stationary state. Figure 3.11b and Figure 3.11c show that the temperature amplitudes of $T'_{HYDROSTATIC}$ are underestimated compared to T'_{EULAG}. This underestimation is largest between 50 km to 70 km where also λ_z is largest.

Figure 3.12 and Figure 3.13 show the impact of the hydrostatic assumption on the temperature determination for the NHSM regime and the HSM regime above the mountain,

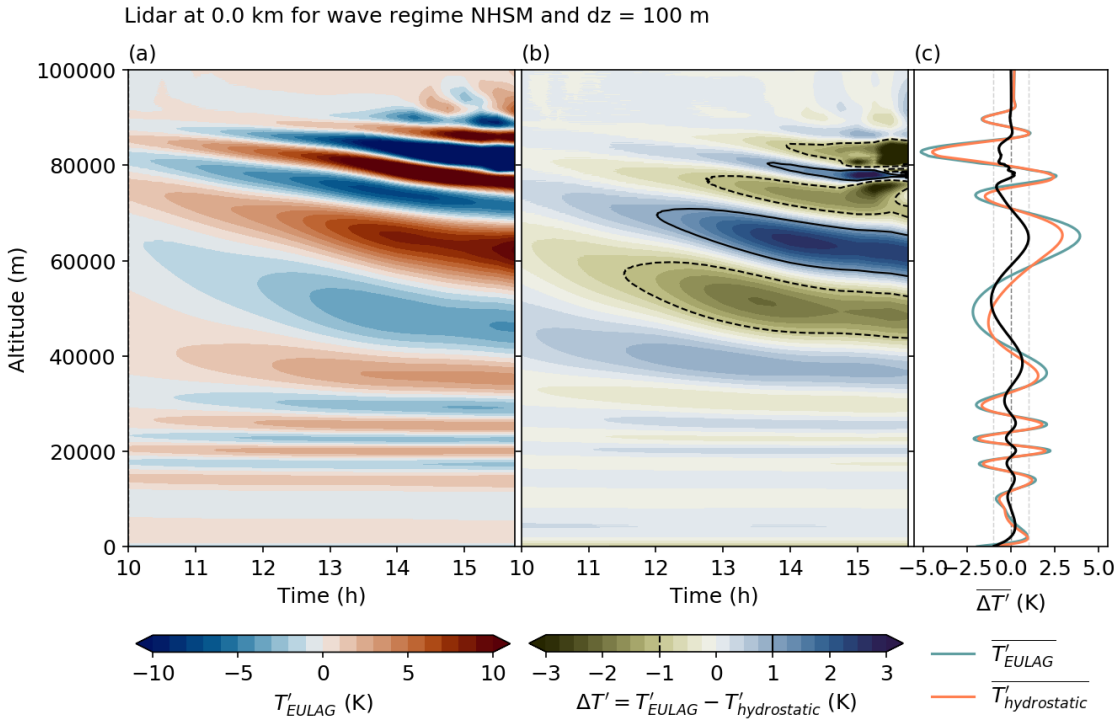

Figure 3.11.: Vertical timeseries of (a) T', (b) $\Delta T'$, and (c) the temporal average $\overline{\Delta T'}$ over the displayed 6 h simulation time from the NHSM simulation above the mountain. Note that small perturbations around 80 km after 15 h are caused by generated wave breaking of the model; this nonlinear behavior is excluded from the analysis. The first 10 h of simulation are not shown due to the spin up of the simulation.

respectively. Both show a temperature error $\Delta T'$ that is negative for positive temperature perturbations and positive for negative temperature perturbations (Fig. 3.12a, 3.13a). The temperature perturbations and $\Delta T'$ obey linear relationships that feature different slopes $\Delta T'$ per T'_{EULAG}. For the NHSM regime, two different states exist with slopes of -0.75 K per 10 K and -3 K per 10 K. For the HSM regime, the slopes of -0.75 K per 10 K and -1.5 K per 10 K exist. This slopes translate to underestimations of the retrieved temperatures of 5 % to 20 %. Especially for the HSM simulation, scattering in $\Delta T'$ is apparent for large temperature perturbations. Potentially, the temperature data is not well enough filtered and perturbations caused by nonlinear phenomena are not entirely excluded. The outliers / scattering from the linear relationship will be disregarded. In a nutshell, the application of the hydrostatic temperature integration results in a underestimation of MW induced temperature perturbations compared to the reference temperature T'_{EULAG}.

Furthermore, $\Delta T'$ intensifies with altitude, being largest around 40 km to 70 km for the NHSM regime (Fig. 3.12b) and around 60 km to 80 km for the HSM regime (Fig. 3.13b).

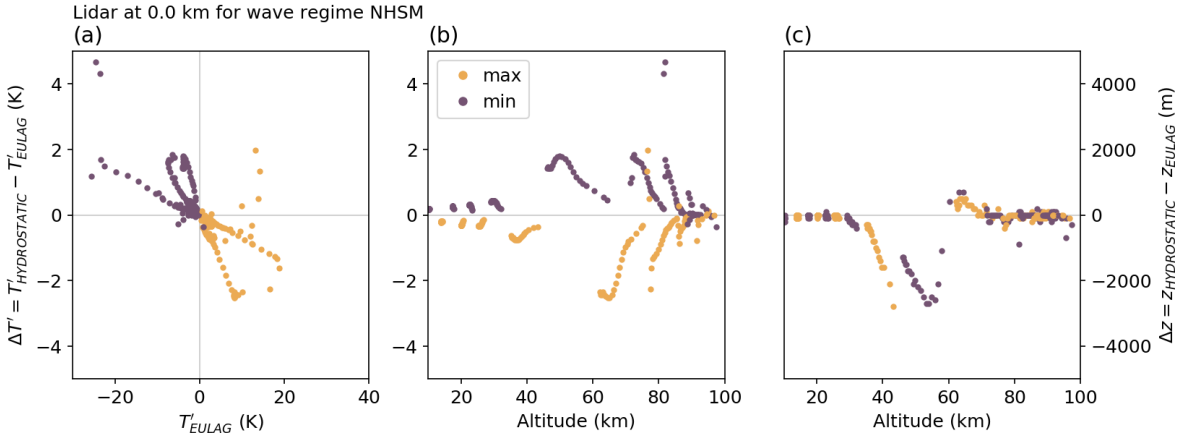

Figure 3.12.: Temperature errors (a, b) and altitude error (c) due to the hydrostatic assumption for the NHSM regime above the mountain. Yellow dots are for maximal amplitudes, purple dots for minimal amplitudes.

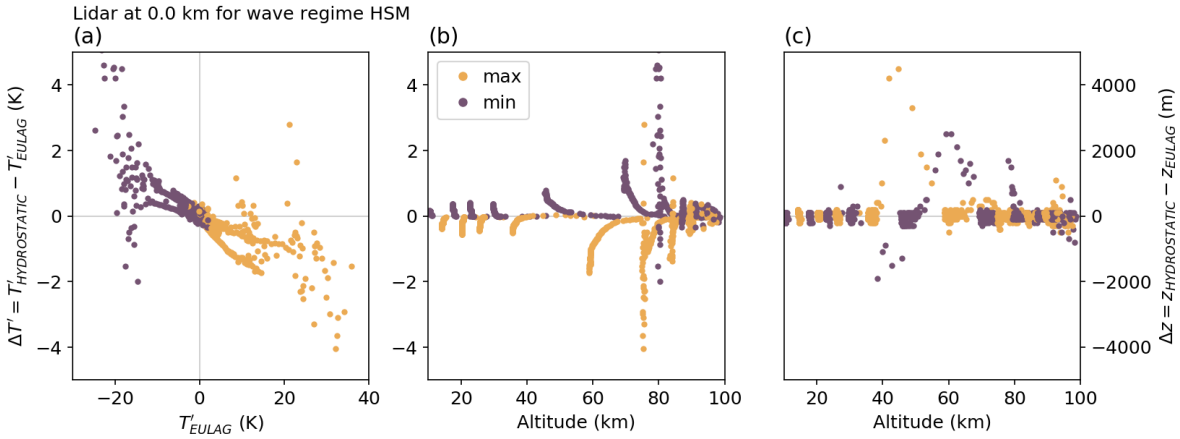

Figure 3.13.: Similar as Fig. 3.12 but for HSM regime above mountain.

Additionally, between 40 km to 60 km the hydrostatic temperature integration results in maxima in temperatures that are shifted in altitude by $\Delta z \approx -3$ km for the NHSM case (Fig. 3.12c) and $\Delta z \approx 2$ km to 4 km for the HSM case (Fig. 3.13c) compared to the reference. This behavior is especially pronounced for the NHSM case, since all amplitudes in the altitude range feature the behavior, whereas in the HSM case, only a fraction of the amplitudes feature the Δz.

Figure 3.14 shows for the NHSM regime the one-dimensional wavelet spectra $W_z(\lambda_z)$ of T'_{EULAG} and $T'_{HYDROSTATIC}$ using a Morlet wavelet and a nondimensional frequency $\omega_0 = 4$ (more information on the wavelet method can be found in Appendix F), as well as the temperature profiles used for the wavelet analysis. The time step corresponding to an elapsed time of 14 h is chosen to reflect steady-state condition, that is, MWs remain stationary in the $t - z$ plane. For both temperature perturbation profiles, λ_z is largest in the altitude range between 40 km to 60 km, coinciding with the altitude

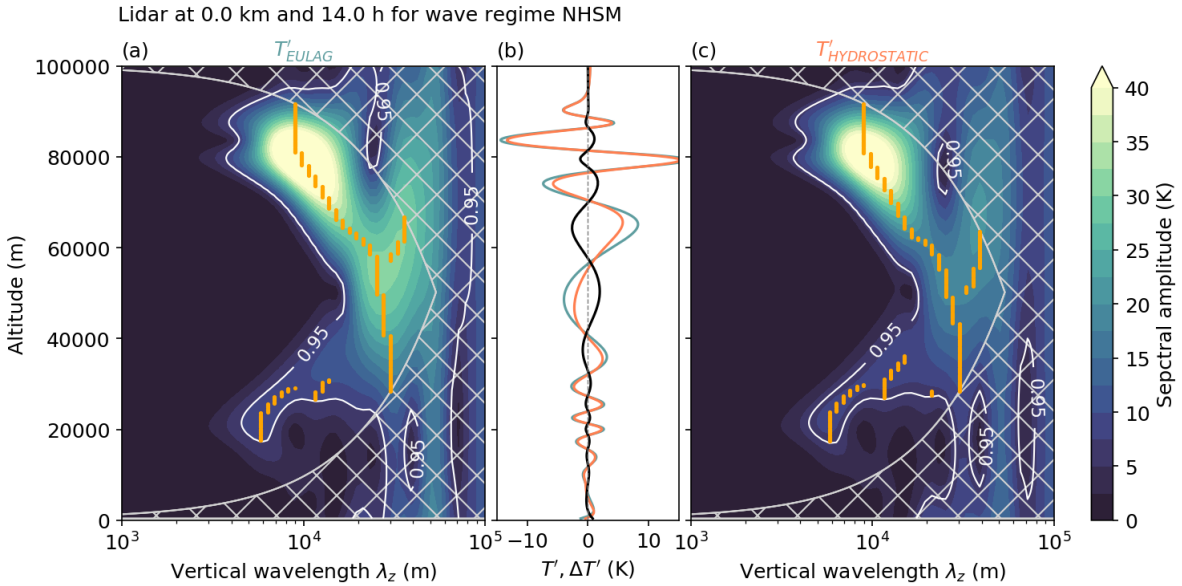

Figure 3.14.: 1D wavelet spectra of NHSM regime at 14 h simulation time as function of vertical wavelength and altitude for (a) T'_{EULAG} and (c) $T'_{HYDROSTATIC}$. Hatched area indicates the cone of influence, orange line the local maxima in spectral amplitude and white line give the 95 % confidence interval. (b) shows the respective temperature profiles T' for the derivation of the wavelet spectra (turquoise and orange line) and their difference $\Delta T'$ (black line).

range where the error Δz peaks and the maximum of the PNJ is located. The spectral amplitudes of the larger λ_z (> 20 km) are generally reduced in the wavelet spectrum of the hydrostatically integrated temperature. On the one hand, smaller temperature perturbations due to the underestimation by the hydrostatic temperature integration cause smaller spectral amplitudes, on the other hand, changes in the vertical wavelength might limit the agreement of wavelet amplitudes and temperature perturbations. Between 40 km to 60 km, λ_z of the hydrostatically integrated temperature is ≈ 2 km to 3 km larger and features a larger secondary maxima of local spectral amplitude. The change in λ_z matches the observed $\Delta z \approx -3$ km, since the deviating position of the amplitudes in altitude by the hydrostatic integration increases the local λ_z.

Figure 3.15 and Figure 3.16 show again the impact of the hydrostatic assumption on the determined temperatures for the NHSM regime and the HSM regime but now for a location upstream of the mountain. No significant $\Delta T'$ or Δz are evident for the NHSM regime. However, temperature perturbations are quite small upstream, -2.5 K $< T' < 5$ K, and the impact of the hydrostatic assumption might just not be detectable. For the HSM regime temperature perturbations are rather large upstream, ± 15 K, and still no significant $\Delta T'$ and Δz are observed.

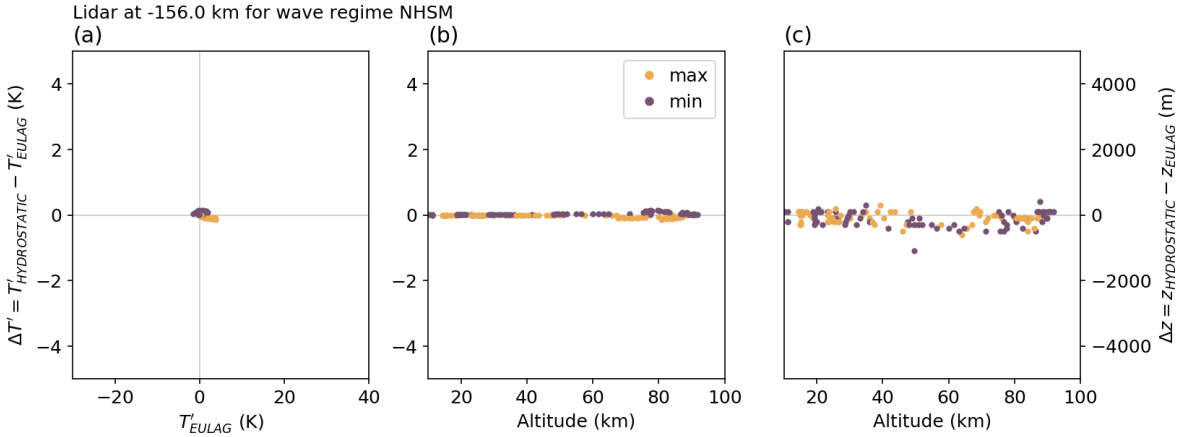

Figure 3.15.: Similar as Fig. 3.12 but for NHSM regime upstream mountain.

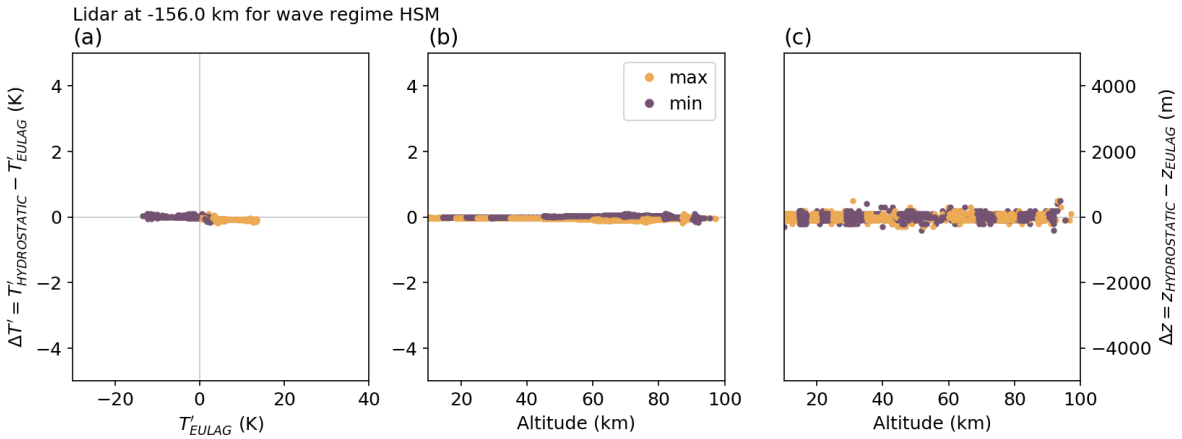

Figure 3.16.: Similar as Fig. 3.12 but for HSM regime upstream mountain.

Influence of the vertical velocity

The relation between the temperature perturbations and the vertical wind for the NHSM regime and the HSM regime above the mountain is displayed in Figure 3.17 and Figure 3.18, respectively. The relation between T'_{EULAG} and w and between $\Delta T'$ and w is shown for the peak amplitudes as well as for all other data points. The polarization equation for (potential) temperature 2.13 shows that temperature perturbations and vertical velocity obey a 90° phase shift ($i \Rightarrow \pi/2$). Due to the selection of the corresponding peak amplitudes in T'_{EULAG} and w, the phase shift is removed and temperature perturbations and vertical velocity feature linear relationships. For all other data points (grey dots), the phase shift is present and the $w - T'$ relationship generates circular paths, where generally w peaks at T' being zero and vice versa. For both simulations, peak values of w and T' relate linearly with positive (negative) w for positive (negative) T' (Fig. 3.17a, 3.18a) and due to the linearity between temperature perturbation and temperature error, $\Delta T'$ is positive (negative) with negative (positive) w peaks (Fig. 3.17b, 3.18b). The

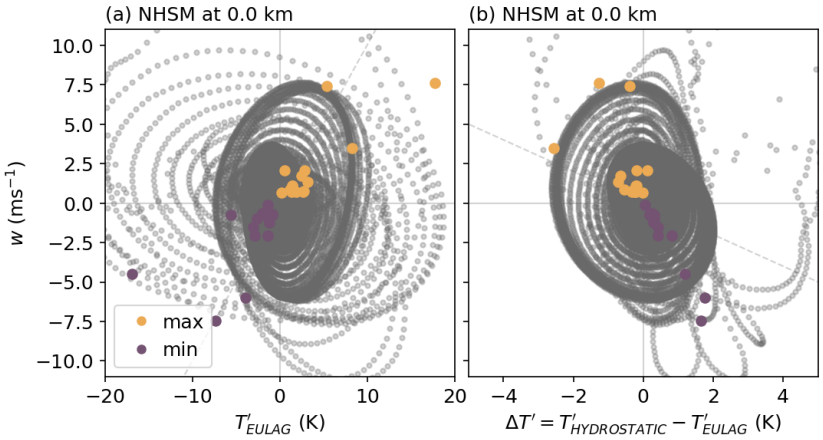

Figure 3.17.: Relation between the vertical wind and (a) the temperature perturbation, as well as, (b) temperature error $\Delta T'$ for the nonhydrostatic mountain regime above mountain. Yellow dots are for maximal amplitudes, purple dots for minimal amplitudes.

$w - T'$ relationships feature slopes of 6 ms^{-1} per 10 K (NHSM and HSM) and 1.5 ms^{-1} per 10 K (HSM). Differences in the $w - T'$ relationship are also visible for all other data points. Other than the theoretical circular path of $w - T'$, the relationship depicts oblate (elongated in T'-direction) and prolate (elongated in w-direction) paths. Oblate paths predominate for the HSM regime while oblate and prolate paths exist for the NHSM regime. Generally, it can be inferred that the more prolate a path is the more important and less negligible the vertical velocity becomes and, hence, the larger the resulting temperature underestimation due to the hydrostatic assumption.

Figure 3.19 and Figure 3.20 show the $w - T'$ relationship and the $w - \Delta T'$ relationship for the NHSM case and HSM regime upstream the mountain. The relations are much weaker upstream of the mountain than above the mountain. For the NHSM regime, temperature perturbations and thus $\Delta T'$ are quite small. Similarly, w is quite small with $w \approx \pm$ 1 ms^{-1}. Values of w are larger for the HSM regime, up to $\pm$ 2 ms^{-1}, and feature a linear relationship with the temperature perturbations with a slope of 1.5 ms^{-1} per 10 K. The circular paths of all other data points are strongly oblate, highlighting the gradual vertical motion connected to the rather large temperature perturbations. As mentioned before, no significant $\Delta T'$ is evident upstream of the mountain and therefore no correlation between $\Delta T'$ and w is evident.

The previous results show that the relation between the vertical motion and the temperature perturbations changes between locations upstream and above the mountain. Following the polarization equation 2.13, this can be possible if either the background temperature profile $d\overline{\theta}/dz$ changes in x-direction or the intrinsic frequency Ω changes in x-direction. Since the background temperature profile is constant for the whole simulation domain, the intrinsic frequencies of the excited GWs have to alter. Figure (3.21) and Figure (3.22) display profiles of intrinsic frequency upstream and above the mountain for the NHSM regime and the HSM regime, respectively. The calculation of Ω is based on

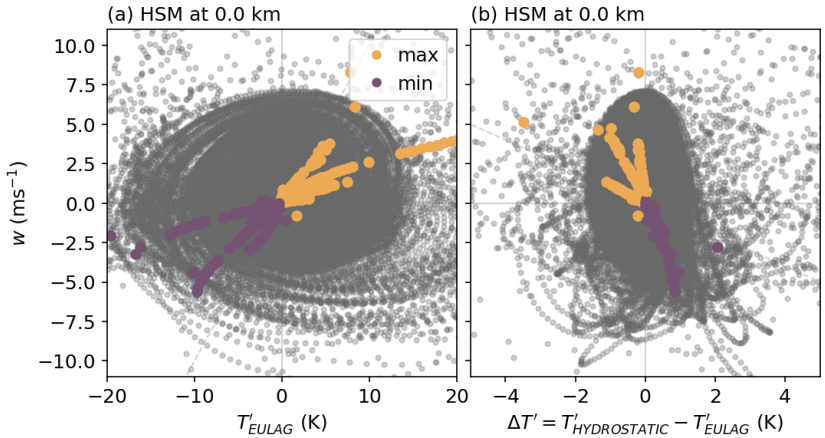

Figure 3.18.: Similar as Fig. 3.17 but for the HSM regime above the mountain.

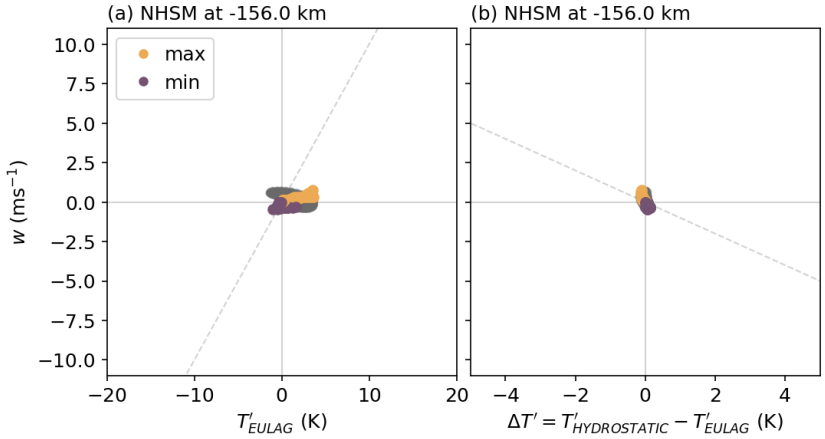

Figure 3.19.: Similar as Fig. 3.17 but for a location upstream the mountain.

the polarization equation 2.13. Additionally, the Brunt-Vaisala frequency N is shown (black line), which is constant in time and x-direction due to the constant background temperature profile. N varies between 0.01 s^{-1} in the troposphere and 0.02 s^{-1} in the stratosphere in z-direction. Generally, Ω is smaller than N, resulting in conditions enabling GW propagation over all altitudes. For the NHSM regime, the majority of Ω values is larger above the mountain ($0.002 - 0.018$ s^{-1}) than upstream of the mountain ($0.001 - 0.010$ s^{-1}). Fluid parcels oscillate faster in order to relate the stronger vertical velocity above the mountain to the temperature perturbation. Ω in the HSM regime behaves similar and is larger above the mountain ($0.001 - 0.020$ s^{-1}) than upstream of the mountain ($0.001 - 0.015$ s^{-1}), while part of Ω stays nearly similar, especially above 60 km.

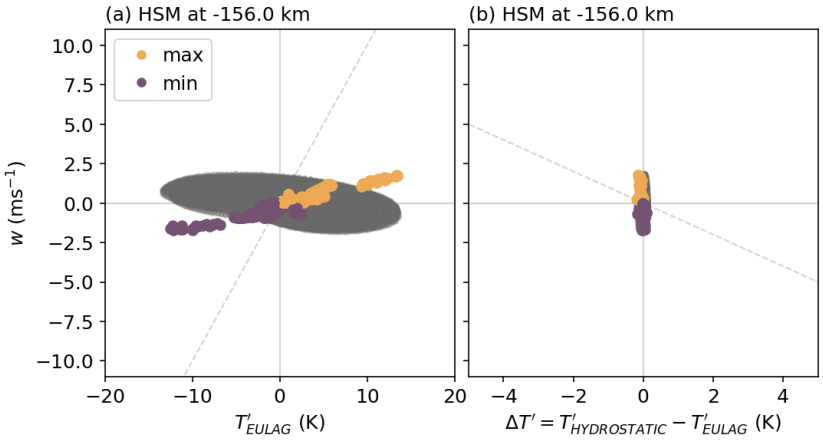

Figure 3.20.: Similar as Fig. 3.17 but for the HSM regime at a location upstream the mountain.

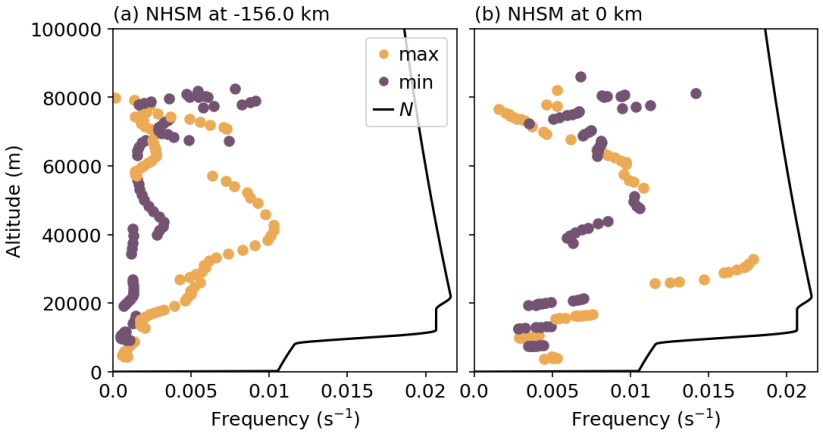

Figure 3.21.: Profiles of intrinsic frequency of the peak values of the NHSM regime at a location (a) upstream, and (b) above the mountain.

Gravity wave scales

The horizontal and vertical wavelengths are related to each other via equation (2.14) for stationary MWs. From the estimated λ_z using the one-dimensional wavelet transform, λ_x can be calculated. Table 3.3 and Table 3.4 summarize the Scorer parameter, wavelength and wavenumber estimates for the NHSM regime and HSM regime above the mountain, respectively. l and l^2 are identical for both simulations since both simulation have the same constant background conditions. λ_z is estimated from the time step of 14 h, which reflects steady-state condition, that is, MWs remain stationary in the $t - z$ plane. In this simulation setting, λ_z decreases with altitude from 29 km at 40 km to 10 km at 80 km for the NHSM regime and from 23 km at 40 km to 9 km for the HSM regime. λ_z is thus slightly smaller for the HSM regime. Derived λ_x are thus slightly larger for the HSM regime compared to the NHSM regime, with largest λ_x of 8,242 km and 8,105

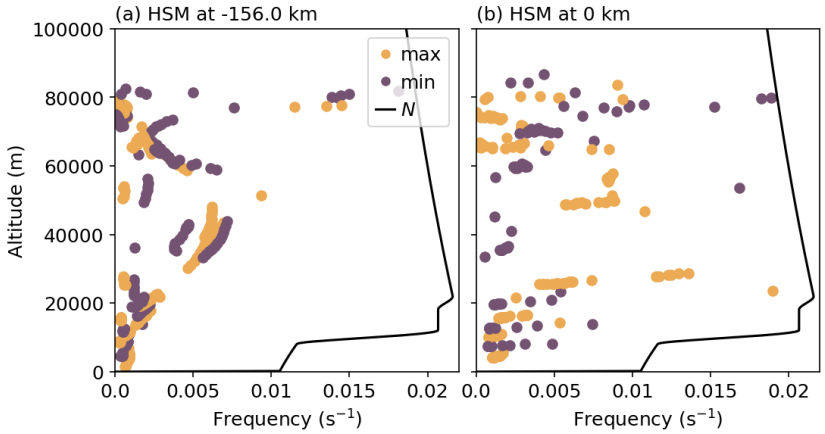

Figure 3.22.: Similar as Fig. 3.21 but for the HSM regime.

km, respectively. Generally, for all altitudes and regimes it follows that $l^2 > k^2$, excited GWs are able to propagate vertically. Since $l^2 >> k^2$ is not fulfilled for any of the two simulation regimes and rather $l^2 \approx k^2$, excited GWs are of non-hydrostatic nature for both, the NHSM and HSM regime. The calculated λ_x also matches the range of horizontal scales of non-hydrostatic GWs as shown in Figure 2.2.

Table 3.3.: Steady-state wave scales of NHSM simulation above mountain

z(km)	l, l^2	λ_z(m)	m(m^{-1})	k, k^2(m^{-1})	λ_x(m)	
80	0.00109, $1.19 * 10^{-6}$	10000	0.00063	0.00095, $8.01 * 10^{-7}$	7021	$\Rightarrow l^2 > k^2$
60	0.00083, $6.90 * 10^{-7}$	21000	0.00030	0.00078, $6.00 * 10^{-7}$	8105	$\Rightarrow l^2 > k^2$
40	0.00094, $8.87 * 10^{-7}$	29000	0.00022	0.00092, $8.40 * 10^{-7}$	6854	$\Rightarrow l^2 > k^2$

Table 3.4.: Steady-state wave scales of HSM simulation above mountain

z(km)	l, l^2	λ_z(m)	m(m^{-1})	k, k^2(m^{-1})	λ_x(m)	
80	0.00109, $1.19 * 10^{-6}$	9000	0.00064	0.00084, $7.08 * 10^{-7}$	7466	$\Rightarrow l^2 > k^2$
60	0.00083, $6.90 * 10^{-7}$	19000	0.00033	0.00078, $5.81 * 10^{-7}$	8242	$\Rightarrow l^2 > k^2$
40	0.00094, $8.87 * 10^{-7}$	23000	0.00027	0.00090, $8.13 * 10^{-7}$	6970	$\Rightarrow l^2 > k^2$

3.4.4. Discussion and conclusions

Occurrence of non-hydrostatic MW modes

The results presented in Section 3.4.3 are derived from idealized two-dimensional simulations of a limited domain with the assumption that the seperation of orographic wave regimes is determined by the width of the mountain (Queney, 1948). Thus, the simulations represent only certain types of waves, e.g. inertia-GWs are not captured. The given set-up of the simulations does not allow any statement at which horizontal scale GWs become soley hydrostatic.

The simulation results show that the background temperature is captured well by the hydrostatic integration. MW induced temperature perturbations are also reproduced by the hydrostatic integration upstream of the mountain but are underestimated above the mountain. This underestimation thus depends on the location relative to the mountain and increases with increasing altitude, increasing amplitude and increasing vertical wavelength of the MW.

One reason for the increasing deviation with altitude is the increase of the temperature perturbation amplitude due to the decrease of density with altitude. Another reason is the vertical wind structure and the resulting structure of the vertical wavelength, namely increasing wind velocities with altitude increase the vertical wavelength (as shown in Equations 2.14 and 2.17). The latter might play an important role, as $\Delta T'$ decreases above 65 km for the NHSM regime even though temperature amplitudes still increase above (Fig. 3.14b). The decrease in $\Delta T'$ agrees well with the decreasing of the vertical wavelength with altitude above 65 km.

It is very interesting that the hydrostatic temperature integration leads to similar underestimations for both non-hydrostatic and hydrostatic simulations above the mountain. Most likely, non-hydrostatic wave responses are excited and propagated in both simulations due to the presence of the vertical wind shear related to the background wind profile.

The results indicate that the classification of MWs as hydrostatic response or non-hydrostatic response is not solely determined by the underlying orography (Wurtele et al., 1987; Keller, 1994). The analysis of wave scales ($l^2 > k^2$) confirms that non-hydrostatic wave responses are excited in both simulations. The simulation results emphasize that in the presence of vertical wind shear, the separation of hydrostatic and non-hydrostatic effects is challenging and often invalid. The classical theory of wave regime separation through orography is based on constant wind (Queney, 1948). Therefore, in reality one has to assume that non-hydrostatic modes are always excited if the wind profile varies with altitude. Whether the non-hydrostatic modes are strong enough to dominate an observed field has to be determined for each observation.

The small temperature perturbations upstream the mountain justify the assumption of a hydrostatic equilibrium. Vertical wind velocities of 2.5 ms^{-1} are about one order of magnitude smaller than the horizontal wind velocity and are thus considered to be small enough for the validity of Equation 3.8. However, above the mountain non-hydrostatic modes are present in both cases. This leads to the conclusion that the vertical wind is

not negligible above the mountain and that the hydrostatic balance is not valid. Using a hydrostatic temperature retrieval in this case results in an underestimation of retrieved temperature perturbations.

Resulting uncertainty in the hydrostatic temperature retrieval

A further question arises from the results: Why are the retrieved temperatures underestimated in presence of non-hydrostatic modes? This can be answered by considering the polarizations equations 2.11-2.13. If the vertical wind velocity increases, also the other wave quantities, perturbations in horizontal wind velocity, pressure, and temperature, have to increase. On the one hand, a larger vertical velocity implies that also $\mathrm{d}w/\mathrm{d}t$ is larger and a vertically displaced fluid parcel oscillates faster. On the other hand, the vertical displacement of this fluid parcel needs to be larger, too, which can be inferred from the larger temperature or pressure perturbations.

If a fluid parcel is vertically displaced upwards, $\mathrm{d}w/\mathrm{d}t$ decreases from zero at its level of hydrostatic balance to $\mathrm{d}w/\mathrm{d}t < 0$ at its maximum upwards displacement. When the fluid parcel moves again downwards to its level of hydrostatic balance, the acceleration increases again to $\mathrm{d}w/\mathrm{d}t = 0$. During the whole upwards displacement, the acceleration is negative which means that $\vec{F}_P < \vec{F}_G$, which follows from Equation 3.6:

$$\underbrace{\frac{\mathrm{d}w}{\mathrm{d}t} \cdot \rho}_{<0} + \frac{\partial p}{\partial z} = -g \cdot \rho \Rightarrow \frac{\partial p}{\partial z} < -g \cdot \rho. \tag{3.10}$$

The stronger the acceleration due to larger vertical velocities during the upward oscillation, the greater will be the difference between the acting forces in order to restore the larger vertical displacements, e.g. $\vec{F}_P << \vec{F}_G$ for $\mathrm{d}w/\mathrm{d}t << 0$. Vice versa, for a downwards displaced fluid parcel, $\mathrm{d}w/\mathrm{d}t$ and $\vec{F}_P > \vec{F}_G$.

Qualitatively, the application of the hydrostatic assumption in the hydrostatic temperature retrieval neglects the inertia force of the vertical motion. Quantitatively, the application of the hydrostatic assumption in the hydrostatic temperature retrieval causes a underestimation of the retrieved temperature perturbation by 5 % to 20 %, if non-hydrostatic wave modes are present. The bias depends on the amplitude, altitude and wavelength of the present GWs.

Furthermore, the occurrence of the temperature perturbation underestimation depends on the location. In the simulation, only hydrostatic modes are present upstream of the mountain while above the mountain non-hydrostatic modes dominate. The general conclusion about a temperature bias in retrieved temperatures from ALIMA observations due to the hydrostatic assumption is difficult to capture due to the simplified approach used in this analysis and due to the different identified dependencies of amplitude, altitude and wavelength of the present GWs.

Still the results can be of relevance. Reichert et al. (2021) showed that for the Southern Andes common MW events feature temperature amplitudes of 25 K to 55 K and vertical wavelength between 10 km to 20 km in the middle atmosphere during austral wintertime.

Due to present vertical wind shear, non-hydrostatic modes are excited. If those are able to propagate into the middle atmosphere, temperature perturbations are potentially underestimated by 5 % to 20 % due to hydrostatic retrieval. Hence, actual temperature perturbations for common Southern Andes MW events may be as large as 30 K to 66 K.

Generally, non-hydrostatic MWs have short horizontal wavelengths, e.g. $\lambda_k \leq 20$ km (Fig. 2.2), and are limited to the troposphere (Fritts and Alexander, 2003). The question if non-hydrostatic wave modes are at all present in ALIMA observations, is investigated in Chapter 5.

3.5. Summary

ALIMA was first operated during the SouthTRAC-GW campaign 2019. This Chapter presented a detailed error budget of uncertainties and biases in photon count profiles of ALIMA and corresponding retrieved temperature profiles. The analysis included the investigation obtained with ALIMA photon counts, lidar simulations based on ERA5 data and lidar simulations based on EULAG simulations. The findings concerning the error budget of ALIMA are summarized in Table 3.5. Repeating question **(1)** raised in Chapter 1:

(1) How accurate and precise are the densities and temperatures derived from ALIMA observations?

Various factors impact the quality of the observations by ALIMA and retrieved temperatures: photon noise, photon background, atmospheric transmission as Rayleigh extinction and absorption by ozone, the temperature retrieval including the hydrostatic assumption, the initialization, numerical effects and smoothing effects. These factors should be considered when interpreting lidar-based temperature measurements and assessing their uncertainties. The Chapter emphasized that real-world conditions, such as flight maneuvers and variations in ozone concentration, can further impact the retrieved temperatures.

Generally, it can be concluded that 1 % difference in photon counts translates to a ΔT of 0.5-0.65 K. An altitude-dependent bias of $\pm$ 1 K and an altitude-dependent uncertainty of 1-6 K for Δt = 1 min (Fig. 3.7a) persist using the temperature retrieval with all corrections as described in Section 3.2. These values can be translated for the accuracy and precision of the retrieved density. The density includes an altitude-dependent bias of $\pm$ 0.4 % and altitude-dependent uncertainty of $\pm$ 0.7-2 %.

This chapter further analyzed the impact of the presence of non-hydrostatic GW modes on the retrieved temperature perturbations using simulated lidar measurements. The Chapter investigated the validity of the hydrostatic assumption used in temperature retrieval of ALIMA by using a non-hydrostatic model to explore how the temperature retrieval might be affected by the presence of non-hydrostatic GWs.

Using the hydrostatic temperature retrieval in cases where non-hydrostatic GWs are present introduces errors in temperature estimates. The Chapter demonstrated that the

application of the hydrostatic assumption underestimates temperature perturbations caused by non-hydrostatic GWs. This is because the hydrostatic assumption does not account for the presence of vertical wind shear and non-hydrostatic wave responseIn the presence of vertical wind shear, even in cases where the underlying orography suggests a hydrostatic response, non-hydrostatic modes can be excited causing an potential underestimation of retrieved temperature perturbations.

Furthermore, the bias introduced by the hydrostatic assumption depends on the amplitude, altitude, and wavelength of the GWs. The bias is larger for larger temperature perturbations, and it intensifies with altitude. Additionally, the bias is related to the vertical wind velocity; larger wind velocities lead to larger biases. The relationship between the bias and these factors is not linear, and there can be variations and complexities in the error behavior.

Table 3.5.: Contributions of different error sources to ALIMA observations and the retrieved temperatures.

Source	ΔP_R	$\overline{\Delta T}$	$\max \Delta T$	Correction possible	Remarks
Photon background	$<$ 1-2 %	–	$<$ 1 K	Yes	at initialization altitude
Photon noise	$<$ 20-30 %	1-2.5 K	25 K	No	Cold bias at initialization altitude; altitude-dependent; for small integration periods
Rayleigh extinction	2.5-3.5 %	1.5 K	2 K	Yes	Cold bias below 25 km; altitude-dependent
Absorption by ozone	2.4-4.7 %	2 K	2.5 K	Yes	Cold bias peak at 20-25 km; altitude-dependent
Initialization	–	0-20 K	$>$ 20 K	No	Any ΔT becomes negligible approx. 15 km below the initialization altitude
Hydrostatic integration	–	0 %	5-20 %	No	Depends on the presence of non-orographic GWs and their structure
Bias	–	$\pm$ 1 K	–	No	Altitude-dependent

4. Large-scale and gravity wave dynamics during the SOUTHTRAC-GW campaign

The Andes are the most prominent mountain range in the SH and influence the weather and circulation throughout all altitudes of the atmosphere, from the synoptic scale down to the mesoscale. The part of the Andes south of 40°S, the Southern Andes, reaches to mean heights of 1500 m a.s.l., with peaks above 3000 m a.s.l. and a typical mountain width of 200 km. The Southern Andes act as a perpendicular barrier to the on average westerly low-level flow, resulting in opposite climate zones over the western and eastern slopes (Garreaud, 2009). Following the Köppen-Geiger climate classification (Peel et al., 2007), the western slope (South Chile: Aysén and Magallanes y de la Antártica Chilena; Tierra del Fuego) is characteristed by oceanic subpolar climate, temperate oceanic climate and tundra climate, while the eastern slope (South Argentina: Patagonia and Tierra del Fuego) features cold semi-arid climate and a cold desert climate.

The dominant year-around tropospheric westerly flow over the Southern Andes contains eastward propagating anticyclones, cyclones and associated frontal systems. These transient eddies are part of the SH extratropical storm track trailing the Polar Front Jet (PFJ) (e.g. Trenberth, 1991; Nakamura and Shimpo, 2004; Garreaud et al., 2008). The PFJ is located south of 40°S during austral winter and the transition seasons and can be clearly separated from the Subtropical Jet (STJ) located north of 40°S while a single PFJ is present during austral summer south of 40°S (Gallego et al., 2005). The pressure systems of the storm track induce a large day-to-day variability to the tropospheric flow impinging on the mountain range of the Southern Andes. The flow can interact with the Southern Andes in different ways depending on the daily synoptical flow, e.g. split and flow around, being blocked or flow over. These flow regimes can lead to e.g. low-level jets along the western side of the mountain range (Garreaud, 2009), isentropic draw-down of upper-level flow causing potential downslope windstorms, called Zonda, (Temme et al., 2020) or lifting which can induce orographic precipitation (Smith and Evans, 2007) and the excitation of MWs.

The Southern Andes are the world's strongest hotspot of MWs (e.g. Rapp et al., 2021). The nearly perpendicular orientation of the mountain range to the strong westerly flow of the PFJ within the troposphere, as well as, the position of the mountain range close or even centered to the maximum of the PFJ, are the crucial factors for the large MW activity.

Also stationary Rossby waves are generated by the Southern Andes. The downstream

wave train results from the westerly flow over the prolonged ridge of the Southern Andes as a result of potential vorticity conservation (e.g. Holton and Hakim, 2013). Vertical stretching (compressing) causes a cyclonic (anticyclonic) rotation and poleward (equatorward) motion upstream (above the mountain) while the north-south motion is accompanied by an increase (decrease) of the Coriolis force f.

The interaction between the SH storm track and the Southern Andes results in a complex interplay of atmospheric processes. The mountains not only enhance precipitation on their windward side but also have broader implications for regional and global weather and climate patterns. By influencing the movement of moisture and storm systems, the Southern Andes contribute to the intricate overall picture of dynamical variability in the SH.

This Chapter aims to characterize the large-scale dynamics in the troposphere and stratosphere and the GW dynamics in the middle atmosphere during the SouthTRAC-GW campaign in September 2019. In doing that, question **(2)** will be elaborated:

- What was the dynamical condition during SouthTRAC-GW and how did it impact the observed GWs?

In particular, further detailed aspects of the questions are explored, namely:

- What were the conditions for the excitation of MWs at the Southern Andes during the period of the SouthTRAC-GW campaign and did the excitation in 2019 differ from other years due to the SSW?
- How was the GW activity distributed around the Stratospheric Polar Vortex (SPV) during the SSW?

4.1. Methods and Data

For the characterization of the dynamical situation, ERA5 data are analyzed by the determination of the Mountain Wave Activity (MWA) in the troposphere for certain upstream areas and the calculation of the gravity wave potential energy density E_p. For the first part in Sections 4.2.2 and 4.3, 6-hourly resolved ERA5 data on pressure levels from 1000 hPa to 1 hPa and at the 2PVU (Potential Vorticity Unit) level are used.

The upstream flow conditions are characterized in order to determine the potential MWA in days per month by evaluating the following three criteria (Dörnbrack et al., 2001):

$$U_{H,up}(p = 850hPa) > U_*, \tag{C1}$$

$$\alpha_{SA} - \Delta\alpha_* < \alpha_{H,up}(p = 850hPa) < \alpha_{SA} + \Delta\alpha_*, \tag{C2}$$

$$\partial\alpha(p) = \alpha_{H,up}(p) - \alpha_{H,up}(p = 850hPa) < \Delta\alpha_*, \tag{C3}$$

with $U_{H,up}$ as average horizontal wind velocity of one of the upstream boxes [UP1, UP2, UP3.1, UP3.2] (Fig. 4.1), $U_* = 10$ ms^{-1} as horizontal wind velocity threshold. α_{SA} describes the wind direction of the flow upstream which is perpendicular to the Southern

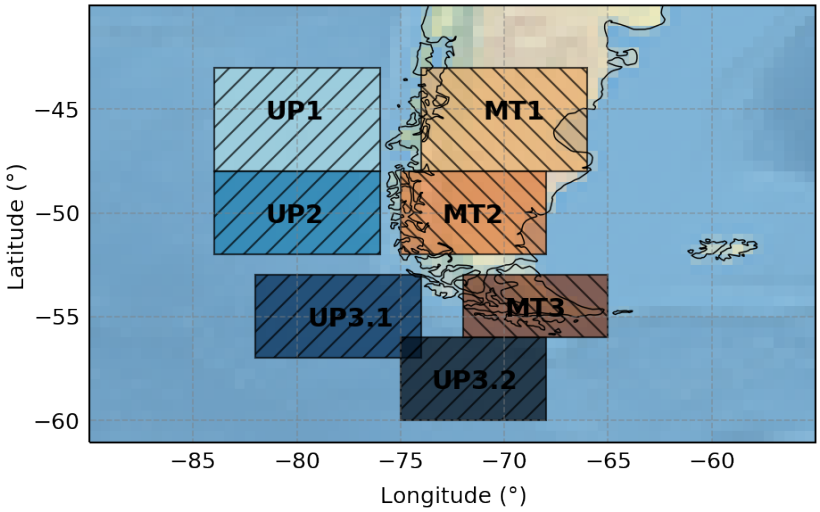

Figure 4.1.: Overview of the used upstream boxes and the boxes above the the Southern Andes. ERA5 data within each box are averaged to one representative value for ach time step and vertical level.

Andes mountain range and is set to $\alpha_{SA} = 270°$ for UP1 and UP2, to $\alpha_{SA} = 260°$ for UP3.1, and to $\alpha_{SA} = 210°$ for UP3.2. $\alpha_{H,up}$ is the average upstream wind direction of the four boxes and $\Delta\alpha_* = 45°$ is the threshold difference between the wind direction and the direction perpendicular to the mountain range. $\partial\alpha(p)$ describes the vertical change of the wind direction with respect to the 850 hPa level and is calculated from 500 hPa up to 50 hPa.

The three criteria C1, C2 and C3 are evaluated for each time step whether true or false. Subsequently, the MWA arises as true if all three criteria are true. Criteria C1 and C2 depict the potential of excitation of MWs by ensuring a tropospheric flow which is strong enough and impinges on the mountain range in an appropriate angle. Criteria C3 describes basically the potential for the vertical propagation of excited MWs, namely that the vertical change of horizontal wind direction is small enough that no critical level for the MWs arises.

In order to evaluate whether the dynamical conditions during September 2019 were anomalous, the ERA5 data during the SouthTRAC-GW campaign 2019 is compared to a daily climatology calculated from daily values between 1979 to 2019 (the variability of each day within this 40 years period), as well as, to the year 2006. During 2006, the SPV was strong (Byrne and Shepherd, 2018) and resulted in good excitation and propagation conditions of MWs.

For the second part presented in Section 4.4, hourly resolved ERA5 data on model levels are used. The vertical levels are transformed to altitude and interpolated to a vertical grid with $\Delta z = 100$ m resolution to resemble the ALIMA data and allow a direct comparison. Furthermore, the ERA5 data are interpolated in time and horizontal space with a bilinear interpolation to $\Delta t = 10$ s and to the flight tracks of the six research flights ST08, ST09, ST10, ST11, ST12, and ST14.

A PNJ detection is performed for the ERA5 data in all four dimensions (t, z, lat, lon) alias (time, altitude, latitude, longitude). On the basis of Manney et al. (2011) and Manney et al. (2014), the following conditions/method are chosen for the determination of the PNJ:

- $U_H \geq 30$ ms^{-1}.
- The detection is performed in the region from 35°S to 65°S and from 82°W to 46°W (the area covering all six flights).
- The detection is performed for each altitude in latitudinal and longitudinal direction and the resulted detections are combined afterwards (due to the displacement of the SPV from the South Pole and its deformation, the PNJ deviates from a mostly zonal flow and features a dominate meridional component).
- If more than one wind maximum is detected, they have to be separated by at least 15° in latitude to count as individual jet streams. Due to the limited regional extent, typically only one wind maximum prevails; a second wind maximum can be present due to the displacement of the SPV.

The determination of the PNJ position allows for the classification whether a ALIMA observations was taken poleward or equatorward, and – by classifying the edge of the SPV as wind maximum of the PNJ – whether a ALIMA observations was taken inside or outside of the SPV.

Furthermore, the gravity wave potential energy density E_p is calculated as proxy for GW activity from ALIMA observations and ERA5 data:

$$E_p = \frac{1}{2}\frac{g^2}{N^2}\overline{\left(\frac{T'}{\overline{T}}\right)^2}. \tag{4.1}$$

The temperature perturbation T' is determined by subtracting a 30 min running mean $\overline{T}$. The relative temperature perturbation term is furthermore averaged over 30 min denoted by the large overline.

4.2. Dynamical overview of the 2019 SH SSW and the SouthTRAC–GW research flights

4.2.1. The 2019 Sudden Stratospheric Warming

A persistent midlatitude circumpolar Rossby wave train of zonal Wavenumber 1 (WN1), sustained through anomalous convection over the subtropical Pacific Ocean and eastern South Pacific, governed the 2019 SH SSW (Shen et al., 2020b). The exceptional and prolonged upward propagation of zonal WN1 Rossby waves from the troposphere originated equally from inputs of instantaneous anomalous WN1 and the constructive interference with the climatological WN1 pattern. Furthermore, the descending easterly phase of the

stratospheric QBO facilitated beneficial conditions for the SSW. The easterly phase of the QBO prohibits the propagation of Rossby waves towards the equatorial stratosphere which instead decelerated the SH PNJ (Gray et al., 2005).

The 2019 SH SSW started on 30 August and peaked on the 17 September with an overall warming of polar cap temperatures at 10 hPa of 66 K (Eswaraiah et al., 2020). The most pronounced temperature increase of 50.8 K occurred from 5 to 11 September as obtained from MERRA-2 reanalysis data (Yamazaki et al., 2020). The zonal mean zonal wind at 10 hPa and 60°S decreased by 72 ms^{-1}. A wind reversal was detected at 60 km and 70 km close to 62°S; more southward, at 72°S, a reversal of the zonal flow was also observed in the stratosphere at 32 km (Eswaraiah et al., 2020). During this period the SPV was displaced from the South Pole toward the tip of South America.

The 2019 SSW was the second ever observed SSW in the SH. Due to the missing wind reversal at 10 hPa and 60°S, the 2019 event was only classified as minor SSW event even though comparable in magnitude to the first major SSW which occurred in 2002. As the 2019 event happened earlier in the year than in 2002, a still stronger SPV had to be decelerated in 2019 (Shen et al., 2020b; Lim et al., 2021). SH SSWs are rare and potentially will become rarer due to the predicted strengthening of the SPV caused by the changing climate system (Jucker et al., 2021).

Rao et al. (2020) demonstrated that the predictability of the 2019 SSW was considerably large with a lead time of around 18 days for sub-seasonal to seasonal models. The first signatures of the 2019 SSW were already predicted in July as shown by Lim et al. (2021).

A SSW is a complex phenomenon with various consequences for the atmosphere, from the troposphere up to the thermosphere and ionosphere.

The SSW led to changes in the convective activity in the tropics and to an acceleration of the Hadley cell circulation, primarily due to the changes of the thermal structure in the Upper Troposphere Lower Stratosphere (UTLS) (Noguchi et al., 2020).

The SSW caused a reduction in the formation of PSCs and an enhancement of stratospheric O_3 by 29 % during September 2019 (Safieddine et al., 2020), which lead to the smallest ozone hole on records (Hu, 2020; Shen et al., 2020a). The increased O_3 concentrations linked to the SSW provoked localized heating and stability changes of the lower atmosphere which induced a positive phase of the Southern Annular Mode (SAM) during austral spring (Jucker and Goyal, 2022), while from end of October the negative phase of the SAM subsided into the troposphere (Shen et al., 2020b; Lim et al., 2021). The SAM is the main mode of variability in the SH and describes the north-south movement of the westerly winds surrounding Antarctica; the SAM index reflects the strength and position of these westerly winds. (e.g. Thompson and Wallace, 2000; Fogt and Marshall, 2020). During the positive phase of the SAM, the following characteristics are typically observed: the poleward shift of the tropospheric PFJ and accompanied poleward shift of the storm track, as well as, a generally stronger zonal flow.

A strong wave activity of quasi 6-day waves was observed in the middle atmosphere and MLT caused by the SSW (Lee et al., 2021; Yamazaki et al., 2020). The quasi 6-day waves, in turn, favored large ionospheric anomalies at low-latitudes observed during September 2019 (Yamazaki et al., 2020; Goncharenko et al., 2020). Furthermore, there is observational evidence that the quasi 6-day waves interacted with 12-hourly tides in

the MLT (Liu et al., 2021) and an amplification of 12-hourly and 24-hourly tides (Liu et al., 2022) as response to the impact of the SSW on the middle atmosphere and MLT region. Mitra et al. (2023) suggested that the seasonal changes in tidal amplitudes can be explained by varying tidal sources, such as water vapor, convective activity, and ozone. However, the short-term variability in global tidal modes, after removing seasonal trends, shows a significant response connected to the 2019 SH SSW.

The weakening of the PNJ and the warming of the SPV during the SSW event caused a critical level for MWs (Rapp et al., 2021). The critical level descended from about 60 km at the beginning of September 2019 to 40 km at the end September 2019 and decreased the MW activity in the upper stratosphere (Rapp et al., 2021; Kogure et al., 2021) and mesosphere (Kohma et al., 2021). The increased selective filtering of GWs in the stratosphere caused anomalously low temperatures in the mesosphere during the SSW. The cooler mesosphere resulted in SH PMCs occurring much earlier in the season than expected (Yang et al., 2022).

The SPV broke down end of October (30 October 2019) at the 10 hPa level due to the SSW while the stratospheric signal of the SSW propagated downward into the troposphere beginning with the third week of October (Lim et al., 2020).

4.2.2. SouthTRAC–GW

SouthTRAC-GW was conducted in the southern part of South America and above the Antarctic peninsula in September 2019 to gather a unique dataset comprising temperature and trace gas observations from the troposphere up to the mesosphere (Rapp et al., 2021). The intention was to study MWs near their orographic sources, their vertical and horizontal propagation, and their breaking and dissipation. SouthTRAC-GW delivered measurements for the comparison and validation of other measurement techniques, high-resolutions simulations, and NWP models.

The first phase of the campaign lasted from September 9, 2019 to October 9, 2019 including the transfer flights from the DLR in Oberpfaffenhofen, Germany to the operational base in Rio Grande, Argentina. The dataset used in this thesis includes measurements from six dedicated MW research flights of the first phase: ST08 on 11/12, ST09 on 13/14, ST10 on 16/17, ST11 on 18/19, ST12 on 20/21, and ST14 on 25/26 September 2019 (see Table 3 in Rapp et al. (2021)) of HALO. Typical travelled distances are around 7000 km, within the region from 35°S to 65°S and from 82°W to 46°W, typical cruising altitudes between 10 km to 14 km, and typical aircraft ground speeds between 200 ms^{-1} to 300 ms^{-1}. A second phase of the SouthTRAC campaign was conducted from November 2, 2019, to November 27, 2019 with the objectives of coupling processes and the impact of the Antarctic SPV on the UTLS.

The key instruments utilized during the SouthTRAC-GW campaign included ALIMA (see Chap. 3), the Gimballed Limb Observer for Radiance Imaging of the Atmosphere (GLORIA) and the Basic HALO Measurement and Sensor System (BAHAMAS). These instruments were pivotal in capturing data related to GWs above, below and at flight altitude of HALO.

The GLORIA instrument is a specialized limb sounder designed to capture high-resolution radiance measurements of the atmosphere mounted in the belly pod of the HALO aircraft (Friedl-Vallon et al., 2014; Riese et al., 2014). As a Fourier transform spectrometer, GLORIA measures infrared radiance in a spectral range from 780 to 1400 cm^{-1}. The instrument utilizes a Michelson interferometer with a two-dimensional infrared detector array containing 256 x 256 elements, of which 48 x 128 pixels are utilized for simultaneous limb views.

GLORIA's observational capabilities cover altitudes from approximately 5 km to slightly above flight altitude. The instrument looks to the right side of HALO with a field of view that can be panned from 135° to 45° with respect to carrier heading in the horizontal plane. The observed radiance is integrated along the line-of-sight, providing valuable data on atmospheric constituents based on the type, amount, and temperature of molecules. GLORIA operates in two modes: chemistry mode with high spectral sampling and dynamics mode with coarser spectral sampling. GLORIA captures infrared radiation emitted by particles and trace species in the atmosphere, providing over 6,000 simultaneous limb views with elevation angles from -3.3° to slightly upwards, covering an altitude range of 4 km to around 15 km.

GLORIA employs two measurement modes suitable for GWs: full angle tomography (FAT) and limited angle tomography (LAT). FAT allows for the reconstruction of atmospheric temperature structure with a spatial resolution of 20 km horizontally and 200 m vertically, achieving high precision at 0.5 K accuracy. LAT, on the other hand, offers a resolution of 30 km in flight direction, 70 km across flight track, and 400 m vertically at an accuracy of 0.7 K. Full angle tomography is suitable for small-scale GWs with unknown orientation, while limited angle tomography is optimal for non-stationary waves.

BAHAMAS provides high-resolution (up to 100 Hz) situ measurements of horizontal and vertical winds, temperatures and pressures at flight level of HALO by means of a nose boom probe with a 5-hole wind sensor (Giez et al., 2017).

The flight planning for the SouthTRAC-GW campaign involved a careful forecasting process, including European Center for Medium-range Weather Forecast (ECMWF) Integrated Forecasting System (IFS) predictions and the Met Office Unified Model for higher resolution forecasts. The objective of flight planning was to perform flight patterns that intersect atmospheric waves at perpendicular angles to optimize observations. Visibility for GLORIA observations was another key factor considered in the planning phase. The success of the campaign depended on strategic coordination, aligning research objectives with instrument capabilities, and adapting to the atmospheric conditions encountered during the flights.

The campaign period coincided with the SH SSW (Dörnbrack et al., 2020; Lim et al., 2021). The SSW started at the end of August, therefore, all flights were conducted during the SSW.

The tropospheric flow was dominated by blocking ridges upstream of the Southern Andes causing a synoptic flow rather parallel to the mountain ridge in the first week of September 2019 (see Fig. 4 in Rapp et al., 2021). From 8 September 2019 a mostly zonal flow or propagating troughs dominated the tropospheric flow. Because the flights were

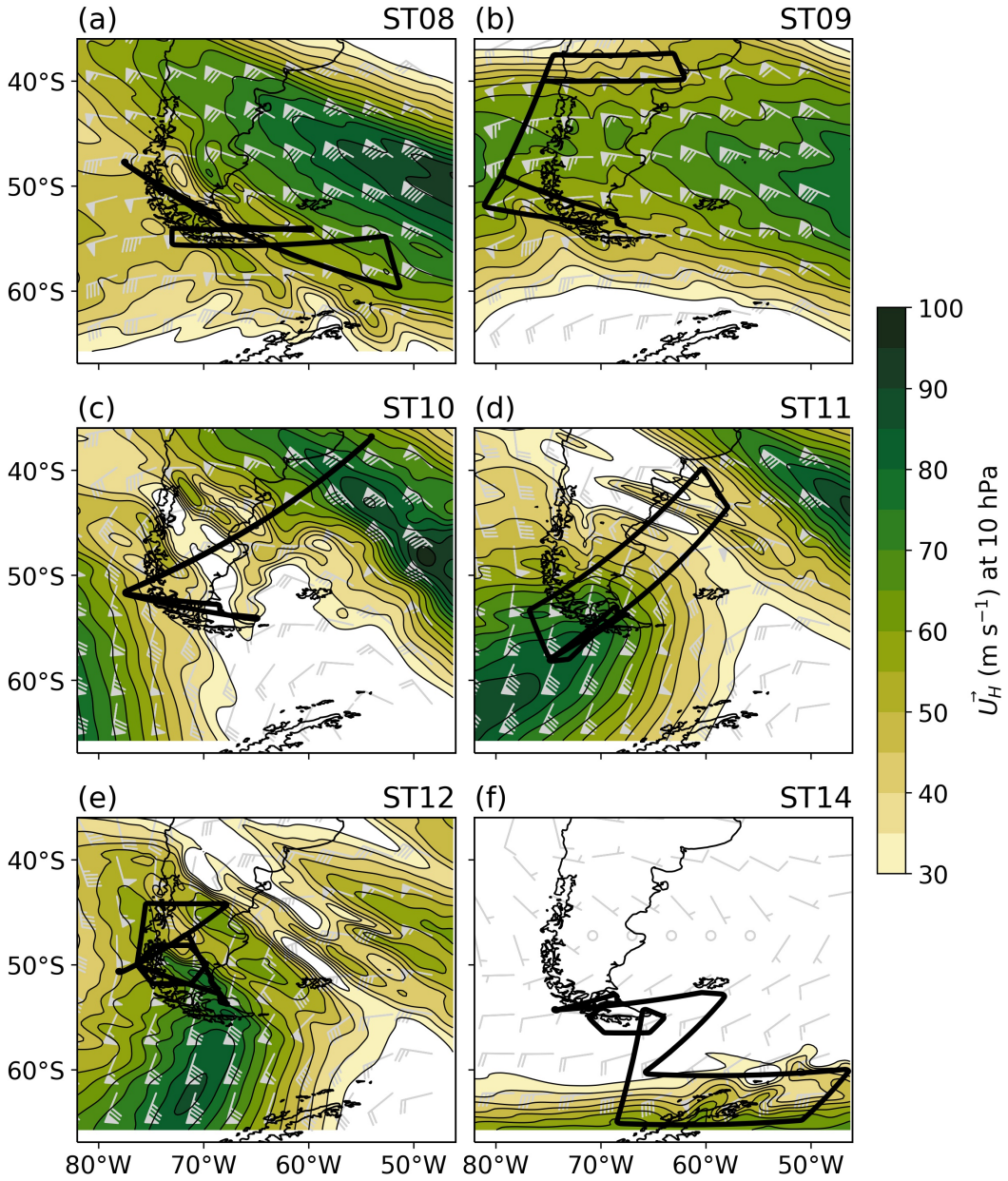

Figure 4.2.: Flight tracks, horizontal winds (shaded) and wind barbs at 10 hPa at 00 UTC of the respective day of research flights (a) ST08 (11/12 September), (b) ST09 (13/14 September), (c) ST10 (16/17 September), (d) ST11 (18/19 September), (e) ST12 (20/21 September) and (f) ST14 (25/26 September).

planned to be temporally aligned with a zonal upstream flow in the troposphere (Bauer et al., 2022), all flight days have in common that there were good excitation conditions of GWs at the Southern Andes and/or Antarctic Peninsula.

Figure 4.2 summarizes the six individual flight tracks and the prevailing horizontal winds at 10 hPa. At 10 hPa, the PNJ was shifted towards the tip of South America

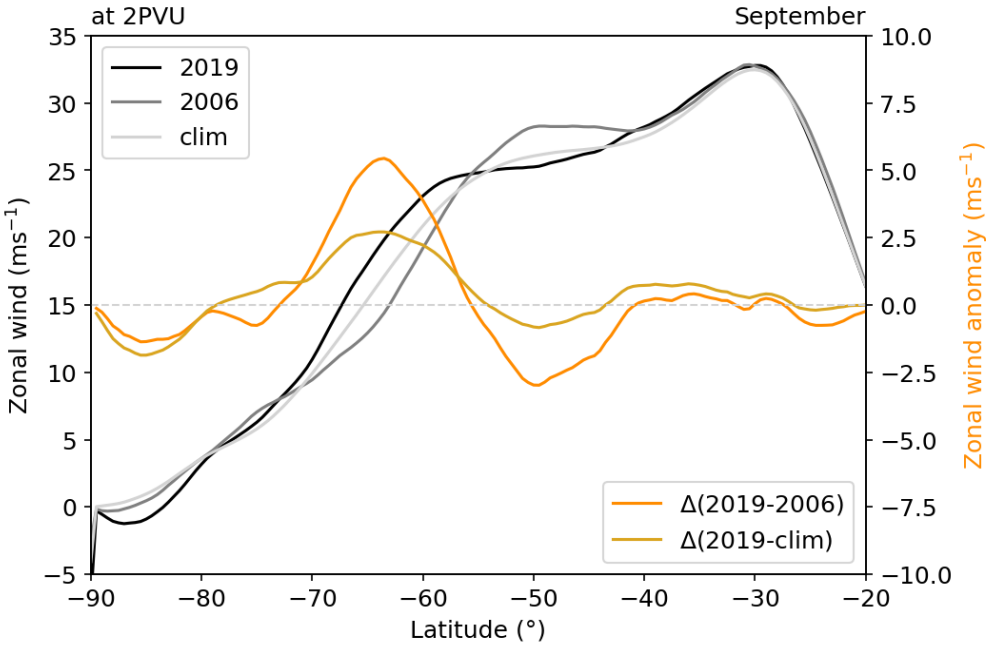

Figure 4.3.: Monthly mean zonal mean zonal wind for 2019, 2006 and the climatology, as well as, the difference in zonal mean zonal wind between 2019 and 2006 or the climatology at the 2 PVU surface for September.

with mostly zonal flow during ST08 and ST09. A deformation of the SPV (more elliptic) induced a strong curvature with strong meridional flow of the PNJ over the Southern Andes at 10 hPa during ST10, ST11, and ST12.

The vertical propagation of observed MWs was affected by the SSW during flights ST09, ST10, ST11, ST12 and ST14, whereas during the first flight ST08 observed MWs were able to propagate up to 60 km.

4.3. The tropospheric jet streams and the mountain wave activity

Figure 4.3 shows the monthly mean zonal mean zonal wind at the 2 PVU level for September. The 2 PVU level illustrates the altitude of the tropopause and intersects with the STJ and the PFJ close to their wind maxima. The STJ constitutes the wind maximum and is well centered at approximately 30°S with similar magnitudes of 32 ms^{-1} in 2019, 2006 and the daily climatology. The secondary wind maximum is the PFJ which is situated at approximately 50°S in 2006 and the daily climatology. The PFJ is slightly weaker in the daily climatology than 2006. During September 2019, the latitude of the wind maximum of the PFJ is shifted by 10° poleward to 60°S in the zonal mean perspective. The largest differences in the zonal mean zonal wind between 2019, 2006 and the daily climatology are apparent at about 65°S.

The zonal mean perspective clearly shows that the PFJ was shifted poleward during September 2019, from its typical location at 50°S streaming above the Southern Andes to 60°S to 65°S streaming above the Southern Ocean and the Drake's passage.

Figures 4.4 and 4.5 represent monthly mean daily anomalies between 2019 and 2006 at 2 PVU and 850 hPa, respectively.

The poleward shift of the PFJ highlighted in the zonal mean zonal wind of Figure 4.3 reinforces as positive anomaly in the zonal wind nearly circumpolar at 60°S to 65°S at the 2 PVU level (Fig. 4.4a) with the strongest accelerations above the Southeast Pacific and South Atlantic. The zonal component of the STJ strongly decelerates upstream of the Southern Andes. Accompanied is a strong increase of the meridional component (far) upstream of the Southern Andes with a poleward flow further to the west above the Pacific and a flow equatorward further to the east and closer to the Southern Andes (Fig. 4.4b). This horizontal flow pattern constitutes an anti-cyclonic rotation and ridge pattern upstream of the Southern Andes including positive geopotential height anomalies at 2 PVU (Fig. 4.4c).

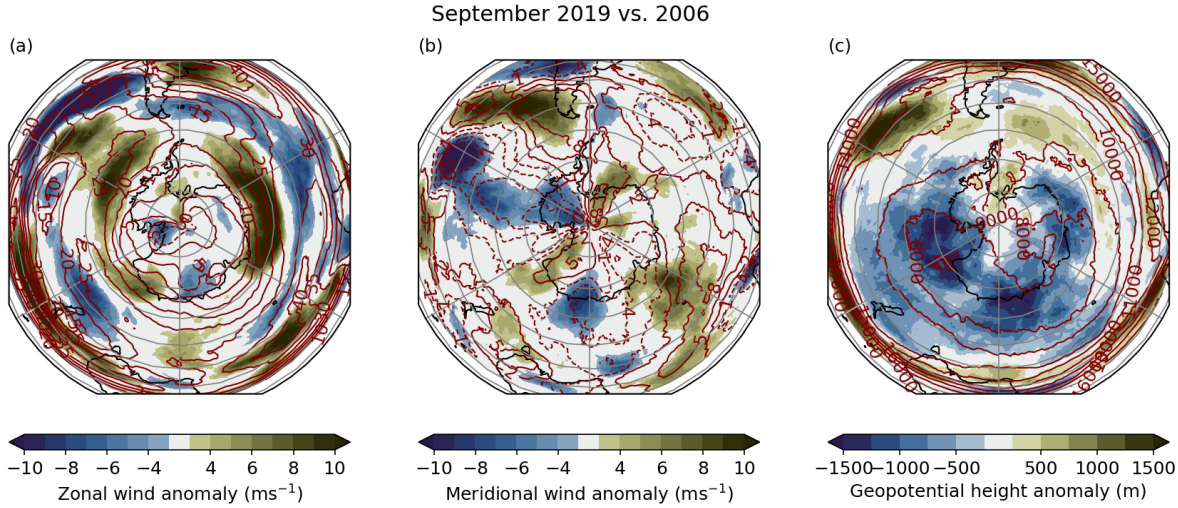

Figure 4.4.: Monthly mean daily anomalies (shaded) and monthly means (red contours) of (a) zonal wind, (b) meridional wind, and (c) geopotential height at the 2 PVU level. Monthly mean anomalies are derived as daily difference between 2019 and 2006.

The ridge is even more prominent within the troposphere at 850 hPa (Fig. 4.5c). A strong positive geopotential height anomaly persists above the Drake's passage with a closed ridge structure upstream the Southern Andes and the axis of the ridge extending toward the Antarctic Peninsula. Subsequently, the tropospheric zonal flow exhibits a strong deceleration upstream of the Southern Andes and is generally weaker all-round the Southern Ocean at 50°S to 60°S (Fig. 4.5a). Upstream the Southern Andes the tropospheric flow is deflected around the ridge structure with strong poleward and equatorward meridional flow, while the equatorward flow is directly upstream of the mountain range and forms a large-scale parallel flow (Fig. 4.5b).

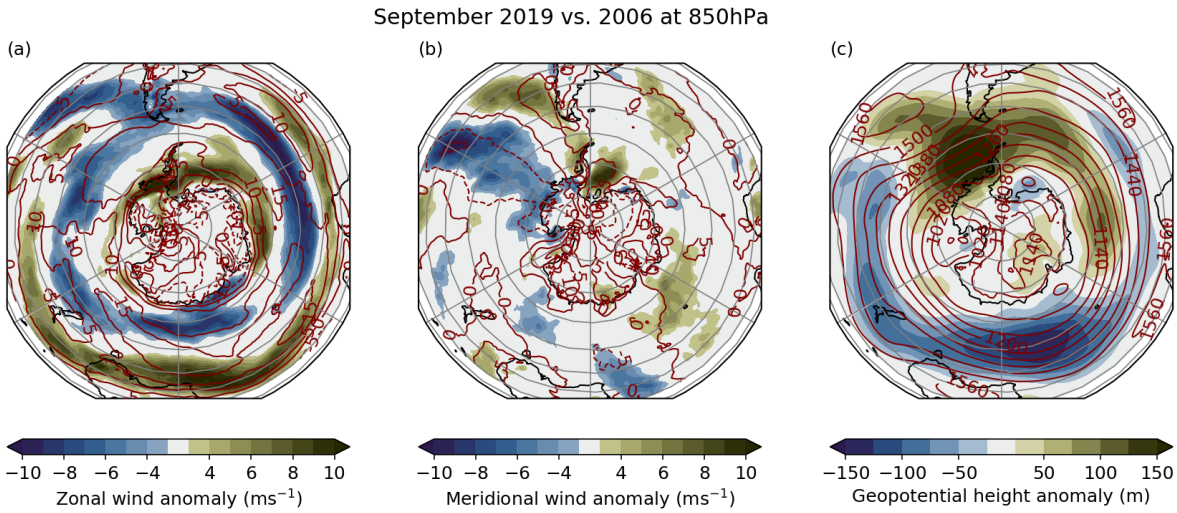

Figure 4.5.: Same as Figure 4.4 but at the 850 hPa level.

The blocking ridge dominates the monthly mean anomalies, highlighting the strength of this flow pattern. However, the upstream blocking was prevailing in the first week of September 2019. The other three weeks of September 2019 were characterized by a sequence of low- and high-pressure systems being advected with the zonal flow across the Southern Andes.

The derived MWA and the individual criteria C1, C2 and C3 for the four upstream boxes as introduced in Section 4.1 are summarized in Figure 4.6. The MWA, for which C1 (the horizontal wind at 850 hPa) is valid, is increased for all upstream boxes by 1 to 5 days in September 2019 compared to 2006. As the previous results showed, the PFJ in general is shifted poleward and the zonal wind component is strongly reduced, therefore, the increase in MWA based on validity of C1 is mainly caused by a stronger meridional component upstream of the Southern Andes. The validity of C2, the wind direction relative to the mountain range, varies for the different upstream boxes. A reduction of 3 days is detected for UP1 and UP3.2, while UP3.1 features an increase of validity of C2 of 6 days and the validity of C2 stays similar for UP2. The MWA based on C2 shows that the wind direction was most favorable for the excitation of MWs in UP3.1, which is placed zonally upstream of Tierra del Fuego. The MWA based on C3 exhibits the largest reduction of 6 to 8 days in UP1 and UP2 while the zonal and meridional upstream boxes of Tierra del Fuego. UP3.1 and UP3.2 hold similar values of C3 in 2019 as in 2006. The vertical wind shear (change of wind direction with altitude) is more pronounced in the northern part of the Southern Andes, reflecting the shift of the PFJ from that northerly position further southward to Tierra del Fuego and the Drake's passage. The MWA resulting from the combination of the three criteria (C123 in Fig. 4.6) is reduced by up to 7 days, most strongly in UP1 and UP2 while the reduction is less than 3 days in UP3.1 and UP3.2. Thus, the MWA is strongest in the UP3.1 box, indicating that the excitation and propagation conditions for MWs were most efficient above Tierra del Fuego.

Figure 4.6 shows additionally the MWA derived for October which shows only minor

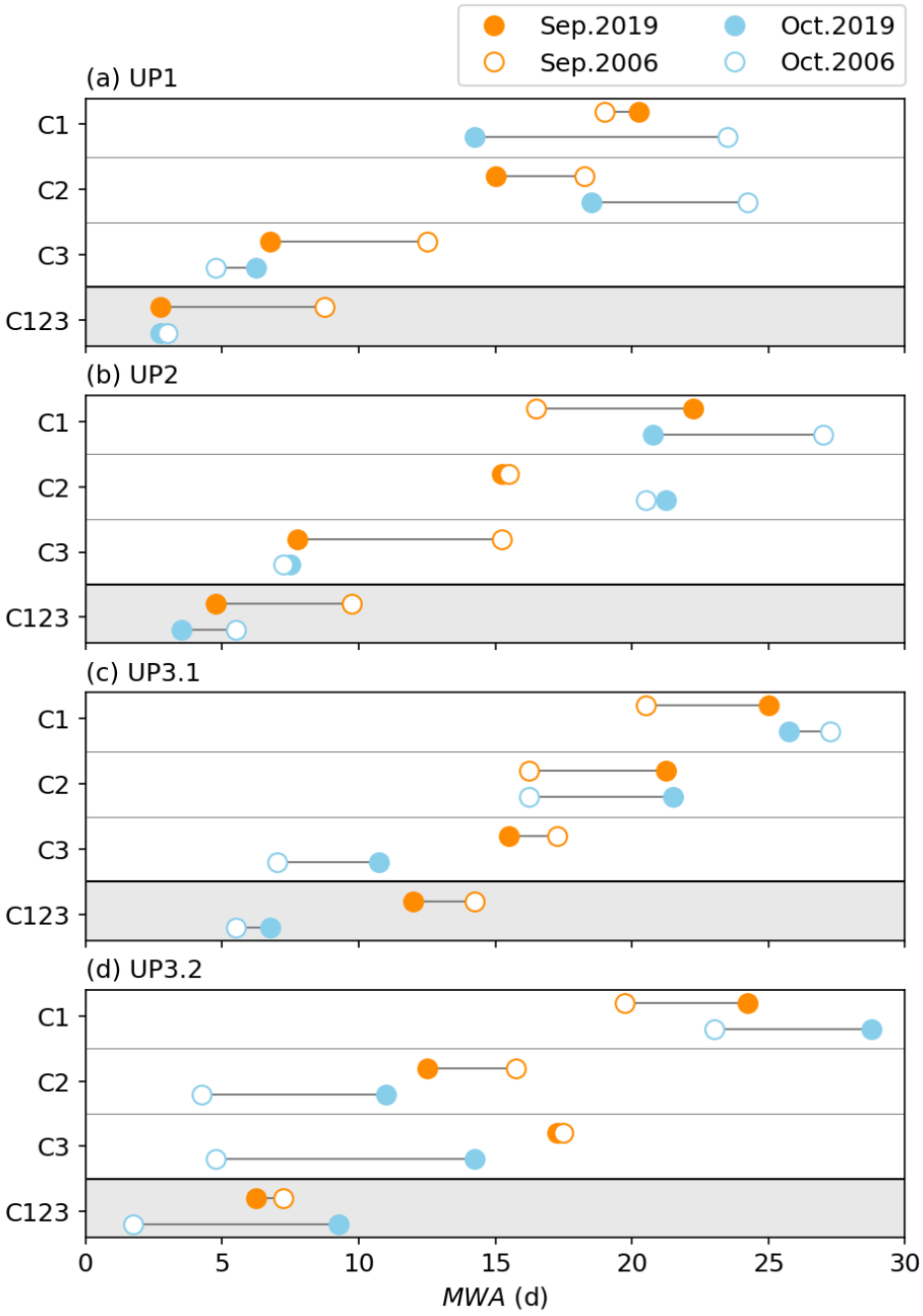

Figure 4.6.: MWA in days per month for the upstream boxes (a) UP1, (b) UP2, (c) UP3.1, and (d) UP3.2. C123 gives the total MWA based on the three individual criteria C1, C2, and C3. Horizontal bars between the dots of 2006 and 2019 highlight the difference between both years.

variations between 2019 and 2006 for UP1, UP2, and UP3.1. Especially in the northern part of the Southern Andes, UP1 and UP2, the MWA of September 2019 is equally small

like during October. In UP3.2 the MWA is increased by 8 days, highlighting that the meridional incident flow direction of Tierra del Fuego was strongly supported by the changes in the tropospheric dynamics during October 2019.

The poleward shift of the PFJ is reflected by the positive phase of the SAM index during September. Jucker and Goyal (2022) proposed a mechanism that relates the positive phase of the SAM during September 2019 with the SSW. The SSW increases the ozone concentrations in the polar lower stratosphere which cause a localized heating and greater stability of the lower stratosphere. Planetary waves get deflected near the tropopause causing wave divergence and a clockwise rotation in the troposphere. The clockwise circulation drives an anomalous upwelling over the polar cap and downwelling at lower latitudes. This circulation pattern corresponds to a positive phase of the SAM in the troposphere. Internal variability cannot be disregarded as driver of the positive phase of the SAM. The mechanism by Jucker and Goyal (2022) is comprehensible and encouraging to conclude that the SSW potentially had an influence on the poleward shift of the PFJ and, subsequently, the SSW potentially caused the differences in the excitation of MWs at the Southern Andes.

4.4. Gravity wave activity around the PNJ during the SSW

Figures 4.7 and 4.8 show the temperature perturbations T' retrieved from ALIMA observations of ST08 and ST12, respectively. Additionally, a SPV mask (dense-dotted, coarse-dotted, and no dots) is overlaid. The SPV mask presents the results of the PNJ detection algorithm: If the dense-dotted mask is shown, the ALIMA observation is located equatorward of the wind maximum of the PNJ and thus outside the SPV; if no dots are shown, the ALIMA observation is made poleward of the wind maximum of the PNJ and thus inside the SPV; if the coarse-dotted mask is shown, no PNJ was detected.

The PNJ detection and the displayed SPV mask do not explicitly reflect the critical level z_c but represent a good proxy for z_c, which is located in the altitude range of the coarse-dotted mask, where $U_H < 30$ ms^{-1}. Generally, one would need to determine z_c for each observed wave mode individually as their respective wave vectors are likely differ in orientation and thus experience different z_c. The determination of a wind reversal level, e.g. the level where the zonal wind component $u = 0$, is not sufficient, especially during September 2019 with the strongest MWA because the tropospheric flow, which excited these waves, deviated from the zonal direction.

Hence, it is not surprising that perturbations T' continue to be present within the altitude range where no PNJ is detected. Otherwise, these T' might originate from non-orographic GWs with phase speeds $c_k < 0$. Nevertheless, the large amplitudes of T' are present up to the altitude where a transition between a detected PNJ and no PNJ occurs, which is approximately at 55 km to 60 km for ST08 (Fig. 4.7) and at 40 km to 45 km for ST12 (Fig. 4.8).

Figure 4.7 illustrates nicely how GWs and the ambient wind interact. The observational

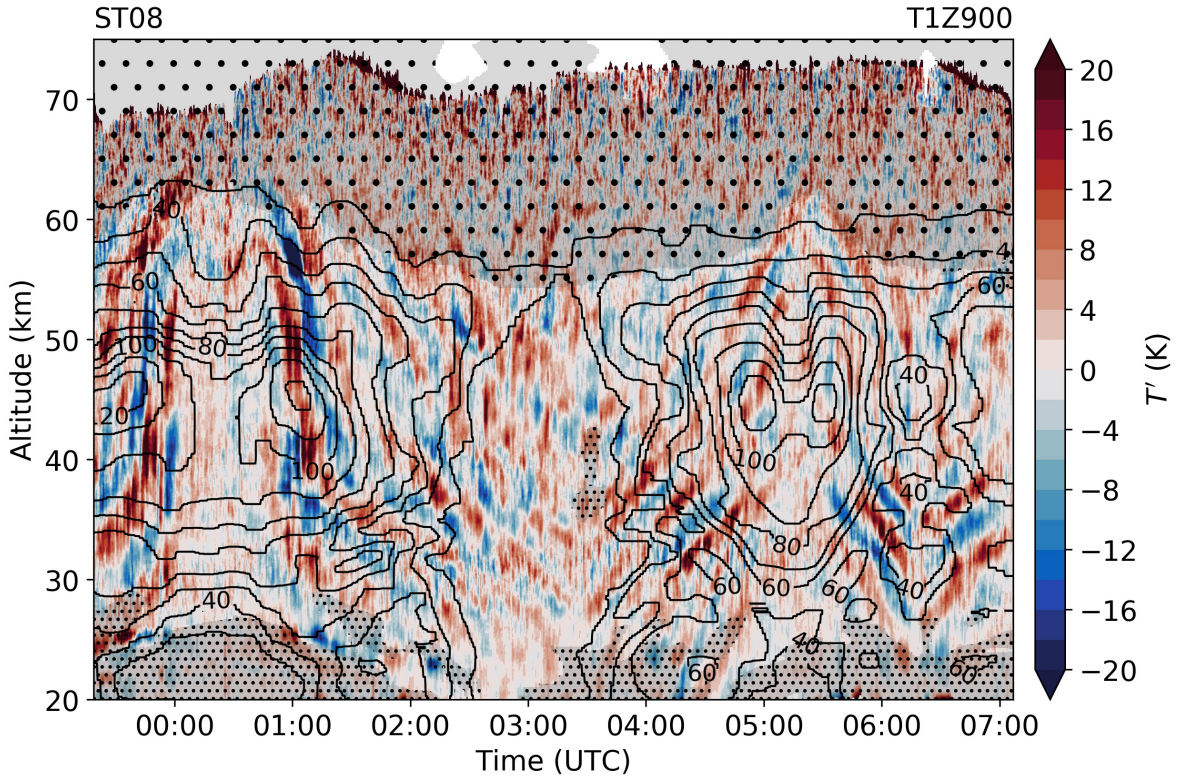

Figure 4.7.: Timeseries of temperature perturbation along the flight track of research flight ST08 with overlaid SPV mask. Dense-dotted means the ALIMA observations is outside of the SPV, no dots means inside SPV and coarse-dotted means no SPV present. Black contour lines show the horizontal wind from ERA5 along the flight track. Retrieved temperatures are of resolution T1Z900. Perturbations are derived by the subtraction of a 30 min running mean from the temperature.

curtain of ALIMA intersected with the wind maximum of the PNJ at an altitude of approximately 45 km at 23:45 UTC and 01:15 UTC. This flight section depicts an overflight of the Southern Andes (Fig. 4.2). Starting from Rio Grande to the Northwest and capturing the wind maximum for the first time, turning over the Pacific Ocean and then another overflight over the Southern Andes to the Southwest, capturing the wind maximum a second time. Therefore, the pattern of T' appears to be mirrored. The phase lines of T' incline from featuring a slope of about 45° between 30 km to 40 km altitude to a nearly vertical aligned phase lines around the wind maximum at 45 km. With the decrease in horizontal wind velocity with altitude, the phase lines gradually flatten with altitude. The observed behavior can be explained with the aid of Equation 2.17: The vertical wavelength λ_z increases for increasing ambient wind for hydrostatic MWs. Based on these observations, the observed GW structure at 23:45 UTC and 01:15 UTC are very likely hydrostatic MWs.

The horizontal distance between the PNJ and the ALIMA curtain can be determined

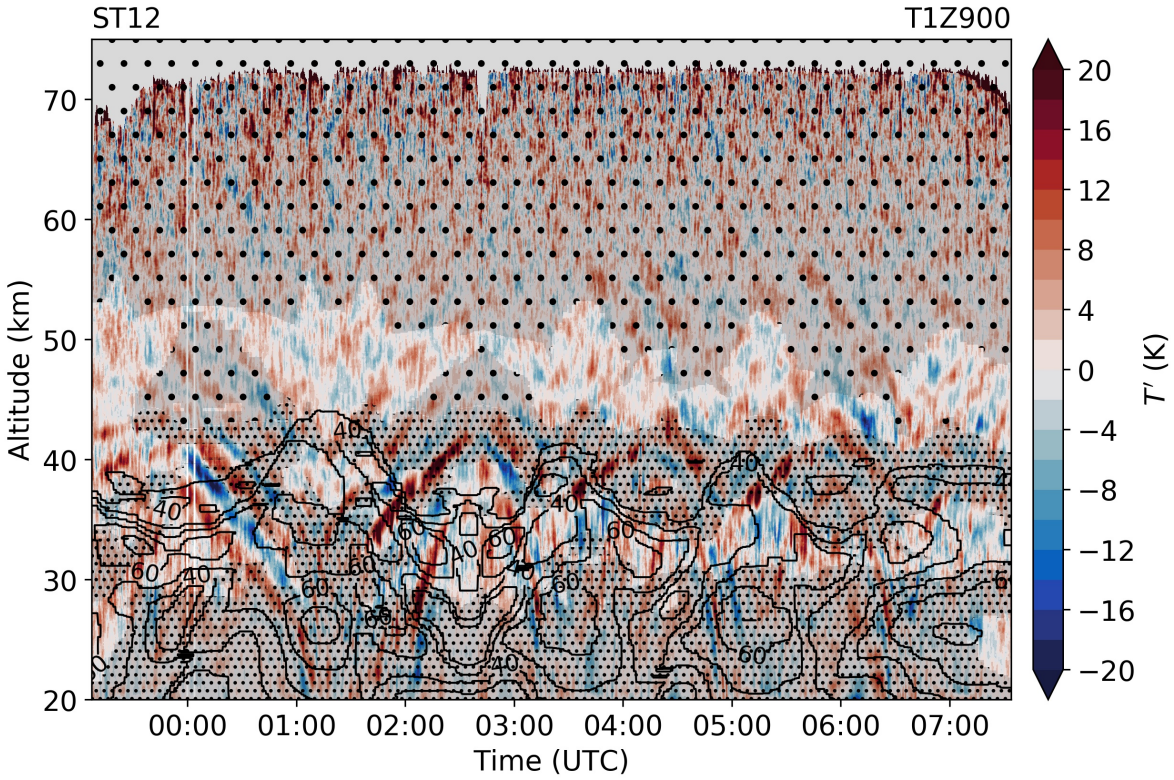

Figure 4.8.: Same as Figure 4.7 but for research flight ST12.

from the detected PNJ position. In Figures 4.9 and 4.10 the information of the horizontal distance is incorporated by the categorization *at*, *near*, and *far*. Observations from the distance range ±500 km are included in the category *at*; *near* includes the distance range ≥ 500 km and ≤ 1000 km; and *far* covers all observations with a distance > 1000 km.

Figures 4.9 and 4.10 show profiles of the averaged GW potential energy density E_p (Equation 4.1). The averaged E_p profile of ALIMA observations of all six research flights is quite erratic with altitude and includes several jumps (Fig. 4.9a). On the one hand, N is vertically smoothed over 500 m for the calculation of E_p, otherwise N includes negative values where localized but negative temperature gradients are apparent, e.g. convective instability. This smoothing might be too weak for an appropriate calculation of E_p. On the other hand, the averaged irregular E_p profile reflects the variable atmospheric conditions. The E_p profiles of ST08 (Fig. 4.9b) and ST12 (Fig. 4.9c) are more continuous in the vertical despite remaining perturbations. ST08 features on average the largest E_p values at 35 km of approximately 100 J kg^{-1}. E_p values drop to 20 J kg^{-1} around 45 km (about the stratopause altitude) and increase again in the mesosphere to 100 J kg^{-1}. Nine days later, during ST12, the largest values of the averaged E_p profile reach up to 70 J kg^{-1} in the stratosphere and drop to just 10 J kg^{-1} in the mesosphere.

The E_p profiles of the different categories undergo limited averaging due to the inclusion of less data E_p values range overall from nearly 1 J kg^{-1} to 200 J kg^{-1}. Generally, it is striking that the E_p profiles of the categories *at*, *near*, and *far* exhibit rather similar

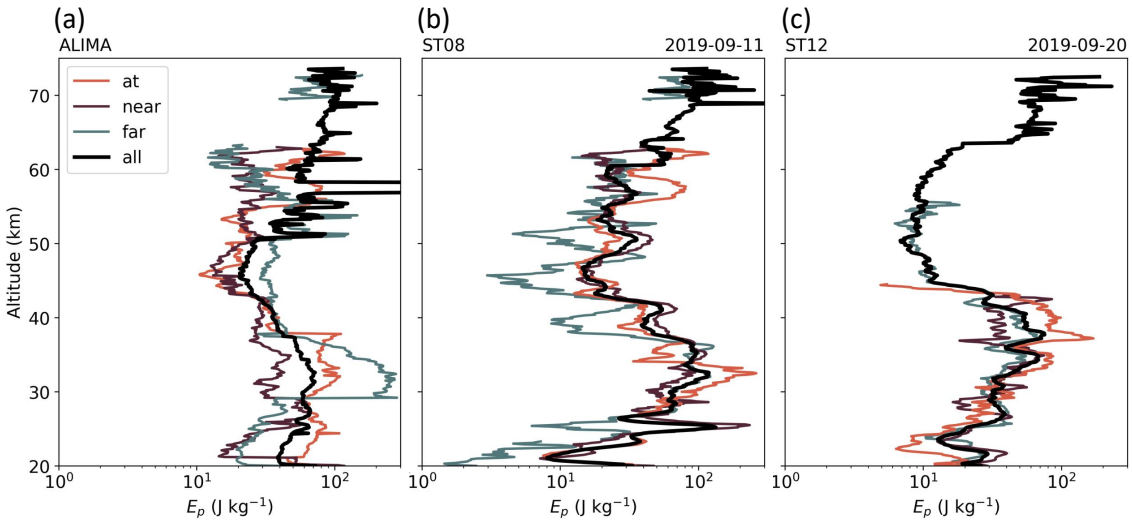

Figure 4.9.: E_p profiles based on ALIMA observations for (a) all research flights, (b) for ST08, and (c) for ST12. The black curves show the respective average E_p profile, while the colored curves show the E_p profiles for the categories *at*, *near*, and *far*.

values and none of the categories stand out, e.g. there is no evidence that the GW activity is stronger close to the PNJ.

Whiteway et al. (1997) provided insights to the GW activity distributed around the Arctic SPV based on ground-based lidar observations from Eureka. They showed that the GW activity varies depending on the position relative to the Arctic SPV in winter. Low GW activity was observed when the vortex was located above their lidar station, and high GW activity was observed at the vortex edge inside the PNJ. E_p correlated well with the strengthening of the PNJ and reduced critical-level filtering during winter (Duck et al., 2001).

There are several reasons, why such a distribution of GW activity around the SPV as shown by Whiteway et al. (1997), Duck et al. (1998), Whiteway and Duck (1999), and Duck et al. (2001) is not observed with ALIMA during the SouthTRAC-GW campaign. First, the difference between the position of the PNJ in the NH and the SH, the difference in land-sea mass between the two hemispheres and accompanied the differential position of GW sources. There is less orography in the vicinity of the position of the PNJ in the SH than in the NH. Second, the characteristics of observed GWs might differ. Whiteway et al. (1997) showed that the amplification of GW activity close to the wind maximum happens especially for MWs with long vertical wavelengths. Such a MW is present during ST08 (Fig. 4.7), but this may not be the dominant wave mode of the SouthTRAC-GW dataset. Third, the number of observations with ALIMA is much smaller than the dataset used for the examination near Eureka. Fourth, maybe the different flight patterns are not sufficient to capture the behavior of GW activity around the PNJ and fifth, the proceeding SSW and weakening of the PNJ prohibited the development of a GW activity

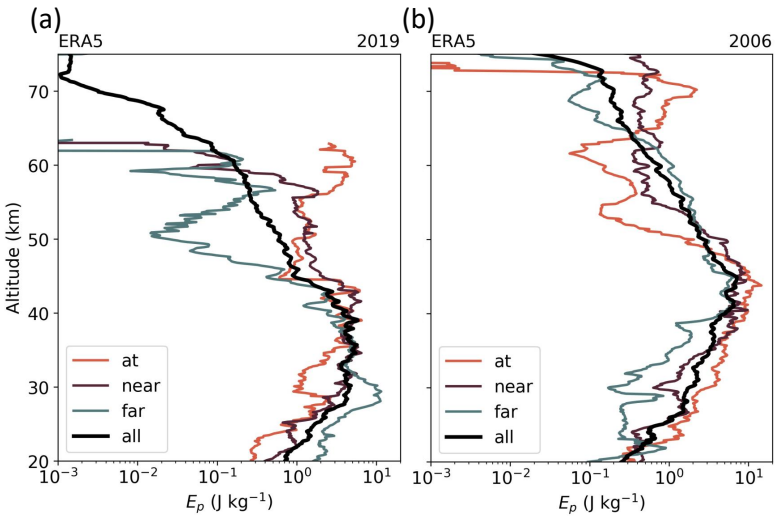

Figure 4.10.: Same as Figure 4.9a but for ERA5 data of (a) 2019 and (b) 2006.

distribution as observed during normal winter conditions.

The examination of the mentioned reasons is limited due to the lack of appropriate wind measurement in addition to the temperature estimates from ALIMA. Thus, a similar analysis as shown in Figure 4.9 is repeated for ERA5 data interpolated along the flight tracks. Figure 4.10 shows E_p profiles for the six flights in September 2019 and for the same time of the year in 2006. The E_p values derived from ERA5 data are generally much smaller due to smaller T'. The meaningfulness of the profiles decreases in the mesosphere, e.g. due to the sponge layer of the model and coarser vertical resolution (Gisinger et al., 2022). Below 40 km, different distributions of E_p values of the three different categories *at*, *near*, and *far* are visible. E_p is largest far away from the PNJ and smallest close to the PNJ in 2019 (Fig. 4.10a). The opposite appears for 2006: E_p is smallest far away from the PNJ and largest close to the PNJ. The selection of the same six dates in 2006 is rather arbitrary as completely different dynamical conditions are selected.

Thus it is rather assumable that the ALIMA observations feature no distinct distribution of GW activity around the PNJ due to the effects of the proceeding 2019 SH SSW, the rather small dataset with just six flights, as well as, general topographical and dynamical differences in the SH than NH.

4.5. Summary

This chapter presented detailed information about the 2019 SH SSW which coincided with the time frame of the SouthTRAC-GW campaign. ERA5 data and ALIMA observations are examined for the characterization of the potential MWA and of the GW activity around the PNJ. The main answers to question **(2)** are:

- The positive phase of the SAM caused a poleward shift of the PFJ. Subsequently,

the MWA exhibited variations during September 2019 compared to 2006, namely: The excitation of MWs was strongly reduced in the northern part of Southern Andes while the southernmost part experienced only little reduction in MWA. The main excitation region of MWs during SouthTRAC-GW was, therefore, the mountain range of Tierra del Fuego.

- The GW activity pattern around the SPV during the SSW did not show a distinct distribution, unlike findings from a study by Whiteway et al. (1997) in the Arctic. Topographic and dynamical differences in the SH and NH, different dominant wave modes, the influence of the preceding SSW, and the smaller dataset might have contributed to this discrepancy.

5. Horizontal wavenumber spectra across the middle atmosphere from airborne lidar observations during the 2019 southern hemispheric SSW

This Chapter has been published by Knobloch et al. (2023).

5.1. Introduction

The first research flights with an upward-pointing airborne lidar were conducted by Kwon et al. (1990) and Hostetler et al. (1991) who computed horizontal and vertical wavenumber spectra between 80 km and 100 km altitude from measurements acquired with an airborne Na lidar. Hostetler and Gardner (1994) combined Rayleigh and Na lidar observations to cover altitudes from 25 km to 40 km and 80 km to 105 km while Rayleigh lidar observations from Gao and Meriwether (1998) ranged from 30 km to 45 km. All the findings from these early airborne lidar studies have in common that their horizontal wavenumber spectra in the troposphere, stratosphere and upper mesosphere support GWs as the underlying dynamical process for determining the horizontal wavenumber dependence in the mesoscale range.

The mesoscale dynamics are characterized by horizontally rotational and horizontally divergent modes. In theoretical work it has been argued that the horizontal wavenumber dependence can be described by stratified turbulence associated with a forward inertial energy cascade (Lindborg, 2006; Brune and Becker, 2013; Li and Lindborg, 2018) or by GWs associated with an inertial energy cascade from larger to smaller scales (Dewan, 1979; VanZandt, 1982; Hostetler and Gardner, 1994; Bacmeister et al., 1996; Gao and Meriwether, 1998), including further work on saturated-cascade (Dewan, 1994; Dewan, 1997), linear-instability (Gardner et al., 1993) and diffusive filtering of GWs (Gardner, 1994).

Recent studies using idealized and NWP simulations indicate that the mesoscale $k^{-5/3}$ spectral shape, with k as horizontal wavenumber, is influenced by buoyancy driven motions and by an inertial energy cascade (Waite and Snyder, 2009; Sun et al., 2017; Menchaca and Durran, 2019; Selz et al., 2019). Menchaca and Durran (2019) found that MWs have a major impact on the energy spectrum: linear waves entirely constitute the divergent mode while breaking waves energize rotational and divergent modes.

The questions which dynamical mechanism underlies the mesoscale $k^{-5/3}$ spectrum and

whether there is a universal dynamical mechanism at all have still not been unequivocally answered, as studies suggest that the spectral energy is rather intermittent because of the intermittency of the dynamical processes, e.g. convection or GWs (Selz et al., 2019; Menchaca and Durran, 2019). However, knowing and understanding the atmospheric spectra is of importance for NWP and atmospheric predictability (Charney, 1971), and for the development and application of GW parameterizations in all layers of the atmosphere (Kim et al., 2003; Plougonven et al., 2020; Harvey et al., 2022).

In this paper we close the gap in altitude coverage of previous measurements and present horizontal wavenumber spectra of lidar photon counts (proportional to density) across the middle atmosphere from 20 km to 80 km altitude. The spectra were calculated from measurements by ALIMA onboard the HALO taken during the SouthTRAC-GW campaign in 2019 (Rapp et al., 2021). The aim of this Chapter is to investigate the horizontal wavenumber spectra over the southern hemispheric hotspot for MWs in the middle atmosphere with ALIMA. Recent technological advances since the first airborne lidar observations in the 1990s have improved the data quality, resolution and altitude range of airborne lidar measurements (Kaifler and Kaifler, 2021). Based on these data, we will consider the following research questions:

(3) What is the shape of horizontal wavenumber spectrum throughout the middle atmosphere in the vicinity of the MW hotspot above the Southern Andes?

(4) How is the horizontal wavenumber spectrum in the middle atmosphere affected by GWs and the SSW?

The Chapter is structured as follows: in section 5.2 the spectral analysis is described. In section 5.3, we present the middle atmospheric horizontal wavenumber spectra. The consequence of the unknown orientation of wave vectors, the role of GWs and the SSW for the horizontal wavenumber spectra, are discussed in section 5.4, followed by our conclusions in section 5.5.

5.2. Spectral analysis

The horizontal wavenumber spectra presented in this study are based on the range corrected photon counts $\gamma(t, z)$ from ALIMA with t and z denoting time and altitude, respectively. $\gamma(t, z)$ is proportional to atmospheric density and thus horizontal wavenumber spectra are proportional to potential energy.

The ALIMA photon counts are about two orders of magnitudes larger compared to the first airborne Rayleigh lidar observations by Hostetler and Gardner (1994) and Gao and Meriwether (1998) which highlights the advance of the lidar technology in the last 30 years and allows us to extend our altitude range of observations throughout the entire middle atmosphere.

We use the photon counts of the low channel below 30 km, the far channel above 50 km and the mid channel between 30 km to 50 km. First, the measurements of each research flight are separated into individual flight legs, which are straight and of near

constant pressure altitude. The observations are screened for instrumental effects, e.g. temporary drops in the SNR due to misalignment of the laser beam or icing on the laser window. Overall, 43 flight legs with travelled distances between 150 km and 2400 km are considered in the spectral analysis. Detailed information of the individual flight legs can be found in the Appendix B. Lidar photon count profiles are temporally integrated to a 1 min resolution and smoothed in the vertical with a 900 m Locally Weighted Scatterplot Smoothing (LOWESS) filter. A filter width of 900 m is large enough to i) satisfactorily reduce photon noise and ii) small enough to not attenuate vertical scales that are above the noise floor and not noticeably affect the horizontal scales (See Appendix D). Second, $\gamma(t,z)$ is normalized by a respective temporal average of each flight leg:

$$\gamma'(t,z) = \frac{\gamma(t,z)}{\overline{\gamma(z)}} \tag{5.1}$$

The normalization eliminates the exponential decrease of photons counts with altitude due the decreasing air density. Remaining fluctuations of photon counts are either caused by geophysical processes, e.g. GWs, or by photon noise (See Chapter 3).

The spectra are presented as the Power Spectral Density (PSD):

$$PSD_\gamma(k) = |\hat{\gamma'}(k)|^2 * \frac{\Delta x^2}{X} \tag{5.2}$$

where $\hat{\gamma'}(k)$ is the Fast Fourier Transform (FFT) of γ'. Δx and X are the horizontal bin size and the length of a flight leg, respectively. The horizontal wavenumber spectra are calculated between altitudes of 20 km to 80 km for each vertical bin (every 100 m) and, for statistical certainty, averaged over an altitude range of 10 km. Above 80 km the signal is dominated by photon noise.

The horizontal wavenumber k and the horizontal wavelength λ_k are given by:

$$\lambda_\mathrm{k} = \mathrm{k} \cdot \Delta x, \quad \mathrm{k} = [1,2,3,...,n], \quad k = \frac{2\pi}{\lambda_\mathrm{k}}, \tag{5.3}$$

where $n = X/\Delta x$ and $\Delta x = \tau \cdot \overline{GS_{HALO}}$ with τ as temporal spacing and $\overline{GS_{HALO}}$ as the leg mean ground speed of HALO. During the research flights GS_{HALO} varied due to changing horizontal winds. The actual spacing of the measurements in the horizontal is thus irregular (Cho et al., 1999b). However, the absolute error in subsequent λ_k due to the usage of a leg mean ground speed instead of the time varying ground speed is small (0.03 % - 0.9 %). The smallest λ_k is typically between 22 km and 30 km, considering the sampling rate in space which depends on GS_{HALO}, the temporal integration of 60 s and the Nyquist-frequency.

As the flight legs have different lengths and $\overline{GS_{HALO}}$, the calculated horizontal wavenumber spectra are interpolated to the same values of k and λ_k before averaging over all flight legs and research flights to obtain flight-mean spectra and SouthTRAC-GW-mean spectra.

Additionally, photon noise spectra for each flight leg are calculated based on $\overline{\gamma(z)}$ and the assumption that the photon noise follows a Poisson distribution. The calculation is repeated 1000 times in a Monte-Carlo experiment. The obtained mean photon noise spectra reveal white noise and are constant over all scales (Fig. 5.1b).

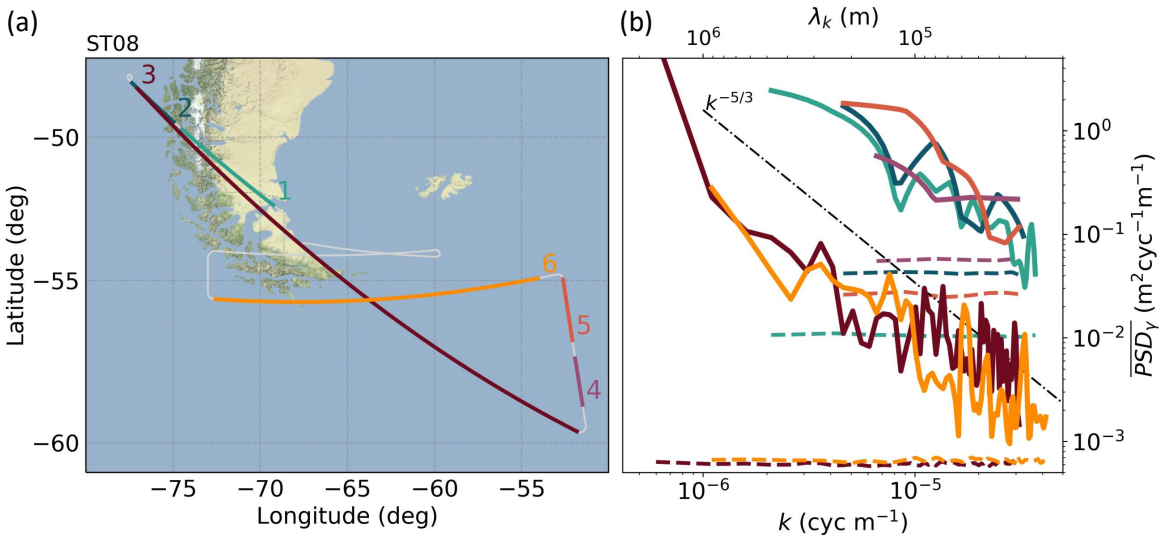

Figure 5.1.: Flight track and individual flight legs of flight ST08 (a) and corresponding mean horizontal wavenumber power spectra of relative density perturbations (b) between 50 km and 60 km altitude. Horizontal dashed lines in (b) show the mean horizontal photon noise spectra and the dashed-dotted line indicates a $k^{-5/3}$ slope.

5.3. Middle atmospheric horizontal wavenumber spectra

Figure 5.1 shows an example of the spectral analysis of the individual flight legs between 50 km and 60 km altitude from research flight ST08 on the 11 September 2019 23:00 UTC to 12 September 2019 07:00 UTC. Flight legs 1, 2, 4 and 5 are separated because of a temporary drop in the SNR caused by a misalignment of the laser beam. All flight legs of ST08 show a similar slope of $k^{-5/3}$ and are well above their respective noise floors. The largest values of $\overline{PSD_\gamma}$ appear in flight legs 4 and 5 over the Scotia Sea and in flight legs 1 and 2 over Patagonia and the Southern Andes (Fig. 5.1a, b).

The distribution of $\overline{PSD_\gamma}$ integrated over the $\lambda_k = 50$ km to $\lambda_k = 150$ km spectral range of all 43 flight legs classified for their position above *Land*, *Ocean* or both (*Land/Ocean*) is shown in Figure 5.2. The $\overline{PSD_\gamma}$ values were scaled by the respective $\overline{PSD_\gamma}$ of photon noise. This is necessary in order to make flights and legs comparable in $\overline{PSD_\gamma}$. The signal strength strongly varies for the different research flights and decreases with altitude. Hence, the relative impact of the photon noise increases. Therefore, normalized $\overline{PSD_\gamma}$ gets smaller with altitude. The largest values and the greatest variability of $\overline{PSD_\gamma}$ are found above the ocean. However, $\overline{PSD_\gamma}$ is on average smaller over the ocean than over land. In the stratosphere the 75 percentile and upper whisker of the category above ocean are similar in $\overline{PSD_\gamma}$ to above land (Fig. 5.2a) while in the mesosphere the 75 percentile and upper whisker are larger above the ocean than above land (Fig. 5.2b).

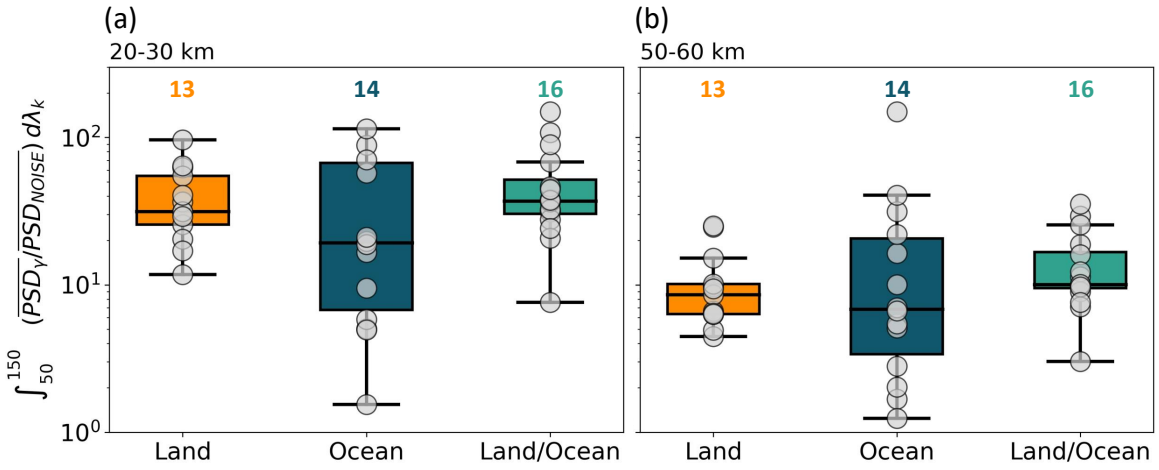

Figure 5.2.: Normalized $\overline{PSD_\gamma}$ integrated over the spectral range $\lambda_k = 50$ km to $\lambda_k = 150$ km of all 43 flight legs in the altitude range 20 - 30 km (a) and 50 - 60 km (b) and classified for their position above land, ocean or land/ocean. The boxplots feature the median, 25 and 75 percentiles (inner quartile range), and the whiskers that extend to smallest/largest non-outliers. The colored numbers give the number of legs for each category.

Flight legs that were flown above land and ocean include large values of $\overline{PSD_\gamma}$ but a rather small variability of the inner quartile range.

Figure 5.3 shows the mean horizontal wavenumber spectra of observed photon counts for horizontal scales from 2000 km to 22 km between 20 km to 80 km altitude. Additionally, the 3σ-value of the photons noise is shown. Normally, the noise floor would be constant across the horizontal wavenumbers (Fig. 5.1b), however due to the averaging of legs of different length the variability of the photon noise is the largest for $50 < \lambda_k < 150$ km (all 43 flight legs fall into this range).

Values of normalized $\overline{PSD_\gamma}$ close to 1 indicate the signal approaching the noise floor while values of normalized $\overline{PSD_\gamma}$ larger than the 3σ-value (outside the grey-shaded area) indicate a large SNR and thus statistically significant data. Except for the highest altitude range and research flight ST10, the signal approaches the noise floor, if at all, at the smallest resolved scales. For the highest altitude range from 70 km to 80 km the noise limit is reached at $\lambda_k \sim 200$ km to 500 km (Fig. 5.3f). The flight legs of research fight ST10 had a constant but much weaker signal compared to the other flights due to icing of the laser window, which resulted in a higher absolute noise floor.

Generally, the spectral slopes in Figure 5.3 are close to $k^{-5/3}$ and partly flatten at higher wavenumbers to a shallower spectral slope depending on the altitude range, research flight and the horizontal wavenumber. In the upper stratosphere and mesosphere only the horizontal wavenumber spectra of research flight ST08 (at the beginning of the SSW) follow closely the $k^{-5/3}$ slope while the other research flights (during the SSW) feature a reduction of approximately 25 % in $\overline{PSD_\gamma}$ at $\lambda_k \sim 200$ km and a transition to a shallower slope at larger λ_k (Fig. 5.3c, d, e).

Figure 5.3.: (Figure on next page) Mean horizontal observed wavenumber spectra of photon counts normalized with the respective photon noise spectra for all research flights (colored lines), the average over all flights (black line) and the average over all flights except ST08 (black dashed line) in the range 20 - 30 km (a), 30 - 40 km (b), 40 - 50 km (c), 50 - 60 km (d), 60 - 70 km (e) and 70 - 80 km (f). The horizontal dashed line marks the noise floor and the grey shading the 3σ-value of photon noise. The dashed-dotted line indicates a $k^{-5/3}$ slope.

For all research flights, $\overline{PSD_\gamma}$ increases with altitude. However, due to the normalization applied before averaging, this behavior is not visible anymore in Figure 5.3. We also want to point out that the signal strength of the lidar return signal affects the $\overline{PSD_\gamma}$ of photon spectra. This becomes apparent at altitudes where switches of detection channels with higher to lower sensitivity take place, e.g. smaller $\overline{PSD_\gamma}$ and larger 3σ-values in the altitude ranges 30 km to 40 km and 40 km to 50 km (Fig. 5.3). Finally, few long legs were flown and as a consequence, the averages include ≤ 7 of spectra with $\lambda_k > 1000$ km.

5.4. Discussion

5.4.1. Orientation of wave vectors

The observed wavelengths are not true wavelengths. The observed wavelength is the distance between wave fronts sampled along the flight track with an unknown angle of intersection. If a wave is sampled at an angle of 60° relative to its wave vector, the true wavelength is half of the observed wavelength. If the angle approaches about 85°, the true wavelength will be about one order of magnitude smaller than the observed wavelength.

The unknown orientation of the observed GWs introduces a potential complication for the interpretation of the spectral analysis. While sampling multiple waves in one flight leg, we can not necessarily assume that all of them have the same wave vector. This complication affects all past airborne spectral analyses, (Nastrom and Gage, 1985; Kwon et al., 1990; Hostetler et al., 1991; Hostetler and Gardner, 1994; Bacmeister et al., 1996; Gao and Meriwether, 1998; Cho et al., 1999b), and, to our knowledge, has not been discussed previously.

Each observed horizontal wavelength may be shifted to a smaller true horizontal wavelength, which influences the spectral shape. In order to investigate this influence, we performed Monte-Carlo experiments. Each wavenumber of a given horizontal wavenumber spectrum is N times randomly perturbed by a perturbation in wave orientation $0° \leq \alpha \leq 90°$ drawn from a Gaussian (experiment A) with an expected value $\alpha = 0°$ and uniform (experiment B) distribution, e.g. $\lambda_k * \cos(\alpha)$ (see Fig. C.2). Experiment A represents the case of flight legs which are rather aligned with the wave orientation and experiment B regards a random orientation of flight legs with respect to waves.

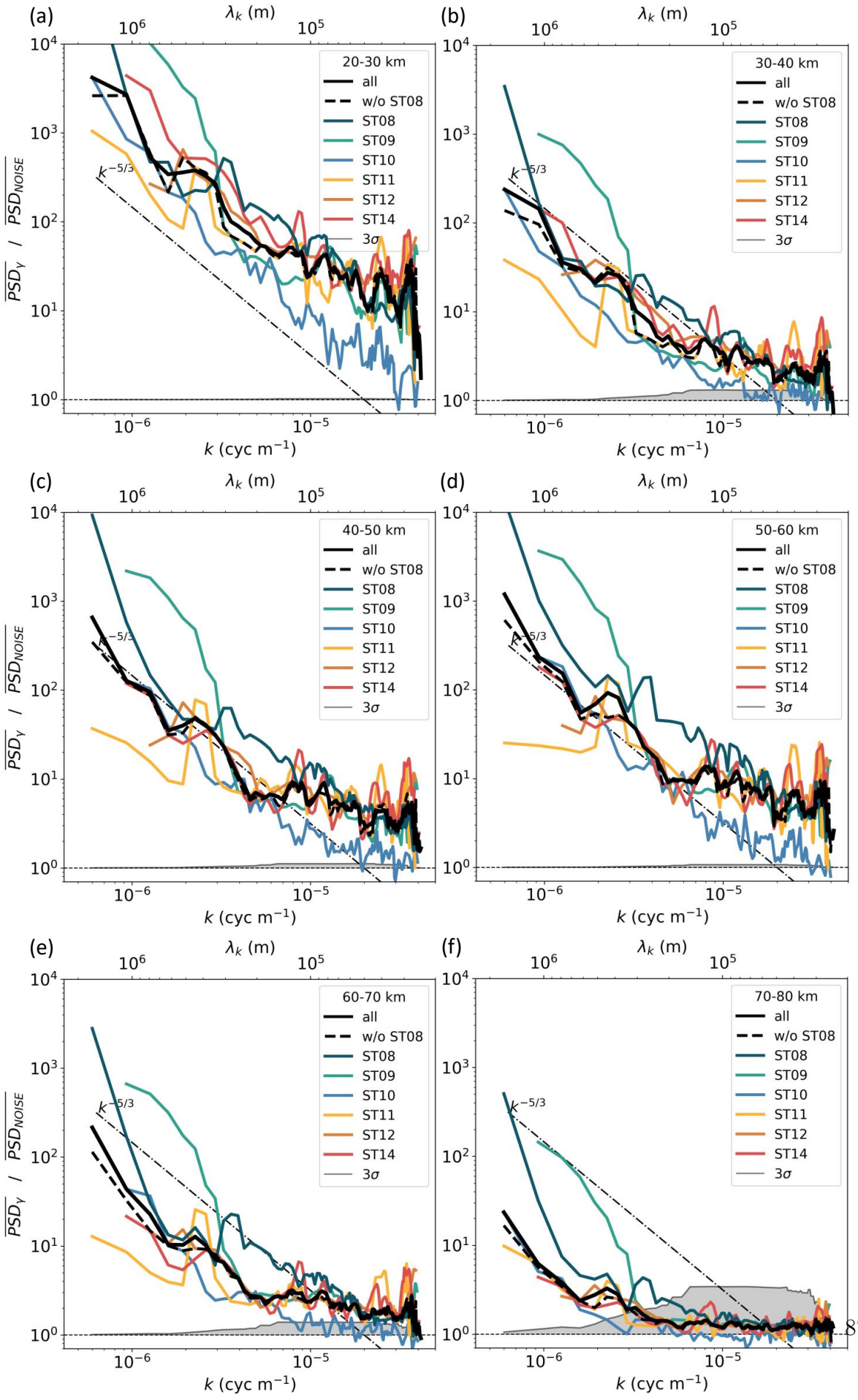

Figure 5.3.: (Caption on previous page.)

For both experiments no significant difference (p-value > 0.1) but still a large correlation (pearson coefficient > 0.94) was found between the given and the averaged randomly perturbed horizontal wavenumber spectra for $N > 5$ realizations. In general, a shift in horizontal wavenumber can be expected but the experiments reveal only a minor influence on the spectral shape if the number of averaged spectra is sufficiently large ($N > 5$). Therefore, we conclude that the presented flight-means of ST08, ST09, and ST12 and the SouthTRAC-GW-mean spectra are robust in spectral shape for $\lambda_k < 1100$ km. For larger λ_k, less than five flight legs were long enough that the amount of flight legs is not sufficient anymore for a robust statistic. The number of legs N of ST10, ST11 and ST14 are < 5 (see Tab. B.1). Still, the spectral slopes of these flights are similar to the spectral slopes of ST09, ST14 and the SouthTRAC-GW-mean, suggesting that unknown wave orientations have a negligible impact even in the case of a small number of averaged spectra.

The differences in orientation between the wave vectors and the flight path do not affect the spectral amplitudes as long as at least one full wavelength is sampled (see Fig. C.1). If this condition is not fulfilled, the spectral amplitudes are underestimated.

5.4.2. Physical cause of spectral slope

The horizontal wavenumber spectra are close to $k^{-5/3}$ in the stratosphere for all observed horizontal scales down to $\lambda_k \approx 100$ km. In the mesosphere, the spectral slope is close to $k^{-5/3}$ for $\lambda_k > 300$ km. For $\lambda_k < 100$ km, the spectral slope tends to be shallower than $k^{-5/3}$, similar to results in the mesopause region found by Kwon et al. (1990). However, why the mesoscale range follows a $k^{-5/3}$ power law dependence (Nastrom and Gage, 1985) or why it deviates from $k^{-5/3}$ (Kwon et al., 1990; Hostetler et al., 1991; Bacmeister et al., 1996), is still an open question for the scientific community.

Lindborg (2006) proposed that GW spectra in the middle atmosphere are affected by stratified turbulence arising from nonlinear dynamics and predicted that observed horizontal GW spectra would exhibit a spectral slope of $k^{-5/3}$. The vertical resolution of the ALIMA observations (100 m grid with 900 m smoothing) is coarser than the vertical resolution needed for the detection of layers of stratified turbulence (Lindborg, 2006; Brune and Becker, 2013). Therefore, and due to the vertical averaging over 10 km altitude ranges, our horizontal wavenumber spectra cannot be associated with stratified turbulence (Rodriguez Imazio et al., 2023) nor can we exclude the occurrence of stratified turbulence. Our findings support the prediction by Lindborg (2006).

5.4.3. Impact of the SSW

The reduction of $\overline{PSD_\gamma}$ at horizontal wavelengths of about 100 km to 300 km for all research flights except ST08 above 40 km or 50 km altitude was potentially caused by the co-occurring SSW. The SSW induced a critical level for vertically propagating MWs due to the slowing of the PNJ and the displacement of the SPV. During ST08, the observed MWs were able to propagate up to 65 km altitude while MWs were filtered by the critical level at about 40 km altitude during ST12 (see Fig. 4a, 12b, d in Rapp et al.

(2021)) and other research flights. The decrease in GW activity in the mesosphere due to the SSW during flights ST09, ST10, ST11, ST12, and ST14 resulted in a decrease of $\overline{PSD_\gamma}$ by 25 % in the range 300 km $> \lambda_h >$ 100 km. This result suggests that these are wavelengths of MWs excited by the Southern Andes. Furthermore, the spectra of flights ST09, ST10, ST11, ST12, and ST14 obey no distinct $k^{-5/3}$ slope for 300 km $> \lambda_h >$ 100 km in the mesosphere. This spectral response to the SSW highlights the sensitivity of the horizontal wavenumber spectra to the temporal decline in MW activity and ultimately the absence of MWs. Turning the argument around, the observed decrease in spectral power due to the decreased MW activity during the SSW supports GWs as driver of the $k^{-5/3}$ slope of the mesoscale range in the middle atmosphere.

5.4.4. Land vs. ocean

On average, the study found only slightly smaller values of $\overline{PSD_\gamma}$ over ocean than over topography, while the largest individual values occurred over ocean. Previous studies detected an enhanced spectral power above orography compared to smooth terrain or ocean (Lilly and Petersen, 1983; Nastrom et al., 1987; Gao and Meriwether, 1998).

There are two potential causes for the observed enhancement of spectral energy over the ocean: 1) horizontal MW propagation and 2) non-orographic GWs. The large values of $\overline{PSD_\gamma}$ over the ocean were observed during unique stratospheric dynamical conditions associated with the SSW. Generally, the occurrence of a SSW diminishes the MW activity in middle atmosphere and the contribution of non-orographic GWs preponderates. Still, Geldenhuys et al. (2023) and Krasauskas et al. (2023) provided evidence for cases of horizontal MW propagation, e.g. refraction, during flight ST08 and ST12.

5.5. Conclusions

High-resolution and high-quality observations by ALIMA enabled the determination of horizontal wavenumber spectra of density within the horizontal scale range of 2000 km to about 22 km across the middle atmosphere from 20 km to 80 km altitude during SouthTRAC-GW. The presented horizontal wavenumber spectra are the first based on airborne lidar observation between 40 km and 80 km altitude and during a SSW.

Our main findings are:

- The averaged horizontal wavenumber spectra are statistically robust, rather smooth and exhibit slopes close to $k^{-5/3}$ in the stratosphere even though the number of research flights and flight legs was limited;
- The derived horizontal wavenumber spectra in the middle atmosphere are influenced by horizontally and vertically propagating MWs and potentially non-orographic GWs; and
- The SSW caused an attenuation of spectral power of the horizontal wavenumber spectra in the mesosphere.

The impacts of horizontal MW propagation, non-orographic GWs and GW–SSW interactions on the horizontal wavenumber spectra support the importance to include such processes in future GW parameterizations (Plougonven et al., 2020). However, since SouthTRAC-GW coincided with the SSW, it is difficult to generalize our conclusions. Observed deviations from $k^{-5/3}$ for $\lambda_k < 200$ km in the mesosphere might be less distinct or not present during strong SPV conditions and without a critical level for MWs, e.g. as during research flight ST08 which featured a spectral slope close to $k^{-5/3}$ in the lower mesophere.

Turning to the research questions **(3)** and **(4)** we formulated in the beginning, we infer concerning the question **(3)** that the derived horizontal wavenumber spectra across the middle atmosphere are close to $k^{-5/3}$. Deviations from this canonical spectral slope mainly appear for $\lambda_k < 300$ km in the mesosphere. Regarding the question **(4)**, we conclude GWs and the SSW have a relevant influence on the horizontal wavenumber spectra. Altogether, this study provides observational evidence that the $k^{-5/3}$ spectral slope in the middle atmosphere can be explained by the occurrence of GWs.

Future applications of ALIMA can be used for e.g. studying of horizontal wavenumber spectra of GWs in the middle atmosphere during strong SPV conditions or the in-depth investigation of horizontal GW propagation. The planned extension of ALIMA by an iron resonance lidar channel (Kaifler et al., 2017) will extend the vertical measurement range into the lower thermosphere and allow for wind measurements. Wind measurements are required for future applications of an airborne lidar in order to estimate the character of the observed GWs.

6. Summary

During the 2019 SouthTRAC-GW campaign, the ALIMA instrument was deployed to conduct horizontally resolved high-resolution observations of the middle atmosphere. This thesis aimed to analyze and evaluate uncertainties and biases in the ALIMA observations and to explore GWs in the middle atmosphere. The combination of ALIMA observations, lidar simulations, EULAG simulations and ERA5 data was used to investigate the central hypothesis of this thesis: **Airborne lidar observations are well-suited for the exploration of GWs in the middle atmosphere.**

The thesis studied photon count profiles of ALIMA and the temperature retrieval in Chapter 3 and evaluated question **(1)**: How accurate and precise are the densities and temperatures derived from ALIMA observations?

Several factors that impact ALIMA's observations and the accuracy of retrieved temperatures were identified. These factors encompassed elements such as the photon noise, the photon background, the influence of atmospheric transmission (which includes Rayleigh extinction and absorption by ozone), initialization procedures, numerical effects, and the underlying hydrostatic assumption made during temperature retrieval. The thesis emphasized that further conditions, such as the aircraft's flight maneuvers and variations in ozone concentration, could introduce additional complexities to the retrieved temperature data.

The thesis revealed a significant insight: a 1 % difference in photon counts corresponded to a discernible temperature difference ΔT in the range of 0.5-0.65 K. The analysis identified that ALIMA features an altitude-dependent bias of approximately $\pm$ 1 K and an altitude-dependent uncertainty ranging from $\pm$ 1 K to $\pm$ 6 K for the high temporal resolution of $\Delta t = 1$ min. These uncertainties were consistent when applying the standard error correction methods employed in ALIMA's data processing. Similar trends were observed when assessing density measurements, where an altitude-dependent bias of around $\pm$ 0.4% and an altitude-dependent uncertainty spanning $\pm$ 0.7 % to $\pm$ 2 % were reported.

The thesis also delved into the intricate relationship between non-hydrostatic GW modes and the temperature retrieval in Chapter 3. It has been demonstrated that the conventional hydrostatic temperature retrieval approach, when applied in the presence of non-hydrostatic MWs, led to erroneous temperature estimates. This error is due to the hydrostatic assumption's inability to account for vertical wind shear and the non-hydrostatic characteristics of these MWs. Consequently, temperature perturbations induced by MWs are systematically underestimated by 5 % to 20 %. The analysis indicated that non-hydrostatic MWs could be excited even in regions where the underlying orography might suggest a primarily hydrostatic response. Moreover, it highlighted that

the magnitude of this error depended on factors such as the GW's amplitude, altitude, wavelength, and the vertical wind velocity.

The error budget analysis indicated a rigorous assessment of the observational technique, which is crucial for understanding the accuracy and precision of the ALIMA measurements, and indicates a deep understanding of the potential sources of error in airborne lidar observations. The quantitative assessment of ALIMA observations contributes to a better understanding of the reliability of airborne lidar observations.

The thesis further explored the implications of the 2019 SH SSW on the large-scale and GW dynamics in Chapter 4 by evaluating question **(2)**: What was the dynamical condition during SouthTRAC-GW and how did it impact the observed GWs?

A poleward shift of the PFJ due to the positive phase of the SAM index affected the excitation and propagation of MWs, which was expressed as MWA. Variations in MWA between September 2019 and 2006 were present, a notably reduced MWA in the northern part of the Southern Andes and enhanced MWA above Tierra del Fuego. Regarding the GW activity around the SPV, unlike studies revealed from Arctic observations, no clear distribution pattern was observed around the austral SPV. Discrepancies were attributed to hemispheric differences, dominant wave modes, and the preceding SSW, rather than insufficient ALIMA sampling.

This indicates that the observational technique of an airborne lidar is sensitive to dynamic events, such as the SSW, and can provide insights into their impact on the middle atmosphere.

Novel horizontal wavenumber spectra based on ALIMA observations were presented in Chapter 5 with a special focus on questions **(3)** and **(4)**: What is the shape of horizontal wavenumber spectrum throughout the middle atmosphere in the vicinity of the MW hotspot above the Southern Andes? And how is the horizontal wavenumber spectrum in the middle atmosphere affected by GWs and the SSW?

Horizontal wavenumber spectra based on density were determined between 20 km and 80 km altitude and covered horizontal scales from 2000 km to 22 km. These spectra were the first from an airborne lidar between 40 km and 80 km altitude and generally during a SSW. The horizontal wavenumber spectra were found to be statistically robust for horizontal scales smaller 1100 km and they exhibited a $k^{-5/3}$-dependence in the middle atmosphere with deviations seen for horizontal scales smaller 300 km in the mesosphere. The horizontal wavenumber spectra were influenced by horizontally and vertically propagating MWs and potentially non-orographic GWs. Spectral power was attenuated in the mesosphere due to the prevailing SSW. Overall, the analysis provided observational support for the $k^{-5/3}$-dependence attributed to GWs in the middle atmosphere.

The evaluation implies that the observational technique of an airborne lidar is capable of characterizing the spectral properties of GWs in the middle atmosphere, providing valuable data for understanding their behavior and dynamics. Notably, the mesospheric spectral power exhibited a reduction due to the SSW. The reduction of spectral power emphasized the relevance of considering horizontal GW propagation and the interactions

between GWs and SSWs when developing future parameterizations for GW dynamics.

It can be assessed that the hypothesis holds true. The thesis presented a comprehensive evaluation of the capabilities and limitations of the airborne lidar instrument ALIMA in exploring GWs in the middle atmosphere during the 2019 SouthTRAC-GW campaign.

In conclusion, the thesis supports the hypothesis that airborne lidar observations are indeed well-suited for exploring GWs in the middle atmosphere. The thesis's detailed analysis, the comprehensive error budget, and the investigation of GW dynamics collectively demonstrated the effectiveness and suitability of airborne lidar for advancing the understanding of GW dynamics in the middle atmosphere.

As for the future prospects of ALIMA, the thesis suggested employing ALIMA for studying horizontal GW spectra under strong SPV conditions and investigating the nuances of horizontal GW propagation. The upcoming enhancement of ALIMA's capabilities with the incorporation of an iron resonance lidar channel will extend the vertical measurement range into the lower thermosphere and enable wind measurements. These wind measurements are vital for accurately characterizing observed GWs and their interaction with the ambient wind, since the wind is responable for selecive filtering of wave modes, changes in the vertical wavelength and Doppler shifting.

The airborne Rayleigh lidar ALIMA is adaptable and evolving to meet the needs of more specified observations of the middle atmosphere for further research. The extended ALIMA instrument is intended to perform such observations in the follow-on campaign *WAVEGUIDE* in the near future.

A. Temperature dataset by ALIMA

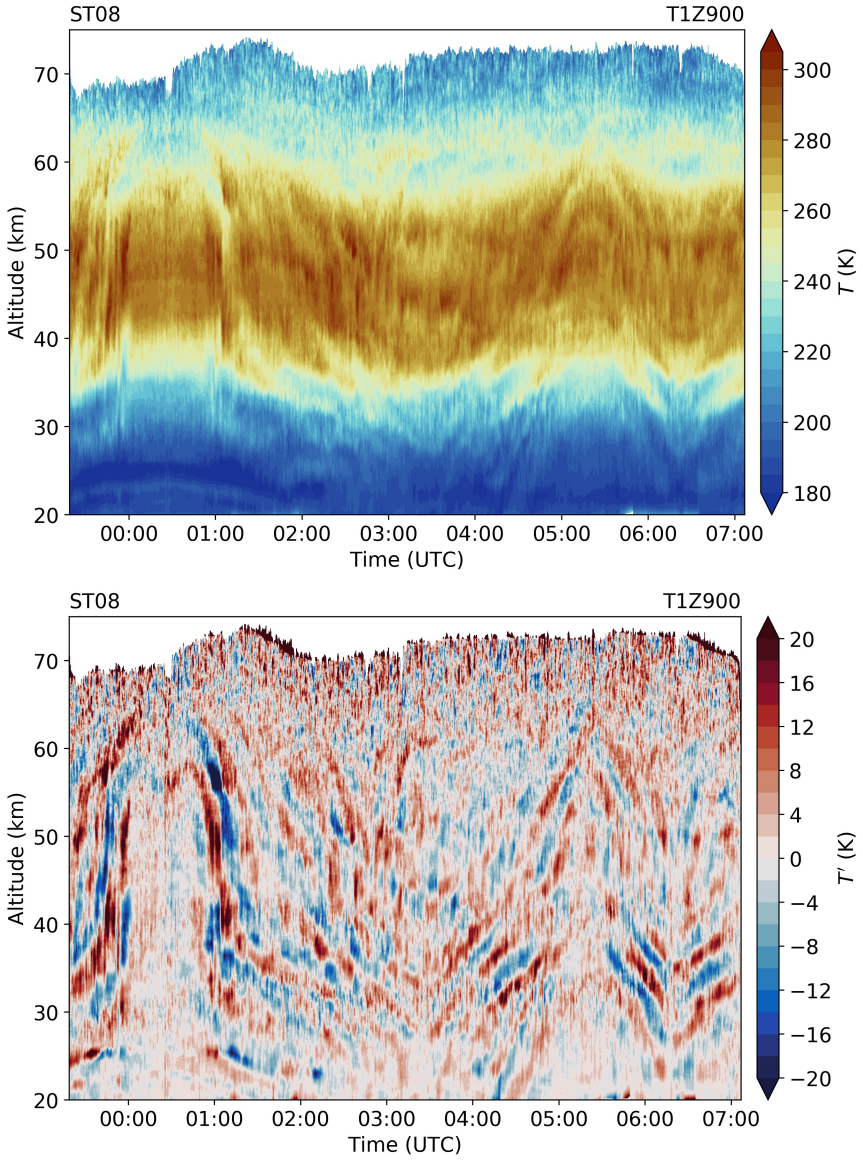

Figure A.1.: Timeseries of (top) temperature and (bottom) temperature perturbation along the flight track of research flight ST08. Retrieved temperatures are of resolution T1Z900. Perturbations are derived by the subtraction of a 30 min running mean from the full temperature.

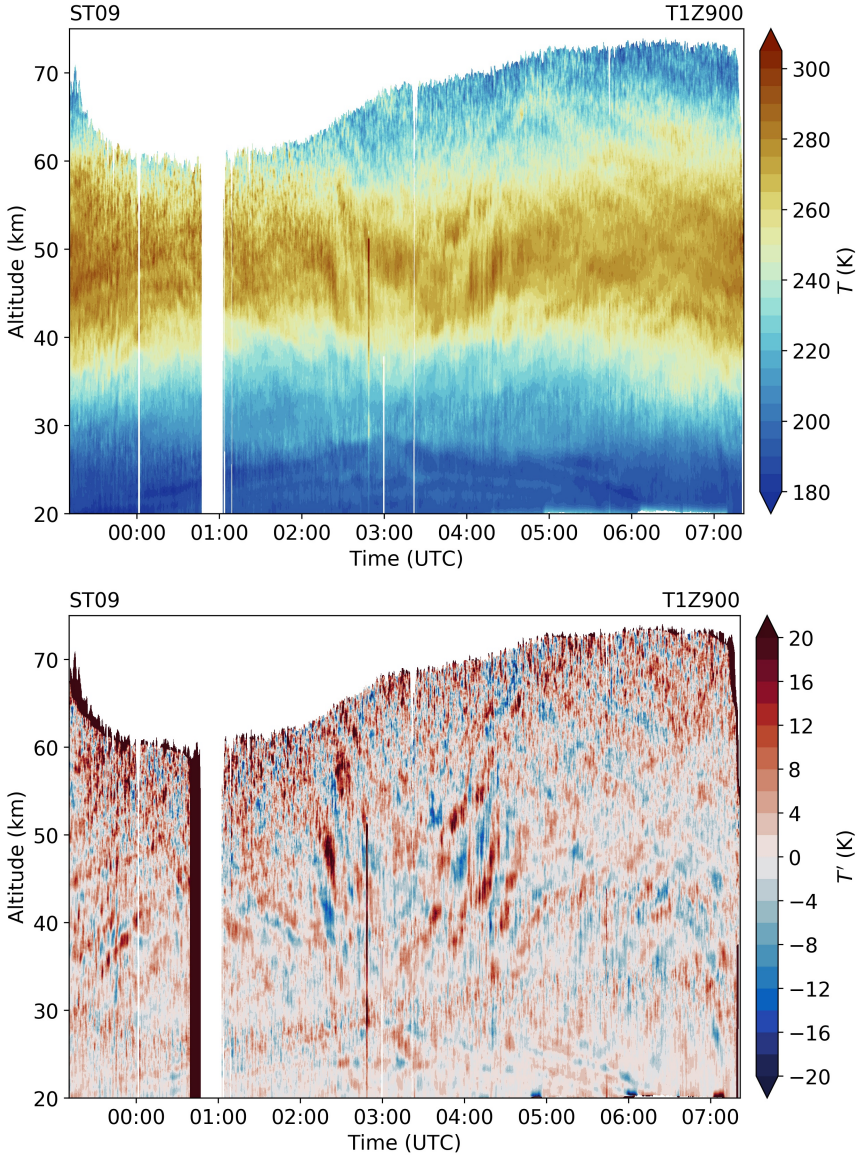

Figure A.2.: Same like Figure A.1 but for flight ST09.

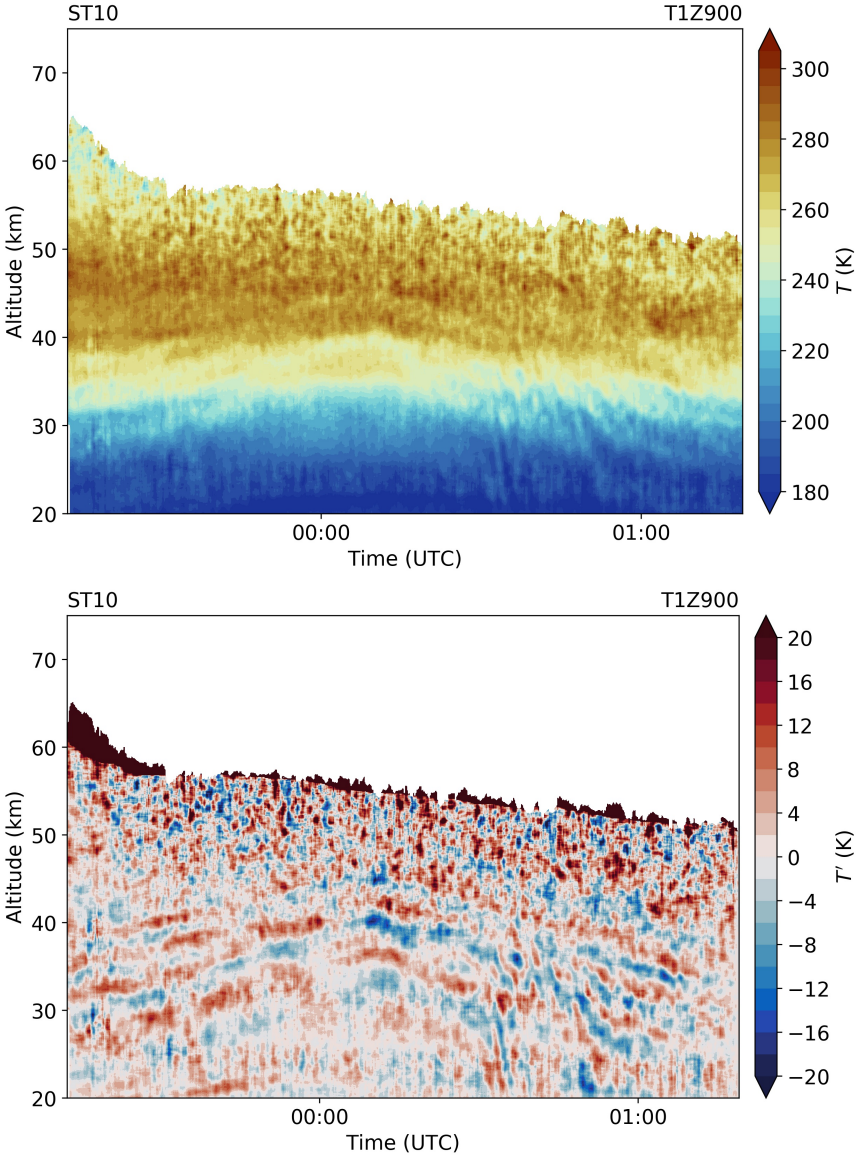

Figure A.3.: Same like Figure A.1 but for flight ST10.

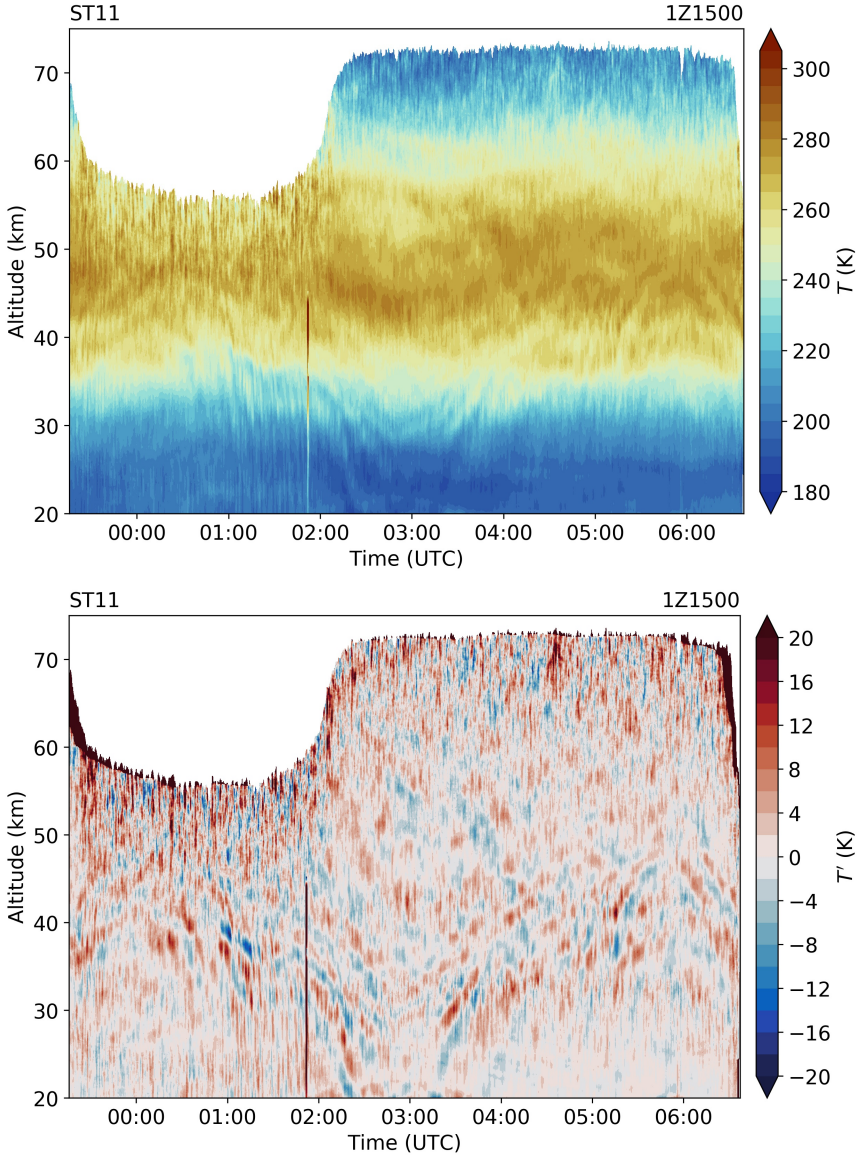

Figure A.4.: Same like Figure A.1 but for flight ST11 and with the resolution T1Z1500.

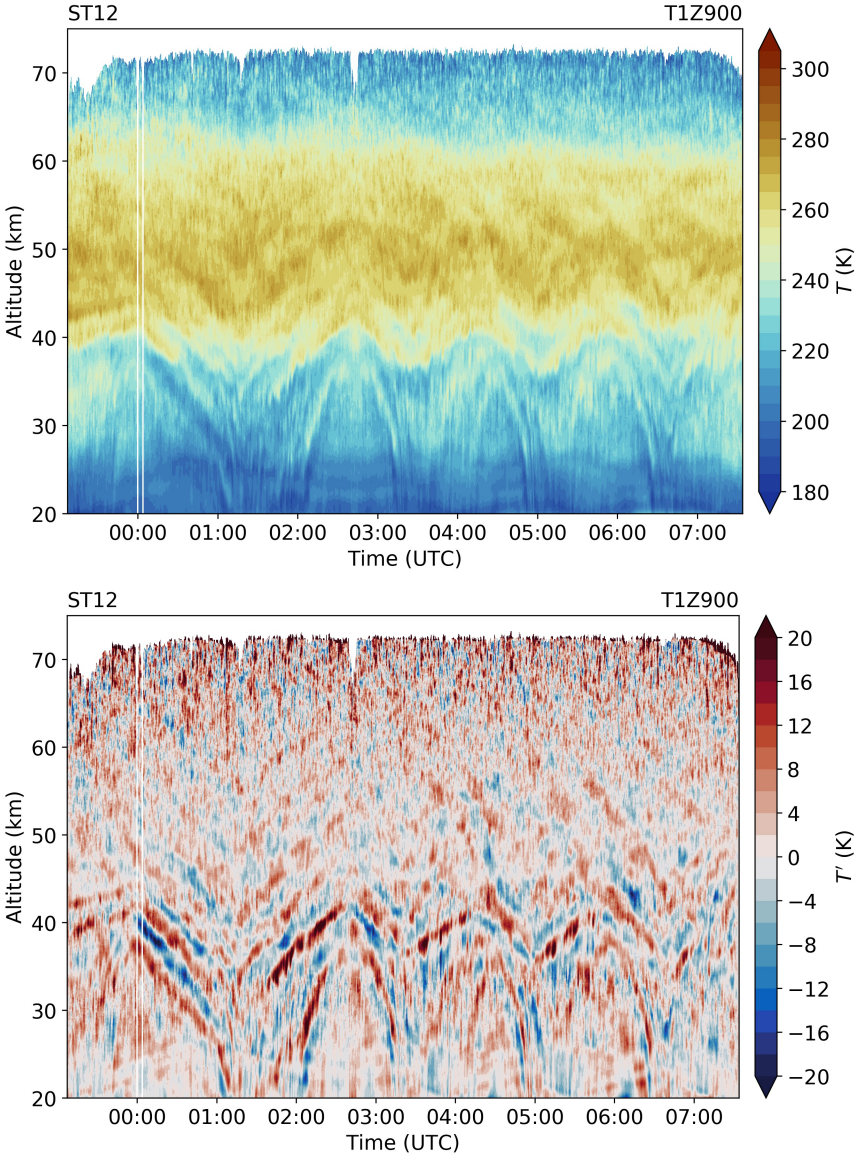

Figure A.5.: Same like Figure A.1 but for flight ST12.

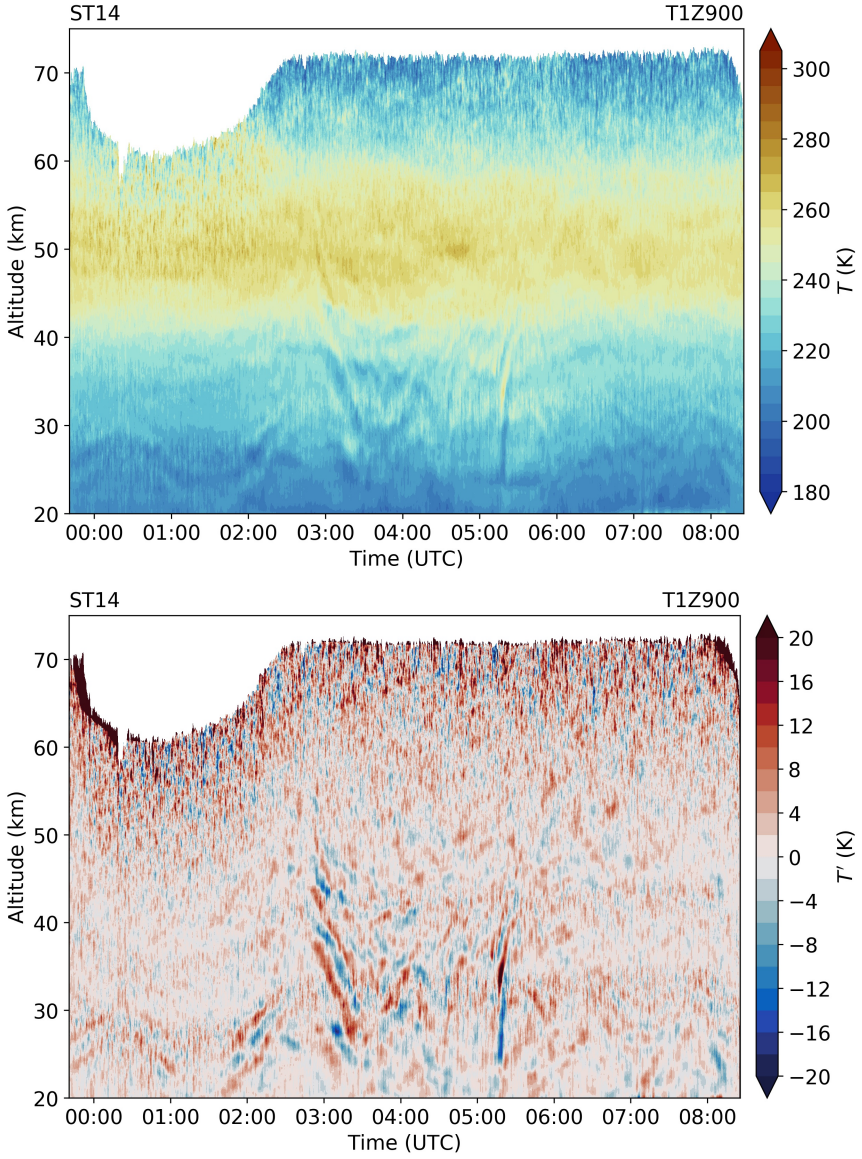

Figure A.6.: Same like Figure A.1 but for flight ST14.

B. Flight leg characteristics

Table B.1.: Characteristics of the selected flight legs from the six research flights of SouthTRAC–GW as used in Chapter 5.

Flight	Leg	Start	End	Duration (min)	Mean distance (km)	True distance (km)
ST08	1	-52.45°N, -69.24°E	-49.70°N, -74.51°E	38	480.00	478.39
	2	-49.44°N, -74.96°E	-47.95°N, -77.38°E	18	244.00	242.87
	3	-48.17°N, -77.05°E	-59.69°N, -51.78°E	132	2080.00	2070.66
	4	-58.90°N, -51.50°E	-57.47°N, -51.93°E	13	162.00	160.99
	5	-56.93°N, -52.08°E	-54.95°N, -52.62°E	17	223.00	222.72
	6	-54.94°N, -54.07°E	-55.62°N, -72.59°E	100	1179.00	1171.86
ST09	1	-51.51°N, -72.79°E	-50.65°N, -75.29°E	16	200.00	199.09
	2	-50.41°N, -75.94°E	-49.08°N, -79.31°E	22	285.00	283.69
	3	-48.70°N, -79.34°E	-46.50°N, -78.27°E	18	258.00	257.44
	4	-43.49°N, -76.91°E	-42.08°N, -76.36°E	10	150.00	150.29
	5	-41.96°N, -76.26°E	-40.63°N, -75.73°E	11	155.00	154.37
	6	-37.52°N, -74.38°E	-37.37°N, -63.17°E	62	994.00	989.19
	7	-37.63°N, -62.90°E	-39.51°N, -62.10°E	14	220.00	220.86
	8	-39.89°N, -62.43°E	-40.01°N, -75.15°E	88	1089.00	1083.45

(To be continued)

Flight	Leg	Start	End	Duration (min)	Mean distance (km)	True distance (km)
	9	-40.38°N, -75.64°E	-45.88°N, -77.98°E	46	641.00	640.29
	10	-46.08°N, -78.08°E	-47.80°N, -78.89°E	15	202.00	201.13
	11	-48.94°N, -79.48°E	-51.59°N, -80.96°E	23	313.00	312.63
	12	-52.04°N, -80.79°E	-53.07°N, -74.54°E	28	441.00	437.63
ST10	1	-51.34°N, -76.98°E	-36.94°N, -54.67°E	143	2423.00	2414.74
	2	-37.56°N, -54.67°E	-41.93°N, -60.09°E	57	673.00	671.17
ST11	1	-43.48°N, -63.81°E	-40.24°N, -60.74°E	28	442.00	440.87
	2	-39.99°N, -60.14°E	-42.94°N, -58.27°E	23	363.00	363.13
	3	-44.07°N, -58.30°E	-56.40°N, -72.12°E	132	1686.00	1680.24
ST12	1	-51.78°N, -71.67°E	-50.11°N, -76.12°E	27	364.00	362.79
	2	-49.11°N, -76.19°E	-44.33°N, -75.52°E	34	535.00	533.95
	3	-44.18°N, -74.95°E	-44.18°N, -68.05°E	33	553.00	550.07
	4	-44.86°N, -68.40°E	-50.67°N, -77.68°E	75	950.00	946.56
	5	-49.76°N, -76.13°E	-48.21°N, -74.66°E	12	205.00	204.88
	6	-48.17°N, -74.49°E	-48.17°N, -71.56°E	13	219.00	217.27
	7	-48.37°N, -71.16°E	-49.76°N, -69.90°E	12	181.00	179.76
	8	-50.13°N, -69.77°E	-51.67°N, -71.02°E	15	192.00	192.37
	9	-51.84°N, -71.51°E	-51.83°N, -74.65°E	17	217.00	215.75
	10	-49.91°N, -76.24°E	-48.15°N, -74.72°E	13	216.00	215.23

(To be continued)

Flight	Leg	Start	End	Duration (min)	Mean distance (km)	True distance (km)
	11	-48.17°N, -74.39°E	-48.18°N, -71.47°E	13	218.00	216.51
	12	-48.31°N, -71.21°E	-49.80°N, -69.86°E	13	193.00	192.68
	13	-50.18°N, -69.82°E	-51.72°N, -71.07°E	15	194.00	192.32
	14	-51.83°N, -71.30°E	-51.82°N, -74.72°E	18	237.00	235.02
	15	-49.39°N, -75.23°E	-47.18°N, -71.66°E	22	363.00	360.71
	16	-47.49°N, -71.27°E	-51.35°N, -69.31°E	32	453.00	451.98
ST14	1	-53.27°N, -58.33°E	-60.00°N, -65.48°E	67	870.00	864.63
	2	-60.46°N, -65.19°E	-60.95°N, -46.91°E	60	1013.00	1007.08
	3	-64.86°N, -51.22°E	-65.18°N, -67.39°E	65	762.00	758.06
	4	-64.76°N, -68.39°E	-54.60°N, -66.03°E	78	1142	1137.28

C. Considerations for the horizontal wavenumber spectra

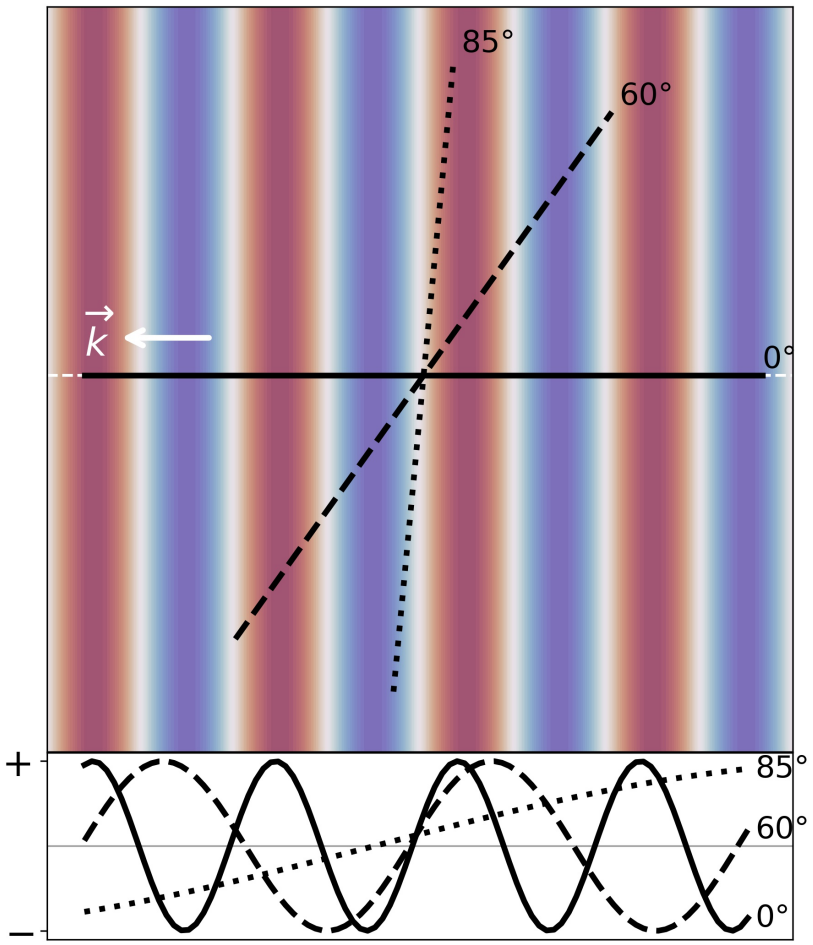

Figure C.1.: Sampled wave amplitudes of a given two-dimensional wave field for different sampling angles or flight legs orientations of 0°, 60° and 85°.

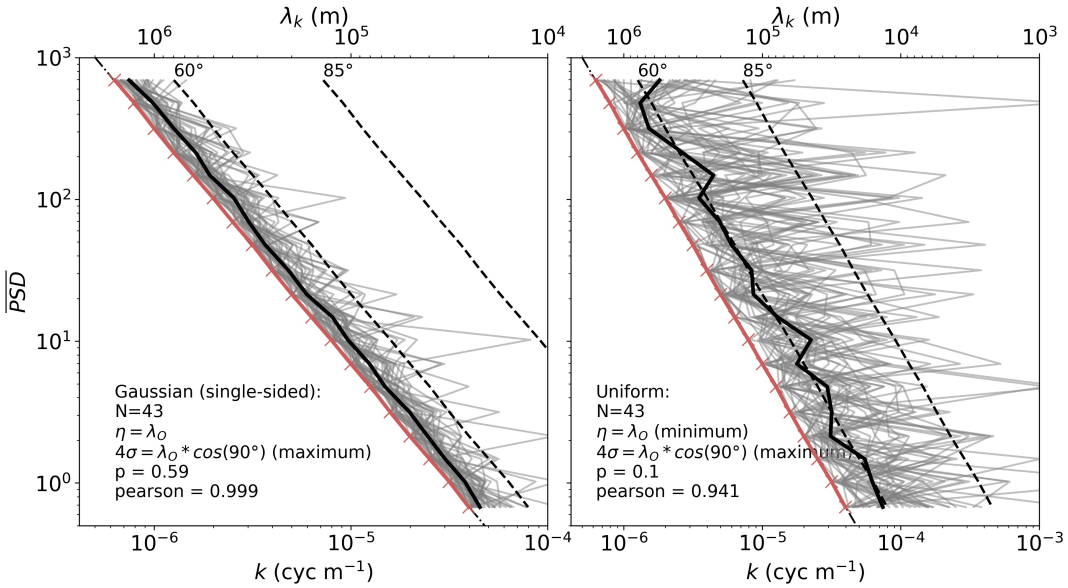

Figure C.2.: Monte-Carlo experiment of N=43 samples for a maximum deviation of 90° between a flight leg and the wave vector following (left) a Gaussian distribution with an expected value of 0° and (right) a Uniform distribution. Red line shows the given spectra, grey lines show the randomly perturbed horizontal wavenumber spectra and the black curve shows the averaged perturbed horizontal wavenumber spectrum.

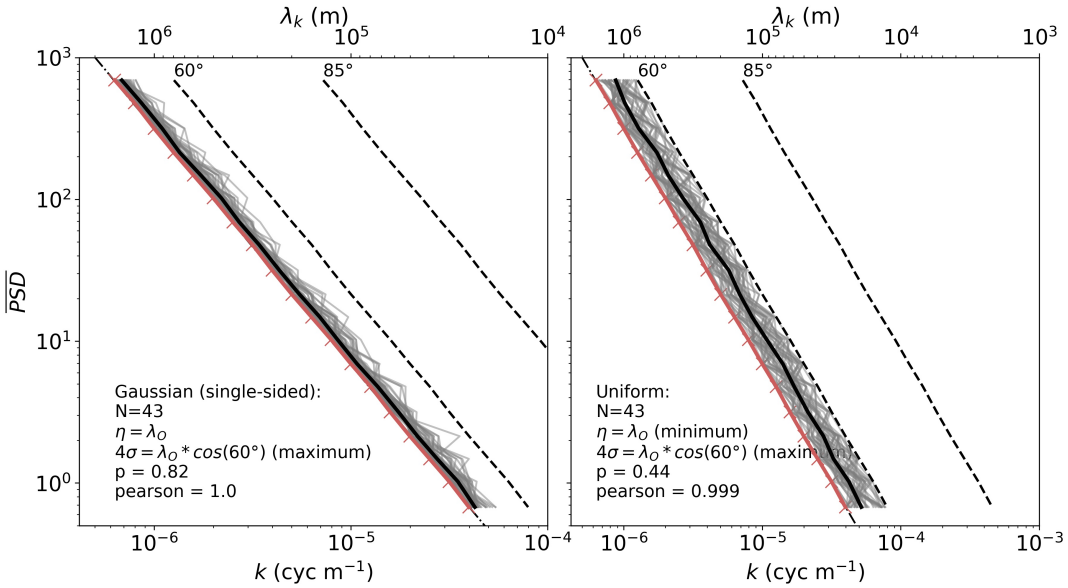

Figure C.3.: Same as Figure C.2 but for a maximum deviation of 60° between a flight leg and the wave vector.

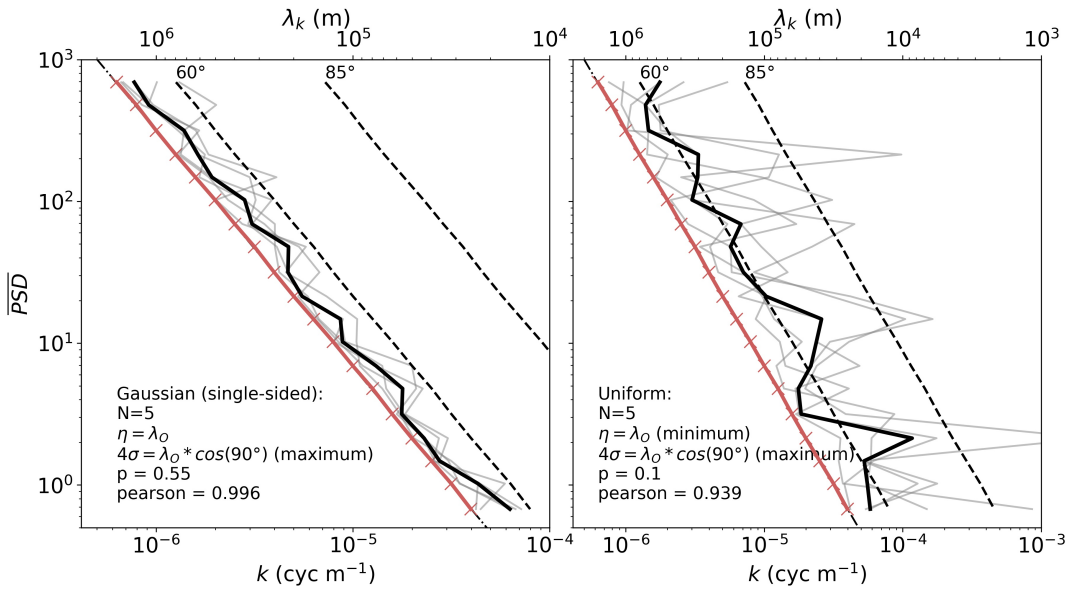

Figure C.4.: Same as Figure C.2 but for $N = 5$.

D. Vertical wavenumber spectra

The vertical wavenumber spectra shown in Figures D.1 and D.2 are derived with a similar method as presented in Section 5.2. The vertical wavenumber spectra are calculated for every time step of the 43 selected flight legs between 20 km to 30 km. Afterwards, the vertical spectra are averaged for each flight leg and research flight.

An applied vertical LOWESS filter with a filter width of 900 m diminishes the spectra energy for $\lambda_z < 1$ km, that means the same range of vertical scales for which the signal already approaches the noise floor.

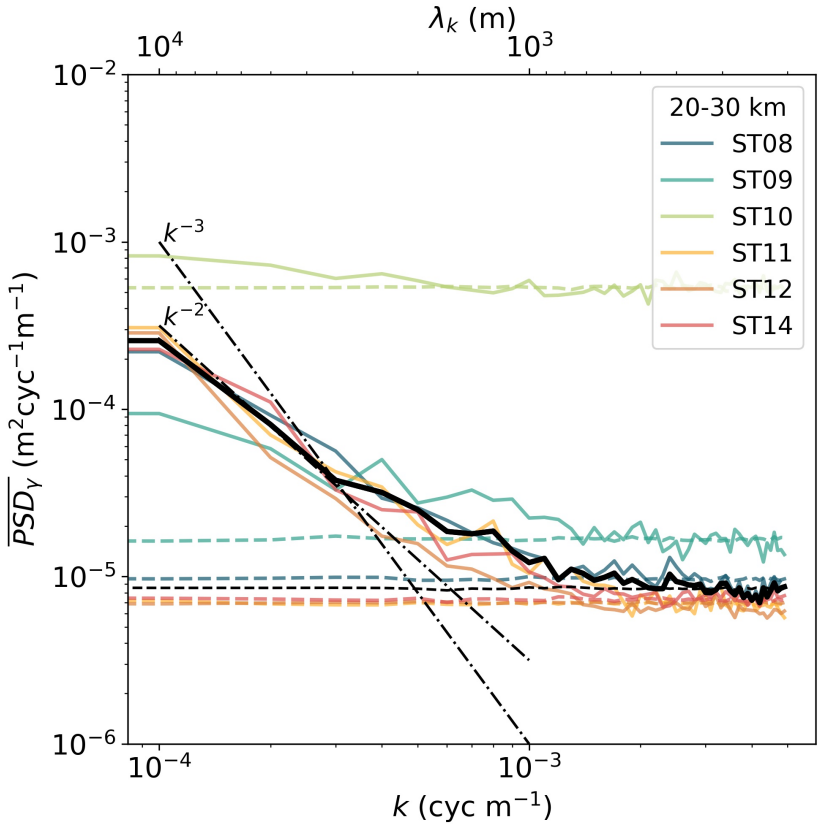

Figure D.1.: Vertical wavenumber spectra between 20 km to 30 km without a vertical filter applied.

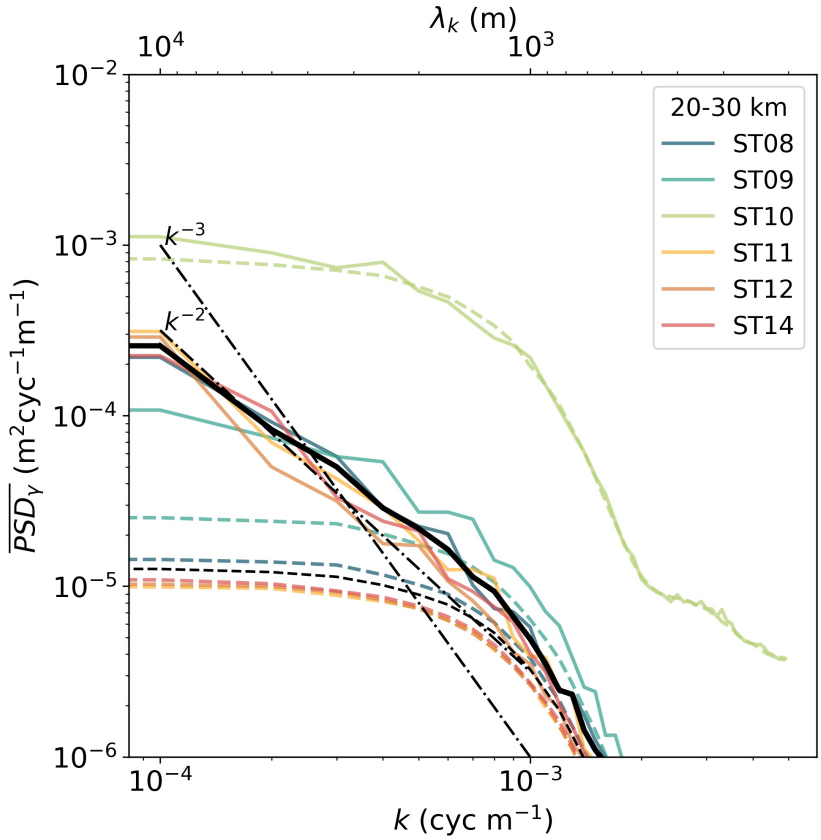

Figure D.2.: Vertical wavenumber spectra between 20 km to 30 km with a vertical filter of 900 m width applied.

E. EULAG simulations

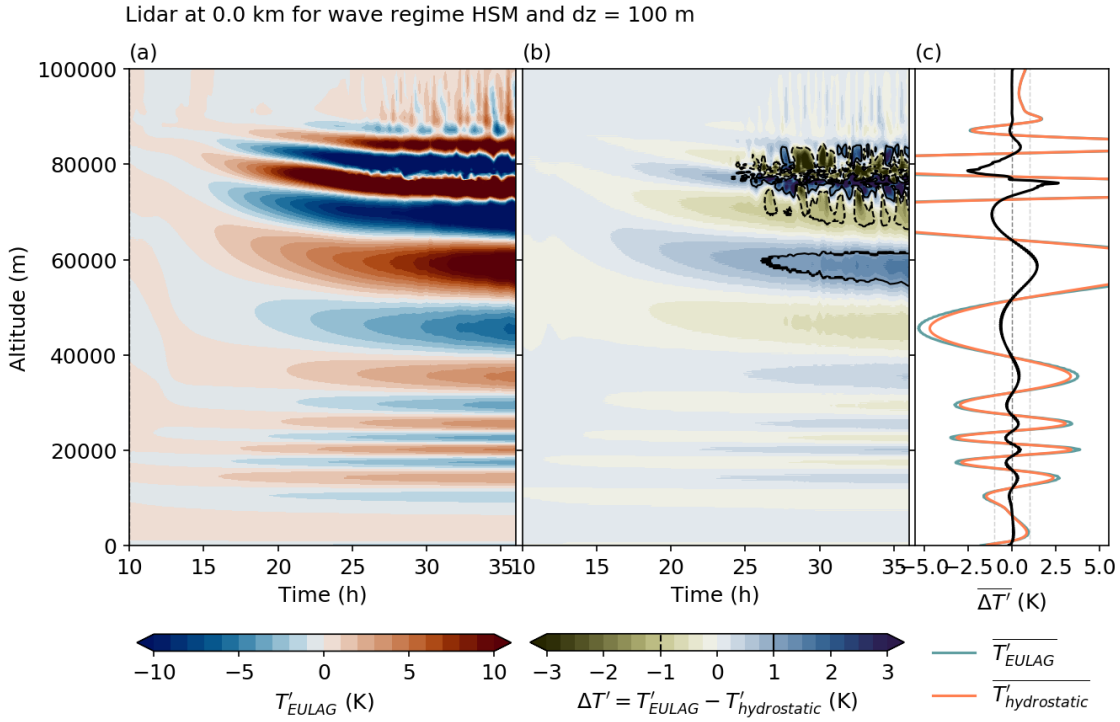

Figure E.1.: Vertical timeseries of (a) T', (b) $\Delta T'$, and (c) the temporal average $\overline{\Delta T'}$ over the displayed 26 h simulation time from the HSM simulation above the mountain. Note that small perturbations around 80 km are caused by generated wave breaking of the model; this nonlinear behavior is excluded from the analysis in Chapter 3.4.

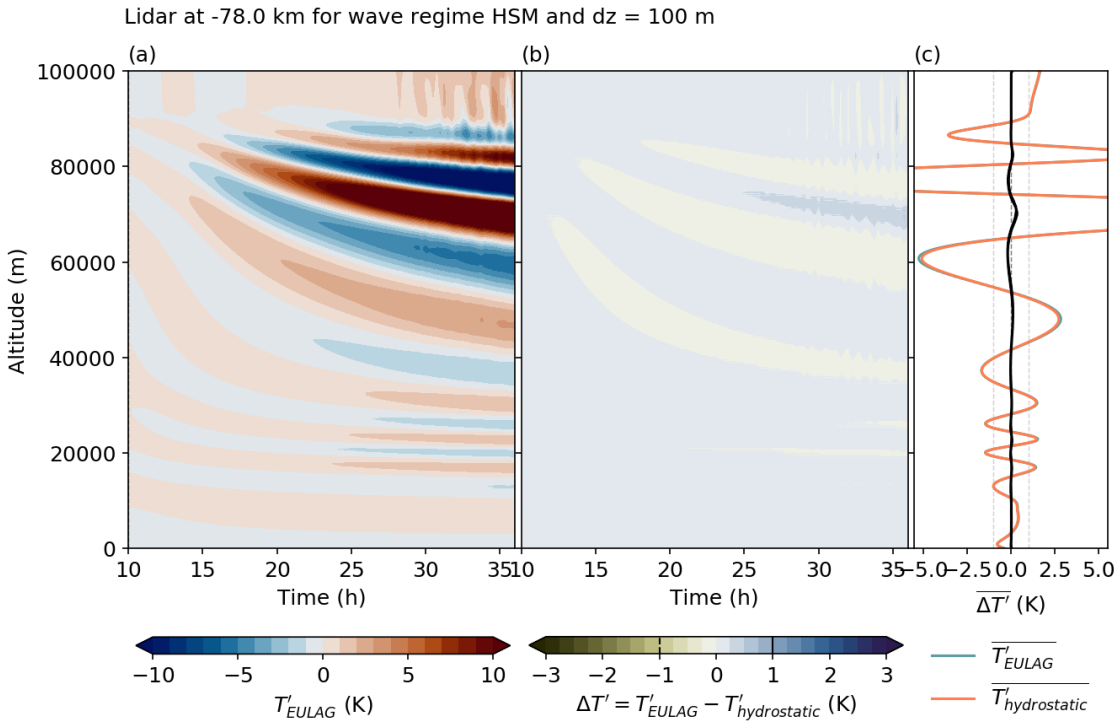

Figure E.2.: Same as Figure E.1 but for the SHM simulation upstream the mountain.

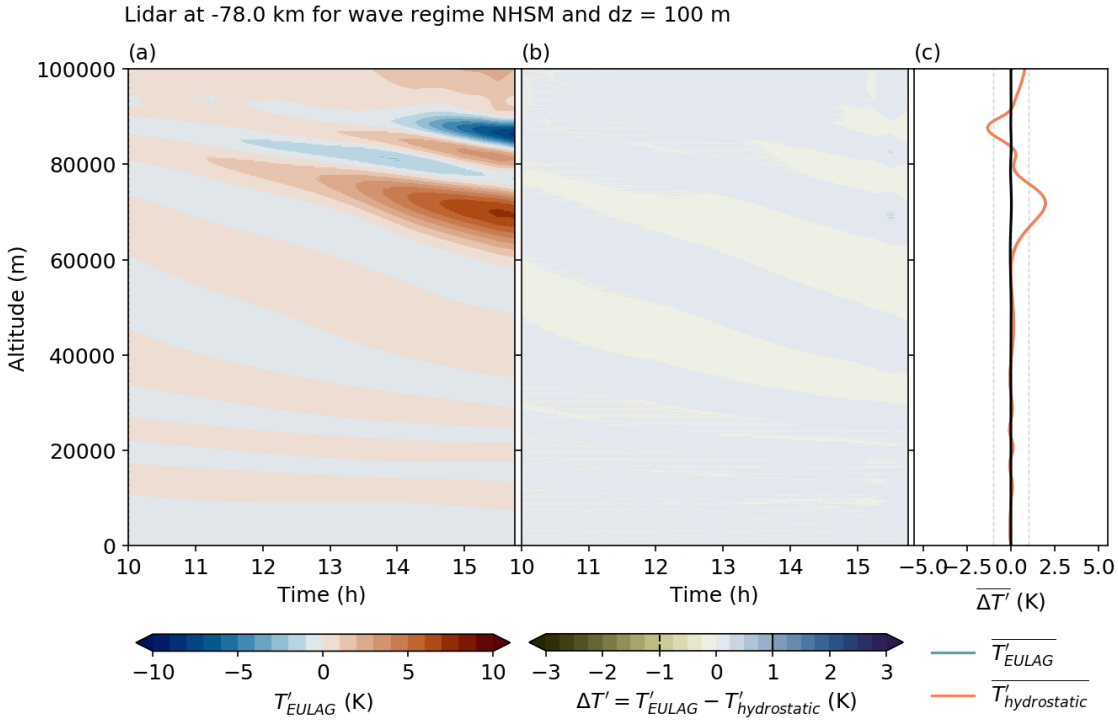

Figure E.3.: Same as Figure E.1 but for the NSHM simulation upstream the mountain.

F. Wavelet analysis

The wavelet analysis is a signal processing tool to estimate the frequency spectrum of a measurement series (Torrence and Compo, 1998). A time series can be decomposed into a time-frequency space by using the Continous Wavelet Transform (CWT) which convolves the signal with a set of wavelets. A wavelet is a wave-like oscillation with the two properties scale s and location $n = 0 \dots N-1$, which are related to frequency and the position in time, respectively. For the CWT in this study, the Morlet wavelet is used as mother wavelet, which is composed of a plane wave modulated by a Gaussian:

$$\psi_0(\eta) = \pi^{-1\backslash 4} e^{i\omega_0 \eta} e^{\eta^2 \backslash 2} \tag{F.1}$$

where η is the nondimensional time parameter and ω_0 is the nondimensional frequency. The integral over the wavelet function has to be zero to fulfill the admissibility condition which can be granted by choosing an appropriate ω_0. Performing the convolution of the CWT for N times, the wavelet transform is given as:

$$W_n(s) = \sum_{k=0}^{N-1} \hat{x}_k \hat{\psi}^*(s\omega_k) e^{i\omega_k n \delta t} \tag{F.2}$$

where $\hat{x}_k$ and $\hat{\psi}^*$ are the discrete Fourier transforms of the signal series x_n and the mother wavelet, $(^*)$ indicates the complex conjugate and δt is the time step. The used set of s is determined as:

$$s_j = s_0 2^{j\delta j}, \quad j = 0, 1, \dots, J = \delta j^{-1} \log_2(\frac{N\delta t}{s_0}) \tag{F.3}$$

Generally, for each s_j, the wavelet is translated along the time series of the signal and the product of wavelet and signal is returned as coefficient displaying spectral amplitudes.

The one-dimensional wavelet transform can also be used to decompose a vertical profile into an altitude-frequency space, where the time domain is replaced by a space domain ($\delta t \Rightarrow \delta z$).

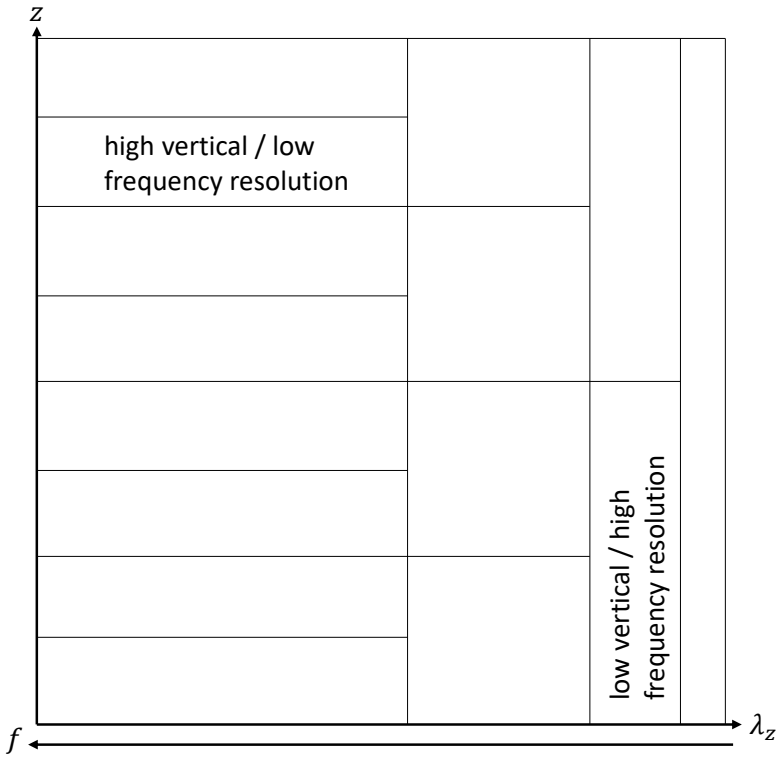

Figure F.1.: Schematic of space-frequency domain of the wavelet transform.

List of Figures

List of Tables

List of Symbols

Symbol	Description	Unit
A	Telescope area	m^2
a	Mountain half-width	m
ab	Placeholder variable	
C	Lidar system parameters	
c	Velocity of light	$m\ s^{-1}$
c_I	Intrinsic phase speed	$m\ s^{-1}$
c_k	Horizontal phase speed	$m\ s^{-1}$
c_p	Heat capacity of dry air	$J\ kg^{-1}\ K^{-1}$
d	Telescope diameter	m
E	Laser pulse energy	mJ
$E(k)$	Spectral energy	
E_p	Gravity wave potential energy density	$J\ m^{-3}$
$\vec{\boldsymbol{F}}$	Frictional forces	$kg\ m\ s^{-2}$
$\vec{F_P}$	Pressure gradient forces	$kg\ m^{-2}\ m^{-2}$
$\vec{F_G}$	Gravity forces	$kg\ m\ s^{-2}$
f	Coriolis parameter	s^{-1}
f_{rep}	Laser pulse repetition frequency	s^{-1}
GS_{HALO}	Ground speed of HALO	$m\ s^{-1}$
g	gravitational acceleration	$m\ s^{-2}$
H	Scale height	m
h	Plank constant	J s
h_0	Mountain height	m
k	Horizontal wavenumber	m^{-1}
k_B	Boltzman constant	$J\ K^{-1}$
k	Array of n	
l	Scorer parameter	m^{-1}
M	Mean molecular mass	
MWA	Mountain wave activity	days
m	Vertical wavenumber	m^{-1}
N	Brunt-Väisälä frequency	s^{-1}
N_{aer}	Number density of aerosols	m^{-3}
N_{air}	Number density of air	m^{-3}
N_{mol}	Number density of molecules	m^{-3}
N_{O_3}	Number density of O_3	m^{-3}

Symbol	Description	Unit
N_2	Nitrogen	
n	Number of grid points of a flight leg	
O_3	Ozone	
P_{BG}	Background photons	
P_L	Photons of laser pulse	
P_R	Backscattered photons	
$P_{R,BGC}$	Background-corrected backscattered photons	
$P_{R,DTC}$	Dead-Time-corrected backscattered photons	
$P_{R,RC}$	Range-corrected backscattered photons	
$P_{R,REC}$	Rayleigh-Extinction-corrected backscattered photons	
ΔP_R	Backscattered photons error	
PSD_γ	Power spectral density of photon counts	
p	Pressure	Pa
p_0	Reference Pressure	Pa
$\dot{Q}$	Diabatic heating	
R_d	Gas constant of dry air	J K^{-1} mol^{-1}
SNR Signal-to-Noise Ratio		
t	Time	s
Δt	Temporal resolution	s
dt	Integration period	s
T	Temperature	K
$T_{hydrostatic}$	Hydrostatically derived temperature	K
$T'_{hydrostatic}$	Hydrostatically derived temperature perturbation	K
T_{EULAG}	EULAG temperature	K
T'_{EULAG}	EULAG temperature perturbation	K
T_0	Initialization temperature	K
T'	Temperature perturbation	K
ΔT	Temperature error	K
$\Delta T'$	Temperature perturbation error	K
U_H	Horizontal wind velocity	m s^{-1}
$U_{H,up}$	Upstream horizontal wind velocity	m s^{-1}
U_*	Horizontal wind velocity threshold	m s^{-1}
$\vec{\boldsymbol{u}}$	Three-dimensional velocity vector	m s^{-1}
u	Zonal velocity component	m s^{-1}
$\overline{u}$	Background zonal velocity component	m s^{-1}
v	Meridional velocity component	m s^{-1}
W_z	One-dimensional wavelet sepctra	
w	Vertical velocity component	m s^{-1}
$\overline{w}$	Background vertical velocity component	m s^{-1}

Symbol	Description	Unit
w'	Perturbation vertical velocity component	m s^{-1}
w_k	Vertical velocity component of k^{th} wave mode	m s^{-1}
X	Length of flight leg	m
x	x dimension	
Δx	Horizontal bin size	m
$\Delta x'$	Primary horizontal resolution	m
y	y dimension	
z	Altitude (vertical direction)	m
z_L	Lidar altitude	m
z_c	Critical level	m
z_0	Initialization altitude	m
Δz	Range	m
$\mathrm{d}z$	Vertical resolution	m
α	Wave vector orientation	$^\circ$
$\alpha_{H,up}$	Upstream wind direction	$^\circ$
α_{SA}	Southern Andes wind direction	$^\circ$
α_*	Wind direction threshold	$^\circ$
β	Backscatter coefficient	
β_{mol}	Molecular backscatter coefficient	
β_{aer}	Paticulate backscatter coefficient	
γ	Corrected photon counts	
$\overline{\gamma}$	Corrected photon count background	
γ'	Corrected photon count perturbations	
ϵ	Energy dissipation rate	
η_{FOV}	FOV efficiency	
η_{trans}	Transmission efficiency	
κ	Poisson constant	
π	Pi	
ρ	Air density	kg m^{-3}
ρ_0	Initialization air density	kg m^{-3}
θ	Potential temperature	K
$\overline{\theta}$	Background potential temperature	K
λ	Wavelength	m
λ_k	Horizontal wavelength	m
λ_{k}	Horizontal wavelength of k	m
λ_z	Vertical wavelength	m
λ_{PD}	Expected value of a Poisson distribution	
σ	Standard deviation	
σ_{aer}	Particulate backscattering cross section	m^{-2}
σ_{mol}	Molecular backscattering cross section	m^{-2}
$\sigma_{mol,tot}$	Total molecular scattering cross section	m^{-2}
$\sigma_{\mathrm{O_3}}$	O_3 scattering cross section	m^{-2}

Symbol	Description	Unit
τ	Temporal spacing	s
τ_D	Dead time of detectors	s
τ_p	Laser pulse duration	s
τ_{Ray}	Rayleigh extinction	
$\tau_{Ray,REC}$	Rayleigh extinction correction parameter	
τ_{O_3}	O_3 absorption	
Ω	Intrinsic frequency	s^{-1}
$\mathbf{\Omega}$	Earth's rotation vector	
$\Delta\Omega$	Solid angle	
ω	Apparent frequency	s^{-1}
ω_0	nondimensional frequency	

Abbreviations

ALIMA	Airborne Lidar for Middle Atmosphere research. 3–5, 27, 28, 30, 31, 33–36, 41–43, 59–61, 65, 66, 68, 75–79, 82, 88–93
ALOMAR	Arctic Lidar for Middle Atmosphere Research. 21, 45
APD	Avalanche Photodiodes. 24, 28, 32
BAHAMAS	Basic HALO Measurement and Sensor System. 68, 69
BDC	Brewer-Dobson-Circulation. 2, 4, 13
BOLIDE	Balloon Lidar Experiment. 45
CORAL	COmpact Rayleigh Autonomous Lidar. 21, 45
CWT	Continous Wavelet Transform. 113
DEEPWAVE	Deep Propagation. 45
DLR	Deutsches Zentrum für Luft- und Raumfahrt. 27, 68
ECMWF	European Center for Medium-range Weather Forecast. 69
ENSO	El Nino-Southern Oscillation. 13
EOS	Earth Observing System. 36
ERA5	ECMWF Reanalysis v5. 34–38, 64–66, 79, 91
EULAG	EUlerian/semi- LAGrangian fluid solver. 47–49, 91
FFT	Fast Fourier Transform. 83
FOV	Field Of View. 23, 30
GASP	Global Atmospheric Sampling Program. 14
GLORIA	Gimballed Limb Observer for Radiance Imaging of the Atmosphere. 68, 69
GW	Gravity Waves. 2–5, 8–11, 13, 16, 17, 26, 34, 44, 46, 48, 49, 54, 55, 57–61, 64, 66, 68–70, 75–83, 86, 88–93
HALO	High Altitude and Long Range. 27, 42, 68, 69, 82
HSM	Hydrostatic Mountain. 47–57

IFS	Integrated Forecasting System. 69
LOWESS	Locally Weighted Scatterplot Smoothing. 83, 109
LTA	Lidar Température et Aérosols. 21, 45
MLS	Microwave Limb Souder. 36, 40, 41
MLT	Mesosphere Lower Thermosphere. 3, 67, 68
MST	Mesospheric Stratospheric and Tropospheric. 2
MW	Mountain Waves. 2–5, 8, 10–13, 21, 46–51, 56, 58–60, 63–65, 68, 71, 73, 75, 76, 78, 80–82, 88–92
MWA	Mountain Wave Activity. 64, 65, 73–75, 79, 92
NaN	Not a Number. 30
NAO	North Atlantic Oscillation. 13
Nd:YAG	Neodymium-Doped Yttrium Aluminum Garnet. 21, 27
NH	Northern Hemisphere. 10, 11, 78–80
NHSM	Non-Hydrostatic Mountain. 47–58
NWP	Numerical Weather Prediction. 1, 2, 4, 68, 81
OEM	Optimal Estimation Method. 45, 46
PCL	Purple Crow Lidar. 21, 45
PFJ	Polar Front Jet. 63, 67, 71–73, 75, 79, 92
PMCs	Polar Mesospheric Clouds. 25, 68
PMT	Photomultiplier Tube. 28, 30, 32
PNJ	Polar Night Jet. 4, 48, 52, 66–68, 70, 71, 75–79, 88
PSCs	Polar Stratospheric Clouds. 25, 67
PSD	Power Spectral Density. 83
QBO	Quasi-Biennial Oscillation. 2, 4, 67
RMR	Rayleigh-Mie-Raman. 21, 45
RMSE	Root Mean Square Error. 43
SABER	Sounding of the Atmosphere using Broadband Emission Radiometry. 33, 34
SAM	Southern Annular Mode. 67, 75, 79, 92
SH	Southern Hemisphere. 4, 63, 64, 66–69, 78–80, 92
SNR	Signal-to-Noise Ratio. 23–25, 28, 33, 34, 37, 43, 83
SouthTRAC-GW	Southern Hemisphere Transport, Dynamics, and Chemistry – Gravity Waves. 3–5, 27, 34, 60, 64, 65, 68, 69, 78–80, 82, 83, 88–93

SPV	Stratospheric Polar Vortex. 4, 65–68, 71, 75, 76, 78, 80, 88, 90, 92, 93
SSW	Sudden Stratospheric Warming. 4, 5, 64, 66–69, 71, 75, 78–80, 82, 85, 88–90, 92, 93
STJ	Subtropical Jet. 63, 71, 72
TELMA	Temperature Lidar for Middle Atmosphere research. 45
TIMED	Thermosphere Ionosphere Mesosphere Energetics Dynamics. 33
UTLS	Upper Troposphere Lower Stratosphere. 67, 68
WN1	Wavenumber 1. 66

Bibliography

Alexander, M. J. (1998). "Interpretations of observed climatological patterns in stratospheric gravity wave variance". In: *Journal of Geophysical Research: Atmospheres* 103.D8, pp. 8627–8640. DOI: https://doi.org/10.1029/97JD03325.

Alexander, S. P., A. R. Klekociuk, and D. J. Murphy (2011). "Rayleigh lidar observations of gravity wave activity in the winter upper stratosphere and lower mesosphere above Davis, Antarctica (69°S, 78°E)". In: *Journal of Geophysical Research: Atmospheres* 116.D13. DOI: https://doi.org/10.1029/2010JD015164.

Alpers, M., R. Eixmann, C. Fricke-Begemann, M. Gerding, and J. Höffner (2004). "Temperature lidar measurements from 1 to 105 km altitude using resonance, Rayleigh, and Rotational Raman scattering". In: *Atmospheric Chemistry and Physics* 4.3, pp. 793–800. DOI: 10.5194/acp-4-793-2004.

Avsarkisov, V., E. Becker, and T. Renkwitz (2022). "Turbulent Parameters in the Middle Atmosphere: Theoretical Estimates Deduced from a Gravity Wave–Resolving General Circulation Model". In: *Journal of the Atmospheric Sciences* 79.4, pp. 933–952. DOI: 10.1175/JAS-D-21-0005.1.

Bacmeister, J. T., S. D. Eckermann, P. A. Newman, L. Lait, K. R. Chan, M. Loewenstein, M. H. Proffitt, and B. L. Gary (1996). "Stratospheric horizontal wavenumber spectra of winds, potential temperature, and atmospheric tracers observed by high-altitude aircraft". In: *Journal of Geophysical Research: Atmospheres* 101.D5, pp. 9441–9470. DOI: https://doi.org/10.1029/95JD03835.

Baldwin, M. P., B. Ayarzagüena, T. Birner, N. Butchart, A. H. Butler, A. J. Charlton-Perez, D. I. V. Domeisen, C. I. Garfinkel, H. Garny, E. P. Gerber, M. I. Hegglin, U. Langematz, and N. M. Pedatella (2021). "Sudden Stratospheric Warmings". In: *Reviews of Geophysics* 59.1. e2020RG000708 10.1029/2020RG000708, e2020RG000708. DOI: https://doi.org/10.1029/2020RG000708.

Baldwin, M. P., T. Birner, G. Brasseur, J. Burrows, N. Butchart, R. Garcia, M. Geller, L. Gray, K. Hamilton, N. Harnik, M. I. Hegglin, U. Langematz, A. Robock, K. Sato, and A. A. Scaife (2019). "100 Years of Progress in Understanding the Stratosphere and Mesosphere". In: *Meteorological Monographs* 59, pp. 27.1–27.62. DOI: 10.1175/AMSMONOGRAPHS-D-19-0003.1.

Bauer, R., J.-U. Grooß, J. Ungermann, M. Bär, M. Geldenhuys, and L. Hoffmann (2022). "The Mission Support System (MSS v7.0.4) and its use in planning for the SouthTRAC aircraft campaign". In: *Geoscientific Model Development* 15.24, pp. 8983–8997. DOI: 10.5194/gmd-15-8983-2022.

Baumgarten, G. (2010). "Doppler Rayleigh/Mie/Raman lidar for wind and temperature measurements in the middle atmosphere up to 80 km". In: *Atmospheric Measurement Techniques* 3.6, pp. 1509–1518. DOI: 10.5194/amt-3-1509-2010.

Becker, E. (2012). "Dynamical Control of the Middle Atmosphere". In: *Space Science Reviews* 168.1-4, pp. 283–314. DOI: 10.1007/s11214-011-9841-5.

Becker, E., S. L. Vadas, K. Bossert, V. L. Harvey, C. Zülicke, and L. Hoffmann (2022). "A High-Resolution Whole-Atmosphere Model With Resolved Gravity Waves and Specified Large-Scale Dynamics in the Troposphere and Stratosphere". In: *Journal of Geophysical Research: Atmospheres* 127.2. e2021JD035018 2021JD035018, e2021JD035018. DOI: https://doi.org/10.1029/2021JD035018.

Bierdel, L., C. Snyder, S.-H. Park, and W. C. Skamarock (2016). "Accuracy of Rotational and Divergent Kinetic Energy Spectra Diagnosed from Flight-Track Winds". In: *Journal of the Atmospheric Sciences* 73.8, pp. 3273–3286. DOI: https://doi.org/10.1175/JAS-D-16-0040.1.

Bossert, K., C. G. Kruse, C. J. Heale, D. C. Fritts, B. P. Williams, J. B. Snively, P.-D. Pautet, and M. J. Taylor (2017). "Secondary gravity wave generation over New Zealand during the DEEPWAVE campaign". In: *Journal of Geophysical Research: Atmospheres* 122.15, pp. 7834–7850. DOI: https://doi.org/10.1002/2016JD026079.

Bowman, M. R., A. J. Gibson, and M. C. W. Sandford (1969). "Atmospheric sodium measured by a tuned laser radar". In: *Nature* 221.5179, pp. 456–457.

Brasseur, G. P. and S. Solomon (2005). *Aeronomy of the middle atmosphere: Chemistry and physics of the stratosphere and mesosphere*. Vol. 32. Springer Science & Business Media.

Brethouwer, G., P. Billant, E. Lindborg, and J.-M. Chomaz (2007). "Scaling analysis and simulation of strongly stratified turbulent flows". In: *Journal of Fluid Mechanics* 585, pp. 343–368. DOI: 10.1017/S0022112007006854.

Brune, S. and B. Becker (2013). "Indications of Stratified Turbulence in a Mechanistic GCM". In: *Journal of the Atmospheric Sciences* 70, pp. 231–247.

Bucholtz, A. (May 1995). "Rayleigh-scattering calculations for the terrestrial atmosphere". In: *Appl. Opt.* 34.15, pp. 2765–2773. DOI: 10.1364/AO.34.002765.

Burris, J., T. McGee, W. Hoegy, L. Lait, L. Twigg, G. Sumnicht, W. Heaps, C. Hostetler, T. P. Bui, R. Neuber, et al. (2002). "Validation of temperature measurements from the airborne Raman ozone temperature and aerosol lidar during SOLVE". In: *Journal of Geophysical Research: Atmospheres* 107.D20, SOL–29.

Byrne, N. J. and T. G. Shepherd (2018). "Seasonal Persistence of Circulation Anomalies in the Southern Hemisphere Stratosphere and Its Implications for the Troposphere". In: *Journal of Climate* 31.9, pp. 3467–3483. DOI: 10.1175/JCLI-D-17-0557.1.

Charlton, A. J. and L. M. Polvani (2007). "A New Look at Stratospheric Sudden Warmings. Part I: Climatology and Modeling Benchmarks". In: *Journal of Climate* 20.3, pp. 449–469. DOI: https://doi.org/10.1175/JCLI3996.1.

Charney, J. G. (1971). "Geostrophic Turbulence". In: *Journal of Atmospheric Sciences* 28.6, pp. 1087–1095. DOI: 10.1175/1520-0469(1971)028<1087:GT>2.0.CO;2.

Cho, J. Y. N. and E. Lindborg (2001). "Horizontal velocity structure functions in the upper troposphere and lower stratosphere: 1. Observations". In: *Journal of Geophysical Research: Atmospheres* 106.D10, pp. 10223–10232. DOI: https://doi.org/10.1029/2000JD900814.

Cho, J. Y. N., R. E. Newell, and J. D. Barrick (1999a). "Horizontal wavenumber spectra of winds, temperature, and trace gases during the Pacific Exploratory Missions: 2. Gravity waves, quasi-two-dimensional turbulence, and vortical modes". In: *Journal of Geophysical Research: Atmospheres* 104.D13, pp. 16297–16308. DOI: https://doi.org/10.1029/1999JD900068.

Cho, J. Y. N., Y. Zhu, R. E. Newell, B. E. Anderson, J. D. Barrick, G. L. Gregory, G. W. Sachse, M. A. Carroll, and G. M. Albercook (1999b). "Horizontal wavenumber spectra of winds, temperature, and trace gases during the Pacific Exploratory Missions: 1. Climatology". In: *Journal of Geophysical Research: Atmospheres* 104.D5, pp. 5697–5716. DOI: https://doi.org/10.1029/98JD01825.

Dewan, E. M. (1979). "Stratospheric Wave Spectra Resembling Turbulence". In: *Science* 204.4395, pp. 832–835. DOI: 10.1126/science.204.4395.832.

– (1994). "The saturated-cascade model for atmospheric gravity wave spectra, and the wavelength-period (W-P) relations". In: *Geophysical Research Letters* 21.9, pp. 817–820. DOI: https://doi.org/10.1029/94GL00702.

– (1997). "Saturated-cascade similitude theory of gravity wave spectra". In: *Journal of Geophysical Research: Atmospheres* 102.D25, pp. 29799–29817. DOI: https://doi.org/10.1029/97JD02151.

Donovan, D. P., J. A. Whiteway, and A. I. Carswell (Nov. 1993). "Correction for nonlinear photon-counting effects in lidar systems". In: *Appl. Opt.* 32.33, pp. 6742–6753. DOI: 10.1364/AO.32.006742.

Dörnbrack, A., P. Bechtold, and U. Schumann (2022). "High-Resolution Aircraft Observations of Turbulence and Waves in the Free Atmosphere and Comparison With Global Model Predictions". In: *Journal of Geophysical Research: Atmospheres* 127.16, e2022JD036654. DOI: https://doi.org/10.1029/2022JD036654.

Dörnbrack, A., S. Gisinger, and B. Kaifler (2017). "On the Interpretation of Gravity Wave Measurements by Ground-Based Lidars". In: *Atmosphere* 8.3. DOI: 10.3390/atmos8030049.

Dörnbrack, A., B. Kaifler, N. Kaifler, M. Rapp, N. Wildmann, M. Garhammer, K. Ohlmann, J. M. Payne, M. Sandercock, and E. J. Austin (2020). "Unusual appearance of mother-of-pearl clouds above El Calafate, Argentina". In: *Weather* 75.12, pp. 378–388. DOI: https://doi.org/10.1002/wea.3863.

Dörnbrack, A., M. Leutbecher, J. Reichardt, A. Behrendt, K.-P. Müller, and G. Baumgarten (2001). "Relevance of mountain wave cooling for the formation of polar stratospheric clouds over Scandinavia: Mesoscale dynamics and observations for January 1997". In: *Journal of Geophysical Research: Atmospheres* 106.D2, pp. 1569–1581. DOI: https://doi.org/10.1029/2000JD900194.

Duck, Thomas J., James A. Whiteway, and Allan I. Carswell (1998). "Lidar observations of gravity wave activity and Arctic stratospheric vortex core warming". In: *Geophysical Research Letters* 25.15, pp. 2813–2816. DOI: https://doi.org/10.1029/98GL02113.

– (2001). "The Gravity Wave–Arctic Stratospheric Vortex Interaction". In: *Journal of the Atmospheric Sciences* 58.23, pp. 3581–3596. DOI: 10.1175/1520-0469(2001)058<3581:TGWASV>2.0.CO;2.

Eckermann, S. D., I. Hirota, and W. K. Hocking (1995). "Gravity wave and equatorial wave morphology of the stratosphere derived from long-term rocket soundings". In: *Quarterly Journal of the Royal Meteorological Society* 121.521, pp. 149–186. DOI: https://doi.org/10.1002/qj.49712152108.

Elterman, L. (1953). "A series of stratospheric temperature profiles obtained with the searchlight technique". In: *Journal of Geophysical Research* 58.4, pp. 519–530.

Ern, M., Q. T. Trinh, P. Preusse, J. C. Gille, M. G. Mlynczak, J. M. Russell III, and M. Riese (2018). "GRACILE: a comprehensive climatology of atmospheric gravity wave parameters based on satellite limb soundings". In: *Earth System Science Data* 10.2, pp. 857–892. DOI: 10.5194/essd-10-857-2018.

Eswaraiah, S., J.-H. Kim, W. Lee, J. Hwang, K. N. Kumar, and Y. H. Kim (2020). "Unusual Changes in the Antarctic Middle Atmosphere During the 2019 Warming in the Southern Hemisphere". In: *Geophysical Research Letters* 47.19. e2020GL089199 2020GL089199, e2020GL089199. DOI: https://doi.org/10.1029/2020GL089199.

Evans, W. F. J. and E. J. Llewellyn (1972). "Measurements of Mesospheric Ozone from Observations of the 1.27ν Band". In: *Radio Science* 7.1, pp. 45–50. DOI: https://doi.org/10.1029/RS007i001p00045.

Fiedler, F. and H. A. Panofsky (1970). "Atmospheric scales and spectral gaps". In: *Bulletin of the American Meteorological Society* 51.12, pp. 1114–1120. DOI: https://doi.org/10.1175/1520-0477(1970)051<1114:ASASG>2.0.CO;2.

Fiocco, G. and L. D. Smullin (1963). "Detection of scattering layers in the upper atmosphere (60–140 km) by optical radar". In: *Nature* 199, pp. 1275–1276.

Fogt, R. L. and G. J. Marshall (2020). "The Southern Annular Mode: Variability, trends, and climate impacts across the Southern Hemisphere". In: *WIREs Climate Change* 11.4, e652. DOI: https://doi.org/10.1002/wcc.652.

Fricke, K. H. and U. von Zahn (1985). "Mesopause temperatures derived from probing the hyperfine structure of the D2 resonance line of sodium by lidar". In: *Journal of Atmospheric and Terrestrial Physics* 47.5, pp. 499–512. DOI: https://doi.org/10.1016/0021-9169(85)90116-3.

Friedl-Vallon, F., T. Gulde, F. Hase, A. Kleinert, T. Kulessa, G. Maucher, T. Neubert, F. Olschewski, C. Piesch, P. Preusse, H. Rongen, C. Sartorius, H. Schneider, A. Schönfeld, V. Tan, N. Bayer, J. Blank, R. Dapp, A. Ebersoldt, H. Fischer, F. Graf, T. Guggenmoser, M. Höpfner, M. Kaufmann, E. Kretschmer, T. Latzko, H. Nordmeyer, H. Oelhaf, J. Orphal, M. Riese, G. Schardt, J. Schillings, M. K. Sha, O. Suminska-Ebersoldt, and J. Ungermann (2014). "Instrument concept of the imaging Fourier transform spectrometer GLORIA". In: *Atmospheric Measurement Techniques* 7.10, pp. 3565–3577. DOI: 10.5194/amt-7-3565-2014.

Fritts, D. C. and M. J. Alexander (2003). "Gravity wave dynamics and effects in the middle atmosphere". In: *Reviews of Geophysics* 41.1. DOI: https://doi.org/10.1029/2001RG000106.

Fritts, D. C., R. B. Smith, M. J. Taylor, J. D. Doyle, S. D. Eckermann, A. Dörnbrack, M. Rapp, B. P. Williams, P.-D. Pautet, K. Bossert, et al. (2016). "The Deep Propagating Gravity Wave Experiment (DEEPWAVE): An airborne and ground-based exploration of gravity wave propagation and effects from their sources throughout the lower and

middle atmosphere". In: *Bulletin of the American Meteorological Society* 97.3, pp. 425–453.

Fujii, T. (2005). *Laser Remote Senising*. CRC Press.

Fujita, T. T. (1981). "Tornadoes and Downbursts in the Context of Generalized Planetary Scales". In: *Journal of Atmospheric Sciences* 38.8, pp. 1511–1534. DOI: https://doi.org/10.1175/1520-0469(1981)038<1511:TADITC>2.0.CO;2.

Gadsden, M. (1982). "Noctilucent clouds". In: *Space Science Reviews* 33.3, pp. 279–334.

Gage, K. S. (1979). "Evidence for a $k^{-5/3}$ Law Inertial Range in Mesoscale Two-Dimensional Turbulence". In: *Journal of Atmospheric Sciences* 36.10, pp. 1950–1954. DOI: 10.1175/1520-0469(1979)036<1950:EFALIR>2.0.CO;2.

Gage, K.S. and B. B. Balsley (1984). "MST radar studies of wind and turbulence in the middle atmosphere". In: *Journal of Atmospheric and Terrestrial Physics* 46.9, pp. 739–753. DOI: https://doi.org/10.1016/0021-9169(84)90055-2.

Gallego, D., P. Ribera, R. Garcia-Herrera, E. Hernandez, and L. Gimeno (2005). "A new look for the Southern Hemisphere jet stream". In: *Climate Dynamics* 24.6, pp. 607–621. DOI: 10.1007/s00382-005-0006-7.

Gao, X. and J. W. Meriwether (1998). "Mesoscale airborne in situ and lidar observations of variance and spatial structure in the troposphere and stratosphere regions". In: *Journal of Geophysical Research: Atmospheres* 103.D6, pp. 6391–6396. DOI: https://doi.org/10.1029/97JD03080.

Gardner, C. S. (1991). "Introduction to ALOHA-90: The airborne lidar and observations of the Hawaiian Airglow Campaign". In: *Geophysical research letters* 18.7, pp. 1313–1316.

– (1994). "Diffusive filtering theory of gravity wave spectra in the atmosphere". In: *Journal of Geophysical Research: Atmospheres* 99.D10, pp. 20601–20622. DOI: https://doi.org/10.1029/94JD00819.

– (1995). "Introduction to ALOHA/ANLC-93: The 1993 airborne lidar and observations of the Hawaiian airglow/airborne noctilucent cloud campaigns". In: *Geophysical Research Letters* 22.20, pp. 2789–2792.

– (Sept. 2004). "Performance capabilities of middle-atmosphere temperature lidars: comparison of Na, Fe, K, Ca, Ca+, and Rayleigh systems". In: *Appl. Opt.* 43.25, pp. 4941–4956. DOI: 10.1364/AO.43.004941.

Gardner, C. S., C. A. Hostetler, and S. J. Franke (1993). "Gravity wave models for the horizontal wave number spectra of atmospheric velocity and density fluctuations". In: *Journal of Geophysical Research: Atmospheres* 98.D1, pp. 1035–1049. DOI: https://doi.org/10.1029/92JD02051.

Garreaud, R. D. (2009). "The Andes climate and weather". In: *Advances in Geosciences* 22, pp. 3–11. DOI: 10.5194/adgeo-22-3-2009.

Garreaud, R. D., M. Vuille, R. Compagnucci, and J. Marengo (Oct. 2008). "Present-day South American Climate". In: *Palaeogeography Palaeoclimatology Palaeoecology* 281. DOI: 10.1016/j.palaeo.2007.10.032.

Gatt, P., S. Johnson, and T. Nichols (2007). "Dead-time effects on geiger-mode APD performance". In: *Laser Radar Technology and Applications XII*. Ed. by Monte D.

Turner and Gary W. Kamerman. Vol. 6550. International Society for Optics and Photonics. SPIE, p. 65500I. DOI: 10.1117/12.724773.

Geldenhuys, M., B. Kaifler, P. Preusse, J. Ungermann, P. Alexander, L. Krasauskas, S. Rhode, W. Woiwode, M. Ern, M. Rapp, and M. Riese (2023). "Observations of gravity wave refraction and its causes and consequences". In: *Journal of Geophysical Research: Atmospheres* n/a.n/a. e2022JD036830 2022JD036830, e2022JD036830. DOI: https://doi.org/10.1029/2022JD036830.

Geller, M. A. and J. Gong (2010). "Gravity wave kinetic, potential, and vertical fluctuation energies as indicators of different frequency gravity waves". In: *Journal of Geophysical Research: Atmospheres* 115.D11. DOI: https://doi.org/10.1029/2009JD012266.

Gerding, M., M. Kopp, J. Höffner, K. Baumgarten, and F.-J. Lübken (2016). "Mesospheric temperature soundings with the new, daylight-capable IAP RMR lidar". In: *Atmospheric Measurement Techniques* 9.8, pp. 3707–3715. DOI: 10.5194/amt-9-3707-2016.

Geusic, J. E., H. M. Marcos, and L. G. Van Uitert (1964). "Laser oscillations in Nd-doped yttrium aluminum, yttrium gallium and gadolinium garnets". In: *Applied Physics Letters* 4.10, pp. 182–184.

Giez, A., C. Mallaun, M. Zöger, A. Dörnbrack, and U. Schumann (2017). "Static Pressure from Aircraft Trailing-Cone Measurements and Numerical Weather-Prediction Analysis". In: *Journal of Aircraft* 54.5, pp. 1728–1737. DOI: 10.2514/1.C034084.

Gisinger, S., I. Polichtchouk, A. Dörnbrack, R. Reichert, B. Kaifler, N. Kaifler, M. Rapp, and I. Sandu (2022). "Gravity-Wave-Driven Seasonal Variability of Temperature Differences Between ECMWF IFS and Rayleigh Lidar Measurements in the Lee of the Southern Andes". In: *Journal of Geophysical Research: Atmospheres* 127.13. e2021JD036270 2021JD036270, e2021JD036270. DOI: https://doi.org/10.1029/2021JD036270.

Godin, S., G. Mégie, C. David, D. Haner, C. Flesia, and Y. Emery (1994). "Airborne lidar observation of mountain-wave-induced polar stratospheric clouds during EASOE". In: *Geophysical research letters* 21.13, pp. 1335–1338.

Goldstein, S. (1931). "On the stability of superposed streams of Fluids of different densities". In: *Proceedings of the Royal Society of London. Series A, Containing Papers of a Mathematical and Physical Character* 132.820, pp. 524–548. DOI: 10.1098/rspa.1931.0116.

Goncharenko, L. P., V. L. Harvey, K. R. Greer, S.-R. Zhang, and A. J. Coster (2020). "Longitudinally Dependent Low-Latitude Ionospheric Disturbances Linked to the Antarctic Sudden Stratospheric Warming of September 2019". In: *Journal of Geophysical Research: Space Physics* 125.8. e2020JA028199 2020JA028199, e2020JA028199. DOI: https://doi.org/10.1029/2020JA028199.

Goodman, J. W. (2000). *Statistical Optics*.

Gray, L., W. Norton, C. Pascoe, and A. Charlton (2005). "A Possible Influence of Equatorial Winds on the September 2002 Southern Hemisphere Sudden Warming Event". In: *Journal of the Atmospheric Sciences* 62.3, pp. 651–667. DOI: https://doi.org/10.1175/JAS-3339.1.

Harvey, V. L., C. E. Randall, S. M. Bailey, E. Becker, J. L. Chau, C. Y. Cullens, L. P. Goncharenko, L. L. Gordley, N. P. Hindley, R. S. Lieberman, H.-L. Liu, L. Megner,

S. E. Palo, N. M. Pedatella, D. E. Siskind, F. Sassi, Anne K. Smith, G. Stober, C. Stolle, and J. Yue (2022). "Improving ionospheric predictability requires accurate simulation of the mesospheric polar vortex". In: *Frontiers in Astronomy and Space Sciences* 9. DOI: 10.3389/fspas.2022.1041426.

Hauchecorne, A. (1995). "Lidar Temperature Measurements in the Middle Atmosphere". In: *The Review of Laser Engineering* 23.2, pp. 119–123. DOI: 10.2184/lsj.23.119.

Hauchecorne, A. and M.-L. Chanin (1980). "Density and temperature profiles obtained by lidar between 35 and 70 km". In: *Geophysical Research Letters* 7.8, pp. 565–568. DOI: https://doi.org/10.1029/GL007i008p00565.

Hays, P. B. and R. G. Roble (1973). "Observation of mesospheric ozone at low latitudes". In: *Planetary and Space Science* 21.2, pp. 273–279. DOI: https://doi.org/10.1016/0032-0633(73)90011-1.

Hersbach, H., B. Bell, P. Berrisford, S. Hirahara, A. Horányi, J. Muñoz-Sabater, J. Nicolas, C. Peubey, R. Radu, D. Schepers, A. Simmons, C. Soci, S. Abdalla, X. Abellan, G. Balsamo, P. Bechtold, G. Biavati, J. Bidlot, M. Bonavita, G. De Chiara, P. Dahlgren, D. Dee, M. Diamantakis, R. Dragani, J. Flemming, R. Forbes, M. Fuentes, A. Geer, L. Haimberger, S. Healy, R. J. Hogan, E. Hólm, M. Janisková, S. Keeley, P. Laloyaux, P. Lopez, C. Lupu, G. Radnoti, P. de Rosnay, I. Rozum, F. Vamborg, S. Villaume, and J.-N. Thépaut (2020). "The ERA5 global reanalysis". In: *Quarterly Journal of the Royal Meteorological Society* 146.730, pp. 1999–2049. DOI: https://doi.org/10.1002/qj.3803.

Hindley, N. P., C. J. Wright, L. Hoffmann, T. Moffat-Griffin, and N. J. Mitchell (2020). "An 18-Year Climatology of Directional Stratospheric Gravity Wave Momentum Flux From 3-D Satellite Observations". In: *Geophysical Research Letters* 47.22. e2020GL089557 10.1029/2020GL089557, e2020GL089557. DOI: https://doi.org/10.1029/2020GL089557.

Hines, C. O. (Jan. 1974). "Atmospheric gravity waves: A new toy for the wave theorist". In: *Washington DC American Geophysical Union Geophysical Monograph Series* 18, pp. 198–206. DOI: 10.1029/GM018p0198.

Holton, J. R. (1983). "The Influence of Gravity Wave Breaking on the General Circulation of the Middle Atmosphere". In: *Journal of Atmospheric Sciences* 40.10, pp. 2497–2507. DOI: https://doi.org/10.1175/1520-0469(1983)040<2497:TIOGWB>2.0.CO;2.

Holton, J. R. and G. J. Hakim (2013). *An Introduction to Dynamic Meteorology (Fifth Edition)*. Ed. by J. R. Holton and G. J. Hakim. Fifth Edition. Boston: Academic Press, pp. 1–29. DOI: https://doi.org/10.1016/B978-0-12-384866-6.00001-5.

Hostetler, C. A. and C. S. Gardner (1994). "Observations of horizontal and vertical wave number spectra of gravity wave motions in the stratosphere and mesosphere over the mid-Pacific". In: *Journal of Geophysical Research: Atmospheres* 99.D1, pp. 1283–1302. DOI: https://doi.org/10.1029/93JD02927.

Hostetler, C. A., C. S. Gardner, R. A. Vincent, and D. Lesicar (1991). "Spectra of gravity wave density and wind perturbations observed during ALOHA-90 on the 25 March flight between Maui and Christmas Island". In: *Geophysical Research Letters* 18.7, pp. 1325–1328. DOI: https://doi.org/10.1029/91GL01150.

Houghton, J. T. (1978). "The stratosphere and mesosphere". In: *Quarterly Journal of the Royal Meteorological Society* 104.439, pp. 1–29. DOI: https://doi.org/10.1002/qj.49710443902.

Hu, Y. (2020). "The very unusual polar stratosphere in 2019–2020". In: *Science Bulletin* 65.21, pp. 1775–1777. DOI: https://doi.org/10.1016/j.scib.2020.07.011.

Jalali, A., S. Hicks-Jalali, R. J. Sica, A. Haefele, and T. von Clarmann (2019). "A practical information-centered technique to remove a priori information from lidar optimal-estimation-method retrievals". In: *Atmospheric Measurement Techniques* 12.7, pp. 3943–3961. DOI: 10.5194/amt-12-3943-2019.

Jalali, A., R. J. Sica, and A. Haefele (2018). "Improvements to a long-term Rayleigh-scatter lidar temperature climatology by using an optimal estimation method". In: *Atmospheric Measurement Techniques* 11.11, pp. 6043–6058. DOI: 10.5194/amt-11-6043-2018.

Jasperson, W. H., G. D. Nastrom, and D. C. Fritts (1990). "Further Study of Terrain Effects on the Mesoscale Spectrum of Atmospheric Motions". In: *Journal of Atmospheric Sciences* 47.8, pp. 979–987. DOI: https://doi.org/10.1175/1520-0469(1990)047<0979:FSOTEO>2.0.CO;2.

Johnson, E. A., R. C. Meyer, R. E. Hopkins, and W. H. Mock (1939). "The measurement of light scattered by the upper atmosphere from a search-light beam". In: *JOSA* 29.12, pp. 512–517.

Jucker, M. and R. Goyal (2022). "Ozone-Forced Southern Annular Mode During Antarctic Stratospheric Warming Events". In: *Geophysical Research Letters* 49.4. e2021GL095270 2021GL095270, e2021GL095270. DOI: https://doi.org/10.1029/2021GL095270.

Jucker, M., T. Reichler, and D. W. Waugh (2021). "How Frequent Are Antarctic Sudden Stratospheric Warmings in Present and Future Climate?" In: *Geophysical Research Letters* 48.11. e2021GL093215 2021GL093215, e2021GL093215. DOI: https://doi.org/10.1029/2021GL093215.

Junge, C. E., C. W. Chagnon, and J. E. Manson (1961). "A world-wide stratospheric aerosol layer". In: *Science* 133.3463, pp. 1478–1479.

Kaifler, B., C. Büdenbender, P. Mahnke, M. Damm, D. Sauder, N. Kaifler, and M. Rapp (Aug. 2017). "Demonstration of an iron fluorescence lidar operating at 372 nm wavelength using a newly-developed Nd:YAG laser". In: *Opt. Lett.* 42.15, pp. 2858–2861. DOI: 10.1364/OL.42.002858.

Kaifler, B. and N. Kaifler (2021). "A Compact Rayleigh Autonomous Lidar (CORAL) for the middle atmosphere". In: *Atmospheric Measurement Techniques* 14.2, pp. 1715–1732. DOI: 10.5194/amt-14-1715-2021.

Kaifler, B., N. Kaifler, B. Ehard, A. Dörnbrack, M. Rapp, and D. C. Fritts (2015). "Influences of source conditions on mountain wave penetration into the stratosphere and mesosphere". In: *Geophysical Research Letters* 42.21, pp. 9488–9494. DOI: https://doi.org/10.1002/2015GL066465.

Kaifler, B., D. Rempel, P. Roßi, C. Büdenbender, N. Kaifler, and V. Baturkin (2020a). "A technical description of the Balloon Lidar Experiment (BOLIDE)". In: *Atmospheric Measurement Techniques* 13.10, pp. 5681–5695. DOI: 10.5194/amt-13-5681-2020.

Kaifler, N., B. Kaifler, A. Dörnbrack, M. Rapp, J. L. Hormaechea, and A. de la Torre (2020b). "Lidar observations of large-amplitude mountain waves in the stratosphere

above Tierra del Fuego, Argentina". In: *Scientific Reports* 10.14529. DOI: https://doi.org/10.1038/s41598-020-71443-7.

Kaifler, N., B. Kaifler, M. Rapp, and D. C. Fritts (2022). "The polar mesospheric cloud dataset of the Balloon Lidar Experiment BOLIDE". In: *Earth System Science Data Discussions* 2022, pp. 1–17. DOI: 10.5194/essd-2022-158.

Keckhut, P., M. L. Chanin, and A. Hauchecorne (Dec. 1990). "Stratosphere temperature measurement using Raman lidar". In: *Appl. Opt.* 29.34, pp. 5182–5186. DOI: 10.1364/AO.29.005182.

Keller, T. L. (1994). "Implications of the Hydrostatic Assumption on Atmospheric Gravity Waves". In: *Journal of Atmospheric Sciences* 51.13, pp. 1915–1929. DOI: 10.1175/1520-0469(1994)051<1915:IOTHAO>2.0.CO;2.

Kelley, M. C. (2009). *The Earth's ionosphere*. Academic press.

Kent, G. S. and R. W. H. Wright (1970). "A review of laser radar measurements of atmospheric properties". In: *Journal of Atmospheric and Terrestrial Physics* 32, p. 917.

Kenyon, I. R. (2008). *The light fantastic: a modern introduction to classical and quantum optics*. Oxford University Press, USA.

Kim, Y.-J., S. E. Eckermann, and H.-Y. Chun (2003). "An overview of the past, present and future of gravity wave drag parametrization for numerical climate and weather prediction models". In: *Atmosphere-Ocean* 41.1, pp. 65–98. DOI: 10.3137/ao.410105.

Knobloch, S., B. Kaifler, A. Dörnbrack, and M. Rapp (2023). "Horizontal Wavenumber Spectra Across the Middle Atmosphere From Airborne Lidar Observations During the 2019 Southern Hemispheric SSW". In: *Geophysical Research Letters* 50.14. e2023GL104357 2023GL104357, e2023GL104357. DOI: https://doi.org/10.1029/2023GL104357.

Knobloch, S., B. Kaifler, and M. Rapp (2022). "Estimating the uncertainty of middle-atmospheric temperatures retrieved from airborne Rayleigh lidar measurements". In: *Atmospheric Measurement Techniques Discussions* 2022, pp. 1–27. DOI: 10.5194/amt-2021-310.

Kogure, M., J. Yue, and H. Liu (2021). "Gravity Wave Weakening During the 2019 Antarctic Stratospheric Sudden Warming". In: *Geophysical Research Letters* 48.8, e2021GL092537. DOI: https://doi.org/10.1029/2021GL092537.

Kohma, M., K. Sato, K. Nishimura, and M. Tsutsumi (2021). "Weakening of Polar Mesosphere Winter Echo and Turbulent Energy Dissipation Rates After a Stratospheric Sudden Warming in the Southern Hemisphere in 2019". In: *Geophysical Research Letters* 48.10. e2021GL092705 2021GL092705, e2021GL092705. DOI: https://doi.org/10.1029/2021GL092705.

Kolmogorov, A. N. (1941). "The Local Structure of Turbulence in incompressible viscous fluids for very large Reynolds numbers". In: *C. R. Acad. Sci. URSS* 30, pp. 301–305.

Koshyk, J. N., B. A. Boville, K. Hamilton, E. Manzini, and K. Shibata (1999). "Kinetic energy spectrum of horizontal motions in middle-atmosphere models". In: *Journal of Geophysical Research: Atmospheres* 104.D22, pp. 27177–27190. DOI: https://doi.org/10.1029/1999JD900814.

Koshyk, J. N. and K. Hamilton (2001). "The Horizontal Kinetic Energy Spectrum and Spectral Budget Simulated by a High-Resolution Troposphere–Stratosphere–Mesosphere

GCM". In: *Journal of the Atmospheric Sciences* 58.4, pp. 329–348. DOI: https://doi.org/10.1175/1520-0469(2001)058<0329:THKESA>2.0.CO;2.

Kraichnan, R. H. (1967). "Inertial Ranges in Two-Dimensional Turbulence". In: *The Physics of Fluids* 10.7, pp. 1417–1423. DOI: 10.1063/1.1762301.

Krasauskas, L., B. Kaifler, S. Rhode, J. Ungermann, W. Woiwode, and P. Preusse (2023). "Oblique Propagation and Refraction of Gravity Waves Over the Andes Observed by GLORIA and ALIMA During the SouthTRAC Campaign". In: *Journal of Geophysical Research: Atmospheres* 128.10. e2022JD037798 2022JD037798, e2022JD037798. DOI: https://doi.org/10.1029/2022JD037798.

Kremser, S., L. W. Thomason, M. von Hobe, M. Hermann, T. Deshler, C. Timmreck, M. Toohey, A. Stenke, J. P. Schwarz, R. Weigel, S. Fueglistaler, F. J. Prata, J.-P. Vernier, H. Schlager, J. E. Barnes, J.-C. Antuña-Marrero, D. Fairlie, M. Palm, E. Mahieu, J. Notholt, M. Rex, C. Bingen, F. Vanhellemont, A. Bourassa, J. M. C. Plane, D. Klocke, S. A. Carn, L. Clarisse, T. Trickl, R. Neely, A. D. James, L. Rieger, J. C. Wilson, and B. Meland (2016). "Stratospheric aerosol—Observations, processes, and impact on climate". In: *Reviews of Geophysics* 54.2, pp. 278–335. DOI: https://doi.org/10.1002/2015RG000511.

Kwon, K. H., D. C. Senft, and C. S. Gardner (1990). "Airborne sodium lidar observations of horizontal and vertical wave number spectra of mesopause density and wind perturbations". In: *Journal of Geophysical Research: Atmospheres* 95.D9, pp. 13723–13736. DOI: https://doi.org/10.1029/JD095iD09p13723.

Lane, T. P., M. J. Reeder, and F. M. Guest (2003). "Convectively generated gravity waves observed from radiosonde data taken during MCTEX". In: *Quarterly Journal of the Royal Meteorological Society* 129.590, pp. 1731–1740. DOI: https://doi.org/10.1256/qj.02.196.

Leblanc, T., I. S. McDermid, A. Hauchecorne, and P. Keckhut (1998). "Evaluation of optimization of lidar temperature analysis algorithms using simulated data". In: *Journal of Geophysical Research: Atmospheres* 103.D6, pp. 6177–6187. DOI: https://doi.org/10.1029/97JD03494.

Leblanc, T., R. J. Sica, J. A. E. van Gijsel, A. Haefele, G. Payen, and G. Liberti (2016). "Proposed standardized definitions for vertical resolution and uncertainty in the NDACC lidar ozone and temperature algorithms – Part 3: Temperature uncertainty budget". In: *Atmospheric Measurement Techniques* 9.8, pp. 4079–4101. DOI: 10.5194/amt-9-4079-2016.

Lee, W., I.-S. Song, J.-H. Kim, Y. H. Kim, S.-H. Jeong, S. Eswaraiah, and D. J. Murphy (2021). "The Observation and SD-WACCM Simulation of Planetary Wave Activity in the Middle Atmosphere During the 2019 Southern Hemispheric Sudden Stratospheric Warming". In: *Journal of Geophysical Research: Space Physics* 126.6. e2020JA029094 2020JA029094, e2020JA029094. DOI: https://doi.org/10.1029/2020JA029094.

Leovy, C. (1964). "Simple Models of Thermally Driven Mesopheric Circulation". In: *Journal of Atmospheric Sciences* 21.4, pp. 327–341v. DOI: https://doi.org/10.1175/1520-0469(1964)021<0327:SMOTDM>2.0.CO;2v.

Li, Q. and E. Lindborg (2018). "Weakly or Strongly Nonlinear Mesoscale Dynamics Close to the Tropopause?" In: *Journal of the Atmospheric Sciences* 75.4, pp. 1215–1229. DOI: https://doi.org/10.1175/JAS-D-17-0063.1.

Ligda, M. G. H. (1951). "Radar Storm Observation". In: *Compendium of Meteorology: Prepared under the Direction of the Committee on the Compendium of Meteorology*. Ed. by T. F. Malone. Boston, MA: American Meteorological Society, pp. 1265–1282. DOI: 10.1007/978-1-940033-70-9_103.

Lilly, D. K. (1983). "Stratified Turbulence and the Mesoscale Variability of the Atmosphere". In: *Journal of Atmospheric Sciences* 40.3, pp. 749–761. DOI: 10.1175/1520-0469(1983)040<0749:STATMV>2.0.CO;2.

– (1989). "Two-Dimensional Turbulence Generated by Energy Sources at Two Scales". In: *Journal of Atmospheric Sciences* 46.13, pp. 2026–2030. DOI: https://doi.org/10.1175/1520-0469(1989)046<2026:TDTGBE>2.0.CO;2.

Lilly, D. K. and E. L. Petersen (1983). "Aircraft measurements of atmospheric kinetic energy spectra". In: *Tellus A* 35A.5, pp. 379–382. DOI: https://doi.org/10.1111/j.1600-0870.1983.tb00212.x.

Lim, E.-P., H. H. Hendon, A. H. Butler, R. D. Garreaud, I. Polichtchouk, T. G. Shepherd, A. A. Scaife, R. Comer, L. Coy, P. A. Newman, D. W. J. Thompson, and H. Nakamura (Jan. 2020). "The 2019 Antarctic sudden stratospheric warming". In: *SPARC Newsletter* 54.

Lim, E.-P., H. H. Hendon, A. H. Butler, D. W. J. Thompson, Z. D. Lawrence, A. A. Scaife, T. G. Shepherd, I. Polichtchouk, H. Nakamura, C. Kobayashi, R. Comer, L. Coy, A. Dowdy, R. D. Garreaud, P. A. Newman, and G. Wang (2021). "The 2019 Southern Hemisphere Stratospheric Polar Vortex Weakening and Its Impacts". In: *Bulletin of the American Meteorological Society* 102.6, E1150–E1171. DOI: 10.1175/BAMS-D-20-0112.1.

Lin, Y.-L. (2007). *Mesoscale Dynamics*. Cambridge University Press. DOI: 10.1017/CBO9780511619649.

Lindborg, E. (1999). "Can the atmospheric kinetic energy spectrum be explained by two-dimensional turbulence?" In: *Journal of Fluid Mechanics* 388, pp. 259–288. DOI: 10.1017/S0022112099004851.

– (2005). "The effect of rotation on the mesoscale energy cascade in the free atmosphere". In: *Geophysical Research Letters* 32.1. DOI: https://doi.org/10.1029/2004GL021319.

– (2006). "The energy cascade in a strongly stratified fluid". In: *Journal of Fluid Mechanics* 550, pp. 207–242. DOI: 10.1017/S0022112005008128.

Lindgren, E. A., A. Sheshadri, A. Podglajen, and R. W. Carver (2020). "Seasonal and Latitudinal Variability of the Gravity Wave Spectrum in the Lower Stratosphere". In: *Journal of Geophysical Research: Atmospheres* 125.18, e2020JD032850. DOI: https://doi.org/10.1029/2020JD032850.

Lindzen, R. S. (1981). "Turbulence and stress owing to gravity wave and tidal breakdown". In: *Journal of Geophysical Research: Oceans* 86.C10, pp. 9707–9714. DOI: https://doi.org/10.1029/JC086iC10p09707.

Liu, G., D. Janches, R. S. Lieberman, T. Moffat-Griffin, N. J. Mitchell, J.-H. Kim, and C. Lee (2021). "Wind Variations in the Mesosphere and Lower Thermosphere Near 60°S Latitude During the 2019 Antarctic Sudden Stratospheric Warming". In: *Journal of Geophysical Research: Space Physics* 126.5. e2020JA028909 2020JA028909, e2020JA028909. DOI: https://doi.org/10.1029/2020JA028909.

Liu, G., D. Janches, J. Ma, R. S. Lieberman, G. Stober, T. Moffat-Griffin, N. J. Mitchell, J.-H. Kim, C. Lee, and D. J. Murphy (2022). "Mesosphere and Lower Thermosphere Winds and Tidal Variations During the 2019 Antarctic Sudden Stratospheric Warming". In: *Journal of Geophysical Research: Space Physics* 127.3. e2021JA030177 2021JA030177, e2021JA030177. DOI: https://doi.org/10.1029/2021JA030177.

Lübken, F.-J. (1997). "Seasonal variation of turbulent energy dissipation rates at high latitudes as determined by in situ measurements of neutral density fluctuations". In: *Journal of Geophysical Research: Atmospheres* 102.D12, pp. 13441–13456. DOI: https://doi.org/10.1029/97JD00853.

Maiman, T. H. (1960). "Stimulated Optical Radiation in Ruby". In: *Nature* 187.4736, pp. 493–494.

Manney, G. L., A. H. Butler, Z. D. Lawrence, K. Wargan, and M. L. Santee (2022). "What's in a Name? On the Use and Significance of the Term "Polar Vortex"". In: *Geophysical Research Letters* 49.10. e2021GL097617 2021GL097617, e2021GL097617. DOI: https://doi.org/10.1029/2021GL097617.

Manney, G. L., M. I. Hegglin, W. H. Daffer, M. L. Santee, E. A. Ray, S. Pawson, M. J. Schwartz, C. D. Boone, L. Froidevaux, N. J. Livesey, W. G. Read, and K. A. Walker (2011). "Jet characterization in the upper troposphere/lower stratosphere (UTLS): applications to climatology and transport studies". In: *Atmospheric Chemistry and Physics* 11.12, pp. 6115–6137. DOI: 10.5194/acp-11-6115-2011.

Manney, G. L., M. I. Hegglin, W. H. Daffer, M. J. Schwartz, M. L. Santee, and S. Pawson (2014). "Climatology of Upper Tropospheric–Lower Stratospheric (UTLS) Jets and Tropopauses in MERRA". In: *Journal of Climate* 27.9, pp. 3248–3271. DOI: 10.1175/JCLI-D-13-00243.1.

Markowski, P and Y. Richardson (2010). *Mesoscale Meteorology in Midlatitudes*. John Wiley and Sons, Ltd, p. 414. DOI: https://doi.org/10.1002/9780470682104.fmatter.

Matsuno, T. (1971). "A Dynamical Model of the Stratospheric Sudden Warming". In: *Journal of Atmospheric Sciences* 28.8, pp. 1479–1494. DOI: https://doi.org/10.1175/1520-0469(1971)028<1479:ADMOTS>2.0.CO;2.

– (1982). "A Quasi One-Dimensional Model of the Middle Atmosphere Circulation Interacting with Internal Gravity Waves". In: *Journal of the Meteorological Society of Japan. Ser. II* 60.1, pp. 215–226. DOI: 10.2151/jmsj1965.60.1_215.

McGee, T. J., M. R. Gross, U. N. Singh, J. J. Butler, and P. E. Kimvilakani (1995). "Improved stratospheric ozone lidar". In: *Optical Engineering* 34.5, pp. 1421–1430. DOI: 10.1117/12.199883.

McLandress, C. (1998). "On the importance of gravity waves in the middle atmosphere and their parameterization in general circulation models". In: *Journal of Atmospheric*

and Solar-Terrestrial Physics 60.14, pp. 1357–1383. DOI: https://doi.org/10.1016/S1364-6826(98)00061-3.

McLandress, C., M. J. Alexander, and D. L. Wu (2000). "Microwave Limb Sounder observations of gravity waves in the stratosphere: A climatology and interpretation". In: *Journal of Geophysical Research: Atmospheres* 105.D9, pp. 11947–11967. DOI: https://doi.org/10.1029/2000JD900097.

McLandress, C., T. G. Shepherd, S. Polavarapu, and S. R. Beagley (2012). "Is Missing Orographic Gravity Wave Drag near 60°S the Cause of the Stratospheric Zonal Wind Biases in Chemistry–Climate Models?" In: *Journal of the Atmospheric Sciences* 69.3, pp. 802–818. DOI: 10.1175/JAS-D-11-0159.1.

Menchaca, M. Q. and D. R. Durran (2019). "The Influence of Gravity Waves on the Slope of the Kinetic Energy Spectrum in Simulations of Idealized Midlatitude Cyclones". In: *Journal of the Atmospheric Sciences* 76.7, pp. 2103–2122. DOI: 10.1175/JAS-D-18-0329.1.

Middleton, W. E. K. (1939). "On the theory of the ceiling projector". In: *JOSA* 29.8, pp. 340–349.

Mie, G. (1908). "Beiträge zur Optik trüber Medien, speziell kolloidaler Metallösungen". In: *Annalen der Physik* 330.3, pp. 377–445. DOI: https://doi.org/10.1002/andp.19083300302.

Mitra, G., A. Guharay, P. P. Batista, R. A. Buriti, and T. Moffat-Griffin (2023). "Investigation on the MLT tidal variability during September 2019 minor sudden stratospheric warming". In: *Advances in Space Research* 71.1, pp. 869–882. DOI: https://doi.org/10.1016/j.asr.2022.08.017.

Murgatroyd, R. J. and F. Singleton (1961). "Possible meridional circulations in the stratosphere and mesosphere". In: *Quarterly Journal of the Royal Meteorological Society* 87.372, pp. 125–135. DOI: https://doi.org/10.1002/qj.49708737202.

Nakamura, H. and A. Shimpo (2004). "Seasonal Variations in the Southern Hemisphere Storm Tracks and Jet Streams as Revealed in a Reanalysis Dataset". In: *Journal of Climate* 17.9, pp. 1828–1844. DOI: 10.1175/1520-0442(2004)017<1828:SVITSH>2.0.CO;2.

Nappo, C. J. (2012). *An Introduction to Atmospheric Gravity Waves*. Vol. 102. International Geophysics. Academic Press, p. iv. DOI: https://doi.org/10.1016/B978-0-12-385223-6.00014-8.

Nastrom, G. D., D. C. Fritts, and K. S. Gage (1987). "An Investigation of Terrain Effects on the Mesoscale Spectrum of Atmospheric Motions". In: *Journal of Atmospheric Sciences* 44.20, pp. 3087–3096. DOI: 10.1175/1520-0469(1987)044<3087:AIOTEO>2.0.CO;2.

Nastrom, G. D. and K. S. Gage (1983). "A first look at wavenumber spectra from GASP data". In: *Tellus A: Dynamic Meteorology and Oceanography* 35.5, pp. 383–388. DOI: 10.3402/tellusa.v35i5.11449.

– (1985). "A Climatology of Atmospheric Wavenumber Spectra of Wind and Temperature Observed by Commercial Aircraft". In: *Journal of Atmospheric Sciences* 42.9, pp. 950–960. DOI: 10.1175/1520-0469(1985)042<0950:ACOAWS>2.0.CO;2.

Nastrom, G. D., W. H. Jasperson, and K. S. Gage (July 1984). "Kinetic energy spectrum of large- and mesoscale atmospheric processes". In: *Nature* 310, pp. 36–38. DOI: 10.1038/310036a0.

Noguchi, S., Y. Kuroda, K. Kodera, and S. Watanabe (2020). "Robust Enhancement of Tropical Convective Activity by the 2019 Antarctic Sudden Stratospheric Warming". In: *Geophysical Research Letters* 47.15. e2020GL088743 2020GL088743, e2020GL088743. DOI: https://doi.org/10.1029/2020GL088743.

Obukhov, A. M. (1949). "Structure of the temperature field in a turbulent flow". In: *Izv. Akad. Nauk SSSR, Ser. Geogr. Geofiz* 13.1, pp. 58–69.

Orlanski, I. (1975). "A Rational Subdivision of Scales for Atmospheric Processes". In: *Bulletin of the American Meteorological Society* 56.5, pp. 527–530.

Paul, J., F. Fortuin, and H. Kelder (1998). "An ozone climatology based on ozonesonde and satellite measurements". In: *Journal of Geophysical Research: Atmospheres* 103.D24, pp. 31709–31734. DOI: https://doi.org/10.1029/1998JD200008.

Peel, M. C., B. L. Finlayson, and T. A. McMahon (2007). "Updated world map of the Köppen-Geiger climate classification". In: *Hydrology and Earth System Sciences* 11.5, pp. 1633–1644. DOI: 10.5194/hess-11-1633-2007.

Plougonven, Riwal, Alvaro de la Cámara, Albert Hertzog, and François Lott (2020). "How does knowledge of atmospheric gravity waves guide their parameterizations?" In: *Quarterly Journal of the Royal Meteorological Society* 146.728, pp. 1529–1543. DOI: https://doi.org/10.1002/qj.3732.

Polyakov, S. V. (2013). "Chapter 3 - Photomultiplier Tubes". In: *Single-Photon Generation and Detection*. Ed. by Alan Migdall, Sergey V. Polyakov, Jingyun Fan, and Joshua C. Bienfang. Vol. 45. Experimental Methods in the Physical Sciences. Academic Press, pp. 69–82. DOI: https://doi.org/10.1016/B978-0-12-387695-9.00003-2.

Pope, S. B. (2000). *Turbulent Flows*. Cambridge university press.

Preusse, P., S. D. Eckermann, and D. Offermann (2000). "Comparison of global distributions of zonal-mean gravity wave variance inferred from different satellite instruments". In: *Geophysical Research Letters* 27.23, pp. 3877–3880. DOI: https://doi.org/10.1029/2000GL011916.

Qian, J., Y. Y. Gu, G. C. Papen, C. S. Gardner, and P. J. Espy (1995). "Horizontal wave number spectra of density and temperature perturbations in the mesosphere measured during the 4 August flight of ANLC-93". In: *Geophysical Research Letters* 22.20, pp. 2865–2868. DOI: https://doi.org/10.1029/95GL02556.

Queney, P. (1948). "The Problem of Air Flow Over Mountains: A Summary of Theoretical Studies". In: *Bulletin of the American Meteorological Society* 29.1, pp. 16–26. DOI: 10.1175/1520-0477-29.1.16.

Ralph, F. M., P. J. Neiman, T. L. Keller, D. Levinson, and L. Fedor (1997). "Observations, Simulations, and Analysis of Nonstationary Trapped Lee Waves". In: *Journal of the Atmospheric Sciences* 54.10, pp. 1308–1333. DOI: 10.1175/1520-0469(1997)054<1308:OSAAON>2.0.CO;2.

Randel, W.J. (2003). "MIDDLE ATMOSPHERE | Zonal Mean Climatology". In: *Encyclopedia of Atmospheric Sciences*. Ed. by James R. Holton. Oxford: Academic Press, pp. 1358–1365. DOI: https://doi.org/10.1016/B0-12-227090-8/00227-X.

Rao, J., C. I. Garfinkel, I. P. White, and C. Schwartz (2020). "The Southern Hemisphere Minor Sudden Stratospheric Warming in September 2019 and its Predictions in S2S Models". In: *Journal of Geophysical Research: Atmospheres* 125.14. e2020JD032723 2020JD032723, e2020JD032723. DOI: https://doi.org/10.1029/2020JD032723.

Rapp, M., B. Kaifler, A. Dörnbrack, S. Gisinger, T. Mixa, R. Reichert, N. Kaifler, S. Knobloch, R. Eckert, N. Wildmann, A. Giez, L. Krasauskas, P. Preusse, M. Geldenhuys, M. Riese, W. Woiwode, F. Friedl-Vallon, B.-M. Sinnhuber, A. de la Torre, P. Alexander, J. L. Hormaechea, D. Janches, M. Garhammer, J. L. Chau, F. Conte, P. Hoor, and A. Engel (2021). "SOUTHTRAC-GW: An Airborne Field Campaign to Explore Gravity Wave Dynamics at the World's Strongest Hotspot". In: *Bulletin of the American Meteorological Society* 102.4, E871–E893. DOI: 10.1175/BAMS-D-20-0034.1.

Rapp, M. and F.-J. Lübken (2004). "Polar mesosphere summer echoes (PMSE): Review of observations and current understanding". In: *Atmospheric chemistry and physics* 4.11/12, pp. 2601–2633.

Rapp, M., B. Strelnikov, A. Müllemann, F.-J. Lübken, and D. C. Fritts (2004). "Turbulence measurements and implications for gravity wave dissipation during the MaCWAVE-MIDAS rocket program". In: *Geophysical Research Letters* 31.24. DOI: https://doi.org/10.1029/2003GL019325.

Rauthe, M., M. Gerding, J. Höffner, and F.-J. Lübken (2006). "Lidar temperature measurements of gravity waves over Kühlungsborn (54°N) from 1 to 105 km: A winter-summer comparison". In: *Journal of Geophysical Research: Atmospheres* 111.D24. DOI: https://doi.org/10.1029/2006JD007354.

Rauthe, M., M. Gerding, and F.-J. Lübken (2008). "Seasonal changes in gravity wave activity measured by lidars at mid-latitudes". In: *Atmospheric Chemistry and Physics* 8.22, pp. 6775–6787. DOI: 10.5194/acp-8-6775-2008.

Reichert, R., B. Kaifler, N. Kaifler, A. Dörnbrack, M. Rapp, and J. L. Hormaechea (2021). "High-Cadence Lidar Observations of Middle Atmospheric Temperature and Gravity Waves at the Southern Andes Hot Spot". In: *Journal of Geophysical Research: Atmospheres* 126.22. e2021JD034683 2021JD034683, e2021JD034683. DOI: https://doi.org/10.1029/2021JD034683.

Richardson, L. F. (1922). *Weather prediction by numerical process*. University Press.

Riese, M., H. Oelhaf, P. Preusse, J. Blank, M. Ern, F. Friedl-Vallon, H. Fischer, T. Guggenmoser, M. Höpfner, P. Hoor, M. Kaufmann, J. Orphal, F. Plöger, R. Spang, O. Suminska-Ebersoldt, J. Ungermann, B. Vogel, and W. Woiwode (2014). "Gimballed Limb Observer for Radiance Imaging of the Atmosphere (GLORIA) scientific objectives". In: *Atmospheric Measurement Techniques* 7.7, pp. 1915–1928. DOI: 10.5194/amt-7-1915-2014.

Rodriguez Imazio, P., P. D. Mininni, A. Godoy, N. Rivaben, and A. Dörnbrack (2023). "Not All Clear Air Turbulence Is Kolmogorov—The Fine-Scale Nature of Atmospheric Turbulence". In: *Journal of Geophysical Research: Atmospheres* 128.2. e2022JD037491 2022JD037491, e2022JD037491. DOI: https://doi.org/10.1029/2022JD037491.

Safieddine, S., M. Bouillon, A.-C. Paracho, J. Jumelet, F. Tencé, A. Pazmino, F. Goutail, C. Wespes, S. Bekki, A. Boynard, J. Hadji-Lazaro, P.-F. Coheur, D. Hurtmans, and C. Clerbaux (2020). "Antarctic Ozone Enhancement During the 2019 Sudden Strato-

spheric Warming Event". In: *Geophysical Research Letters* 47.14. e2020GL087810 2020GL087810, e2020GL087810. DOI: https://doi.org/10.1029/2020GL087810.

Schumann, U. (2019). "The Horizontal Spectrum of Vertical Velocities near the Tropopause from Global to Gravity Wave Scales". In: *Journal of the Atmospheric Sciences* 76.12, pp. 3847–3862. DOI: 10.1175/JAS-D-19-0160.1.

Scorer, R. S. (1949). "Theory of waves in the lee of mountains". In: *Quarterly Journal of the Royal Meteorological Society* 75.323, pp. 41–56. DOI: https://doi.org/10.1002/qj.49707532308.

Selz, T., L. Bierdel, and G. C. Craig (2019). "Estimation of the Variability of Mesoscale Energy Spectra with Three Years of COSMO-DE Analyses". In: *Journal of the Atmospheric Sciences* 76.2, pp. 627–637. DOI: 10.1175/JAS-D-18-0155.1.

Shen, X., L. Wang, and S. Osprey (2020a). "The Southern Hemisphere sudden stratospheric warming of September 2019". In: *Science Bulletin* 65.21, pp. 1800–1802. DOI: https://doi.org/10.1016/j.scib.2020.06.028.

– (2020b). "Tropospheric Forcing of the 2019 Antarctic Sudden Stratospheric Warming". In: *Geophysical Research Letters* 47.20. e2020GL089343 2020GL089343, e2020GL089343. DOI: https://doi.org/10.1029/2020GL089343.

Shepherd, T. G. (2000). "The middle atmosphere". In: *Journal of Atmospheric and Solar-Terrestrial Physics* 62.17, pp. 1587–1601. DOI: https://doi.org/10.1016/S1364-6826(00)00114-0.

Sica, R. J. and A. Haefele (2015). "Retrieval of temperature from a multiple-channel Rayleigh-scatter lidar using an optimal estimation method". In: *Appl. Opt.* 54.8, pp. 1872–1889. DOI: 10.1364/AO.54.001872.

Simmons, A., C. Soci, J. Nicolas, B. Bell, P. Berrisford, R. Dragani, J. Flemming, L. Haimberger, S. Healy, H. Hersbach, et al. (2020). "Global stratospheric temperature bias and other stratospheric aspects of ERA5 and ERA5.1". In: *Technical Memo* 859. DOI: https://doi.org/10.21957/rcxqfmg0.

Skamarock, W. C., S.-H. Park, J. B. Klemp, and C. Snyder (2014). "Atmospheric Kinetic Energy Spectra from Global High-Resolution Nonhydrostatic Simulations". In: *Journal of the Atmospheric Sciences* 71.11, pp. 4369–4381. DOI: 10.1175/JAS-D-14-0114.1.

Skamarock, William C. (2004). "Evaluating Mesoscale NWP Models Using Kinetic Energy Spectra". In: *Monthly Weather Review* 132.12, pp. 3019–3032. DOI: https://doi.org/10.1175/MWR2830.1.

Smith, R. B. and J. P. Evans (2007). "Orographic Precipitation and Water Vapor Fractionation over the Southern Andes". In: *Journal of Hydrometeorology* 8.1, pp. 3–19. DOI: 10.1175/JHM555.1.

Smolarkiewicz, P. K. and L. G. Margolin (1997). "On Forward-in-Time Differencing for Fluids: an Eulerian/Semi-Lagrangian Non-Hydrostatic Model for Stratified Flows". In: *Atmosphere-Ocean* 35.sup1, pp. 127–152. DOI: 10.1080/07055900.1997.9687345.

Stephan, C. C., J. Duras, L. Harris, D. Klocke, W. M. Putzman, M. Taylor, N. P. Wedi, N. Žagar, and F. Ziemen (2022). "Atmospheric Energy Spectra in Global Kilometre-Scale Models". In: *Tellus A: Dynamic Meteorology and Oceanography* 74.1, pp. 280–299. DOI: 10.16993/tellusa.26.

Sun, Y. Q., R. Rotunno, and F. Zhang (2017). "Contributions of Moist Convection and Internal Gravity Waves to Building the Atmospheric -5/3 Kinetic Energy Spectra". In: *Journal of the Atmospheric Sciences* 74.1, pp. 185–201. DOI: 10.1175/JAS-D-16-0097.1.

Synge, E. H. (1930). "XCI. A method of investigating the higher atmosphere". In: *The London, Edinburgh, and Dublin Philosophical Magazine and Journal of Science* 9.60, pp. 1014–1020.

Taylor, G. I. (1931). "Effect of variation in density on the stability of superposed streams of Fluid". In: *Proceedings of the Royal Society of London. Series A, Containing Papers of a Mathematical and Physical Character* 132.820, pp. 499–523. DOI: 10.1098/rspa.1931.0115.

Temme, F., J. V. Turton, T. Mölg, and S. Sauter (2020). "Flow Regimes and Föhn Types Characterize the Local Climate of Southern Patagonia". In: *Atmosphere* 11.9. DOI: 10.3390/atmos11090899.

Thayer, J. P., N. B. Nielsen, R. E. Warren, C. Heinselman, and J. Sohn (1997). "Rayleigh lidar system for middle atmosphere research in the arctic". In: *Optical Engineering* 36.7, pp. 2045–2061. DOI: 10.1117/1.601361.

Thompson, D. W. J. and J. M. Wallace (2000). "Annular Modes in the Extratropical Circulation. Part I: Month-to-Month Variability". In: *Journal of Climate* 13.5, pp. 1000–1016. DOI: https://doi.org/10.1175/1520-0442(2000)013<1000:AMITEC>2.0.CO;2.

Torrence, C. and G. P. Compo (1998). "A Practical Guide to Wavelet Analysis". In: *Bulletin of the American Meteorological Society* 79.1, pp. 61–78. DOI: 10.1175/1520-0477(1998)079<0061:APGTWA>2.0.CO;2.

Trenberth, K. E. (1991). "Storm Tracks in the Southern Hemisphere". In: *Journal of Atmospheric Sciences* 48.19, pp. 2159–2178. DOI: 10.1175/1520-0469(1991)048<2159:STITSH>2.0.CO;2.

Tsuda, T. (2014). "Characteristics of atmospheric gravity waves observed using the MU (Middle and Upper atmosphere) radar and GPS (Global Positioning System) radio occultation". In: *Proceedings of the Japan Academy, Series B* 90.1, pp. 12–27. DOI: 10.2183/pjab.90.12.

Tulloch, R. and K. S. Smith (2006). "A theory for the atmospheric energy spectrum: Depth-limited temperature anomalies at the tropopause". In: *Proceedings of the National Academy of Sciences* 103.40, pp. 14690–14694. DOI: 10.1073/pnas.0605494103.

Tung, K. K. and W. W. Orlando (2003). "The k–3 and k–5/3 Energy Spectrum of Atmospheric Turbulence: Quasigeostrophic Two-Level Model Simulation". In: *Journal of the Atmospheric Sciences* 60.6, pp. 824–835. DOI: https://doi.org/10.1175/1520-0469(2003)060<0824:TKAKES>2.0.CO;2.

Vadas, S. L., D. C. Fritts, and M. J. Alexander (2003). "Mechanism for the Generation of Secondary Waves in Wave Breaking Regions". In: *Journal of the Atmospheric Sciences* 60.1, pp. 194–214. DOI: 10.1175/1520-0469(2003)060<0194:MFTGOS>2.0.CO;2.

Vadas, S. L., J. Zhao, X. Chu, and E. Becker (2018). "The Excitation of Secondary Gravity Waves From Local Body Forces: Theory and Observation". In: *Journal of*

Geophysical Research: Atmospheres 123.17, pp. 9296–9325. DOI: https://doi.org/10.1029/2017JD027970.

Vallgren, A., E. Deusebio, and E. Lindborg (Dec. 2011). "Possible Explanation of the Atmospheric Kinetic and Potential Energy Spectra". In: *Phys. Rev. Lett.* 107 (26), p. 268501. DOI: 10.1103/PhysRevLett.107.268501.

Vallis, Geoffrey K (2017). *Atmospheric and oceanic fluid dynamics*. Cambridge University Press.

VanZandt, T. E. (1982). "A universal spectrum of buoyancy waves in the atmosphere". In: *Geophysical Research Letters* 9.5, pp. 575–578. DOI: https://doi.org/10.1029/GL009i005p00575.

Voigt, S., J. Orphal, K. Bogumil, and J. P. Burrows (2001). "The temperature dependence (203–293 K) of the absorption cross sections of O3 in the 230–850 nm region measured by Fourier-transform spectroscopy". In: *Journal of Photochemistry and Photobiology A: Chemistry* 143.1, pp. 1–9.

von Zahn, U., G. von Cossart, J. Fiedler, K. H. Fricke, G. Nelke, G. Baumgarten, D. Rees, A. Hauchecorne, and K. Adolfsen (2000). "The ALOMAR Rayleigh/Mie/Raman lidar: objectives, configuration, and performance". In: *Annales Geophysicae* 18.7, pp. 815–833. DOI: 10.1007/s00585-000-0815-2.

von Zahn, U., J. Höffner, V. Eska, and M. Alpers (1996). "The mesopause altitude: Only two distinctive levels worldwide?" In: *Geophysical Research Letters* 23.22, pp. 3231–3234. DOI: https://doi.org/10.1029/96GL03041.

Waite, M. L. and C. Snyder (2009). "The Mesoscale Kinetic Energy Spectrum of a Baroclinic Life Cycle". In: *Journal of the Atmospheric Sciences* 66.4, pp. 883–901. DOI: 10.1175/2008JAS2829.1.

Wallace, J. M. and P. V. Hobbs (2006). *Atmospheric science: an introductory survey*. Vol. 92. Elsevier.

Weitkamp, C. (2005). *"LIDAR": range-resolved optival remote sensing of the atmosphere*. Springer series in opitcal sciences.

Whiteway, J. A., T. J. Duck, D. P. Donovan, J. C. Bird, S. R. Pal, and A. I. Carswell (1997). "Measurements of gravity wave activity within and around the Arctic stratospheric vortex". In: *Geophysical Research Letters* 24.11, pp. 1387–1390. DOI: https://doi.org/10.1029/97GL01322.

Whiteway, James A. and Thomas J. Duck (1999). "Enhanced Arctic stratospheric gravity wave activity above a tropospheric jet". In: *Geophysical Research Letters* 26.16, pp. 2453–2456. DOI: https://doi.org/10.1029/1999GL900548.

Wing, R., A. Hauchecorne, P. Keckhut, S. Godin-Beekmann, S. Khaykin, and E. M. McCullough (2018a). "Lidar temperature series in the middle atmosphere as a reference data set – Part 2: Assessment of temperature observations from MLS/Aura and SABER/TIMED satellites". In: *Atmospheric Measurement Techniques* 11.12, pp. 6703–6717. DOI: 10.5194/amt-11-6703-2018.

Wing, R., A. Hauchecorne, P. Keckhut, S. Godin-Beekmann, S. Khaykin, E. M. McCullough, J.-F. Mariscal, and É. d'Almeida (2018b). "Lidar temperature series in the middle atmosphere as a reference data set – Part 1: Improved retrievals and a

20-year cross-validation of two co-located French lidars". In: *Atmospheric Measurement Techniques* 11.10, pp. 5531–5547. DOI: 10.5194/amt-11-5531-2018.

Wing, R., M. Martic, C. Triplett, A. Hauchecorne, J. Porteneuve, P. Keckhut, Y. Courcoux, L. Yung, P. Retailleau, and D. Cocuron (2021). "Gravity Wave Breaking Associated with Mesospheric Inversion Layers as Measured by the Ship-Borne BEM Monge Lidar and ICON-MIGHTI". In: *Atmosphere* 12.11. DOI: 10.3390/atmos12111386.

Wright, C. J., N. P. Hindley, M. J. Alexander, M. Barlow, L. Hoffmann, C. N. Mitchell, F. Prata, M. Bouillon, J. Carstens, C. Clerbaux, S. M. Osprey, N. Powell, C. E. Randall, and J. Yue (Sept. 2022). "Surface-to-space atmospheric waves from Hunga Tonga-Hunga Ha'apai eruption". In: *Nature* 609.7928, pp. 741–746. DOI: 10.1038/s41586-022-05012-5.

Wu, D. L. and J. W. Waters (1996). "Satellite observations of atmospheric variances: A possible indication of gravity waves". In: *Geophysical Research Letters* 23.24, pp. 3631–3634. DOI: https://doi.org/10.1029/96GL02907.

Wurtele, M. G., R. D. Sharman, and T. D. Keller (1987). "Analysis and Simulations of a Troposphere–Stratosphere Gravity Wave Model. Part I". In: *Journal of Atmospheric Sciences* 44.21, pp. 3269–3281. DOI: 10.1175/1520-0469(1987)044<3269:AASOAT>2.0.CO;2.

Yamazaki, Y., V. Matthias, Y. Miyoshi, C. Stolle, T. Siddiqui, G. Kervalishvili, J. Laštovička, M. Kozubek, W. Ward, D. R. Themens, S. Kristoffersen, and P. Alken (2020). "September 2019 Antarctic Sudden Stratospheric Warming: Quasi-6-Day Wave Burst and Ionospheric Effects". In: *Geophysical Research Letters* 47.1. e2019GL086577 10.1029/2019GL086577, e2019GL086577. DOI: https://doi.org/10.1029/2019GL086577.

Yang, C., T. Li, D. Lai, X. Wang, X. Xue, and X. Dou (2022). "The Delayed Response of the Troposphere-Stratosphere-Mesosphere Coupling to the 2019 Southern SSW". In: *Geophysical Research Letters* 49.23. e2022GL101759 2022GL101759, e2022GL101759. DOI: https://doi.org/10.1029/2022GL101759.

Yue, J., S. D. Miller, W. C. Straka III, Y.-J. Noh, M.-Y. Chou, R. Kahn, and V. Flower (2022). "La Soufriere Volcanic Eruptions Launched Gravity Waves Into Space". In: *Geophysical Research Letters* 49.8. e2022GL097952 2022GL097952, e2022GL097952. DOI: https://doi.org/10.1029/2022GL097952.

Acknowledgement

First of all, thank you, Markus Rapp, for all your support and valuable time throughout the last three and a half years. I am grateful for your trust in my abilities and for providing me with the scientific freedom that I was able to chart my own path. My path may not have always been as straight as ALIMAs beam, but for me, it has been just as illuminating.
Moreover, I want to say a very big thank you to Bernd Kaifler. Even though you were not assigned as my official supervisor, you have been my guide throughout the vastness of photons and waves. Not only have you tirelessly supported me during my PhD by answering my probably repeating questions and reviewing my manuscripts over and over again, but you've also sparked a new interest in me – from a weather enthusiast to a lidar enthusiast!
Andreas, thank you for releasing me to the end of the world and pulling me back to the IPA. What I learned most from you: follow the red thread – I will try my best!
Furthermore, thank you to the whole Middle Atmosphere matrix group at the IPA. I always appreciated our weekly discussions. Thanks to all the colleagues from the MET department, especially to the irreplaceable office fellow Sonja Gisinger.
I would be lying if I said that I had envisioned my time as a PhD student at the IPA exactly as it turned out to be. In the last three years, the world has temporarily veered off its familiar track, but as my thesis shows different orientation of tracks are not necessarily bad. I appreciated my time as PhD student at the IPA and I am very thankful for meeting so many interesting persons.
To all who also believed in me, whether family or friends. Thanks for all of our support.

Thank you for standing by my side, Michael. Thank you for being my rock in times of challenges and for celebrating the joys of life together.

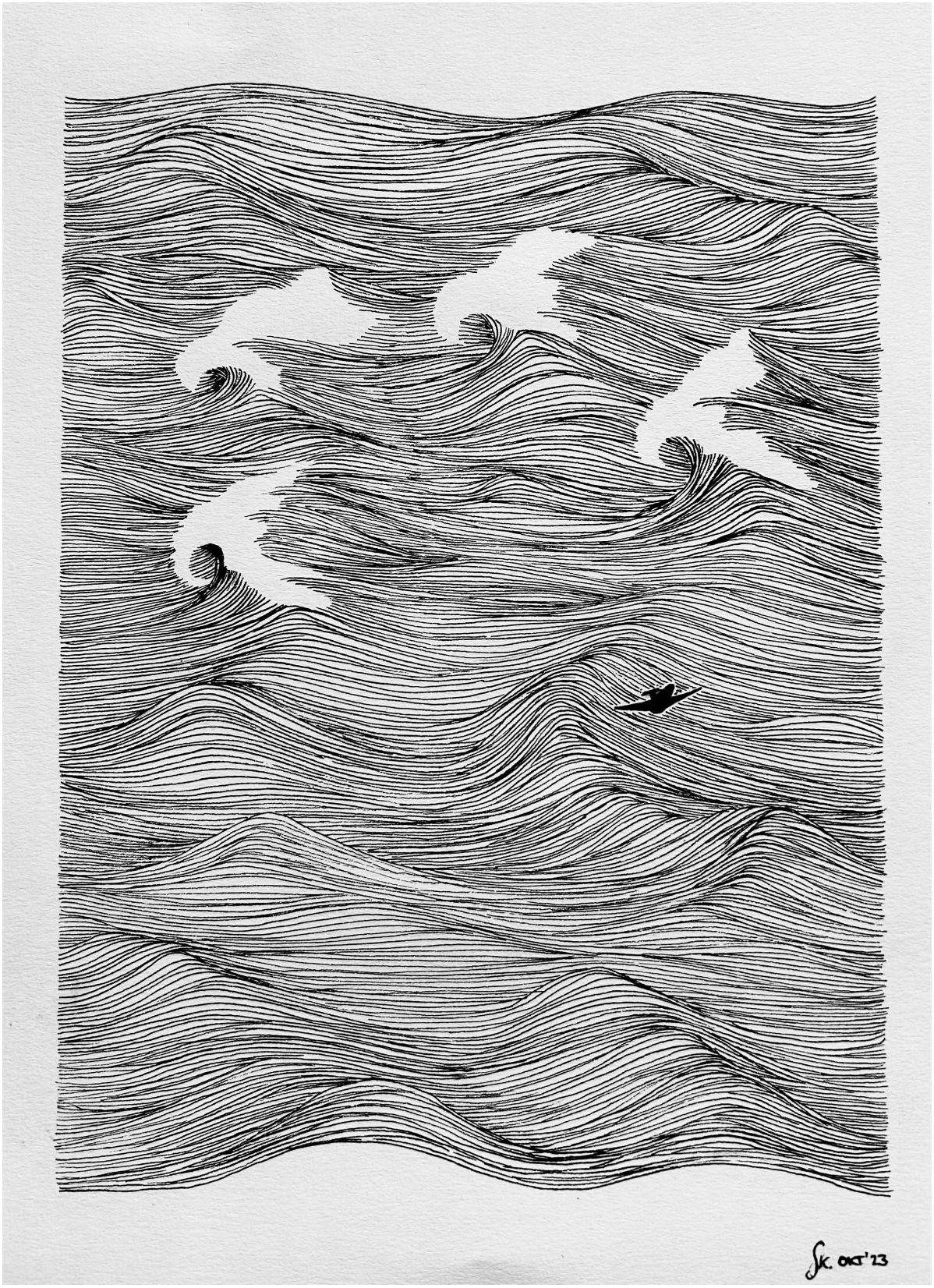
SK. OKT'23